PANJAB UNIVERSITY RESEARCH JOURNAL (SCIENCE)

VOL. 72 2022

PANJAB UNIVERSITY RESEARCH JOURNAL (SCIENCE)
VOLUME 72, 2022

The subscription of the journal may be sent in the form of a Bank Draft payable to ***The Registrar, Panjab University, Chandigarh*** *and addressed to The Editor-in-Chief on the following address:*

Research Journal (Science)
Old Corresponding Building,
Panjab University, Chandigarh -160 014, (India)

The manuscripts for publication or any other enquiry is also to be addressed to the Editor-in-Chief.

Subscription fee:	**Inland**	**Foreign**
Annual Subscription:	Rs. 400/-	US $ 50
Life Membership:	Rs. 3000/-	US $ 250

Printed in 2023

CONTENTS

MODIFIED ECONOMIC MODEL FOR PADDY CROP PRODUCTION FOR SUSTAINABLE WATER MANAGEMENT

Jaswinder Kaur and Onkar Singh
Department of Environmental Studies, Lyallpur Khalsa College Jalandhar 144001

ABSTRACT

Punjab is predominantly an agricultural state with highest percentage of irrigated land. Paddy is widely cultivated in the state and requires large amount of water for irrigation. The underground water fulfills 3/4 requirement of water for paddy crop irrigation. This is the main cause of continuous decline of water table in Punjab. An attempt has been made to use underground water efficiently for the production of paddy crop during the present investigation. Degradable layer of plastic sheet made of high density polyethylene (HDPE) has been introduced at a depth of 18" in soil to prevent percolation of water to the deeper layer of the soil, as paddy roots are adventitious (9" in length). It will also help to prevent percolation of excessive fertilizers and pesticides into deeper layers of soil and underground water. The present method provided better results with 50-60% decline in water consumption and 10-15% increase in yield. This study will help not only to arrest decline in water table but also help to prevent underground water and soil pollution. It is cost effective, as money spent on pumping out water and subsidies given to farmers for electricity by government can be reduced. It provides good health and hygienic conditions to prevent spread of diseases by reducing pollution. The results are in conformity with international investigations. Farmers, Agricultural Universities and Ministry of Agriculture are the main stakeholders who are the beneficiaries.

Keywords: - Irrigation, Water table, Paddy, Pollution.

INTRODUCTION

Punjab had been known as food bowl of India and its economy largely depends upon agriculture. Paddy is widely cultivated in this region and it requires large amount of water. To fulfill the demand, farmers are continuously exploiting underground water. Excessive use of underground water in paddy production is resulting in continuous decline in water table of Punjab. During Paddy cultivation, large amounts of water percolates into the soil with dissolved fertilizers, causing water and soil pollution.

An attempt has been made during the present investigation to develop "Modified Economic Model for Paddy Crop Production for Sustainable Water Management" with following objectives:

(i) To reduce the percolation of water and fertilizers into deeper layers of soil.
(ii) To make efficient use of water for paddy production.
(iii) To save the underground water and soil resources.
(iv) To save electricity, i.e., the cost of pumping out water for irrigation.
(v) To minimize the use of fertilizers and reduce soil pollution.

Out of 50,362 km^2 area of the Punjab state, 39,000 km^2 areas (78%) show a decline in water levels in Punjab. The decadal fluctuation in water level show fall in water levels is between less than 2 meters to more than 4 meters. (Gupta, S. 2011). The dominance of paddy-wheat crop rotation has led to over-exploitation of ground water resulting in rapid decline of water table in the entire state. (Kaur, B. 2011). 110 blocks out of 138 blocks are over-exploited in Punjab based on ground water development. Low water use efficiency is due to high water losses through deep percolation into soil. High amount of energy is required for lifting the underground water to meet irrigation requirements of rice - wheat crops. The study has shown that irrigation consumes the maximum energy among various farm operations for both rice (82%) and wheat (38%). (Singh, K. 2011). Agrochemical processes are responsible for producing chemicals. Irrigated water percolating through soil dissolves carbon dioxide gas produced at high pressures from the plant root respiration and the microbial oxidation of the agricultural matter. The resulting carbonic acid reacts with the insoluble calcium carbonate to produce soluble bicarbonate, which leaches compounds of various metals including uranium from

Corresponding author: environmentlkc@gmail.com
Received: September 10, 2022, Accepted: November 15, 2022

soils and adds it to the shallow ground water. (Alrakabi, et.al 2013) (Singh, et.al 2013) Experimental trials to cultivate rice were quite successful at roof top of Roppongi Hills in Tokyo, Japan as shown in Fig 1. The 130 m^2 area produced over 40 kg of mochi paddy(3070 kg/hectare) (Hui, S. 2011.). About 10.15 billion units of electricity (28% of total consumption of the Punjab State electricity) were consumed by tube-wells in Punjab for pumping out underground water. In 2010-2011, Punjab State Electricity Board has paid about of Rs.309.2 crores for the same. (Singh, K. 2012). Direct Seeded Rice (DSR) emerges as a viable option for timely rice plantation in Punjab during lockdown due to COVID-19 (Bhatt, R and Singh, P 2021). Paddy has adventitious roots. Its roots can grow up to the depth of 16 inches in soil. So, 90% of Nitrogen, Phosphorous and Potassium uptake occurred within 18 inches of soil profile. Hence paddy can be easily cultivated and grown with proposed innovative method with minimum use of water resource as shown in Fig2. (Beyrouty et.al.1997)

During the present study *Oryza sativa* (Basmati rice 1121) was used for paddy cultivation. The experimental trials were conducted in pots, at small scale in $10m^2$ area. Then study was conducted at a site Khadur Sahib in Tarn Taran district of Punjab where Rice is widely grown. It was conducted in June to November in the Kharif season. Soil and water samples were taken before the cultivation of paddy. Experiments were conducted in $1000m^2$ area in farm, which was divided into two half's i.e., $500m^2$ each. in one half the traditional method of growing paddy was used i.e., puddling of soil, in other half the proposed method of paddy was used i.e., by laying down the degradable HDPE (High Density Poly Ethylene) plastic sheet at the depth of 15 inches. Soil and water samples were taken from each field before transplantation. To prepare the field, first remove the top layer of soil of about thickness 15 to 18 inches. Then laying out of the degradable plastic sheet on deeper layer of soil and put again the removed soil on plastic sheet and make a layer of 18 to 24 inches. This prevents the excessive absorption of water and fertilizers by deeper layers of soil when irrigation applies to field. Now field is ready for cultivation of paddy. After the preparation of the field by proposed technique the nursery of rice (basmati 1121) was transplanted in both fields. Approximately 5600-5800 plantlets were planted in each field. The commercial cultivation of Paddy was done by adopting the following steps for the preparation of soil:

Flowchart of Methodology

↓

Remove 18" thick layer of soil (Fig 3a)

↓

Laying out degradable plastic sheet on deeper layer of soil (Fig 3b)

↓

Spread removed soil on plastic sheet (Fig 3c)

↓

Make 18" thick layer of soil on plastic sheet.

↓

Plastic sheet prevents the percolation of water and agrochemicals to the soil

↓

Now field is ready for paddy.

Afterwards the transplantation the paddy crop was closely monitored in both fields and irrigated according to the requirement. The field cultivated in traditional manner requires more water because large amount of water percolates into deeper layer of soil. In the field cultivated by proposed method, there was negligible percolation of water due to underlying sheet and thus it required less amount of water. The rate of evaporation and transpiration is same. It was monitored for about 4 months. After the harvesting of crop, the yield was compared. Soil samples were taken again after the harvesting of crop. Cost analysis was done to design and develop the economic model for the production of paddy crop.

At pot level experiment only water consumption was observed which decreased by about 50% as compared to traditional method. At small scale $10m^2$ level experiment paddy crop required 50% less water as compared to traditional method because negligible percolation of water into the ground. 11% increase in the yield was reported by proposed method as compared to traditional method. It was also observed that the consumption of chemical fertilizers has decreased by 50-55%, because fertilizers did not percolate into deeper layers of soil as shown in figure (4a, 4b, 4c):

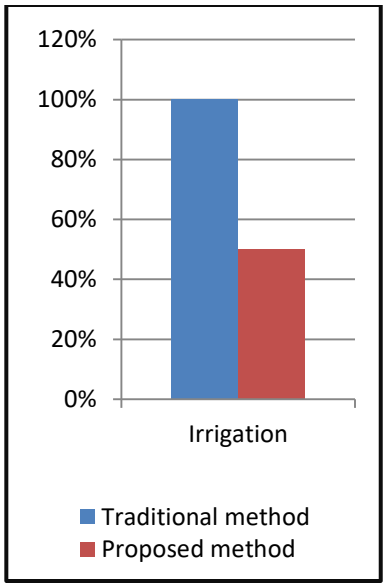

Fig 4a. Water requirement

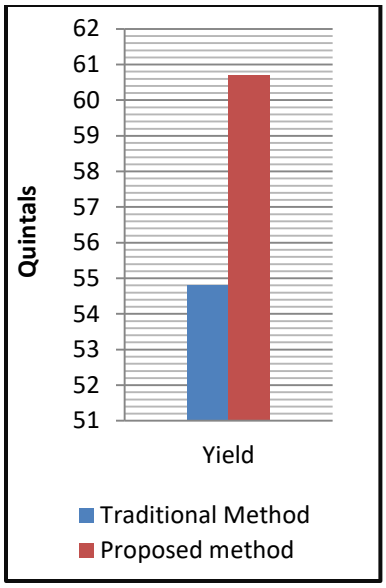

Fig 4b. Crop yield per hectare

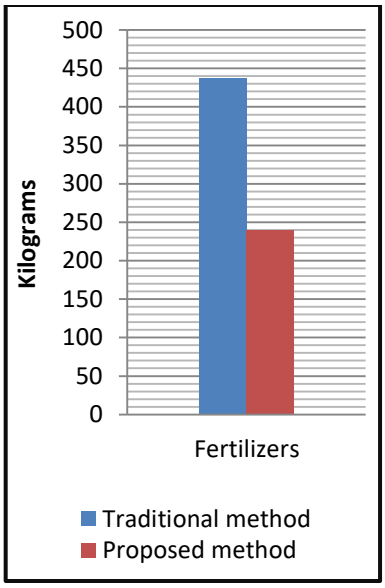

Fig 4c. Fertilizers requirement

At commercial level experiment, paddy crop (Fig 5) required 50% less water as compared to traditional method because negligible percolation of water into the ground. There was about 10% yield increased in proposed method as compared to traditional method. The energy used for pumping water from ground water for irrigation purpose was also reduced to 50%. (Fig.6a,6b,6c).

Particulars	Proposed method	Traditional method
Area	500 sq. meter	500 sq. meter
Date of transplantation	20 June 2016	
Number of plantlet (approx.)	5600-5800	5600-5800
Total rainfall	255.02mm	
Amount. of irrigation	620mm	1250mm
Yield	241.9kg	220.2kg

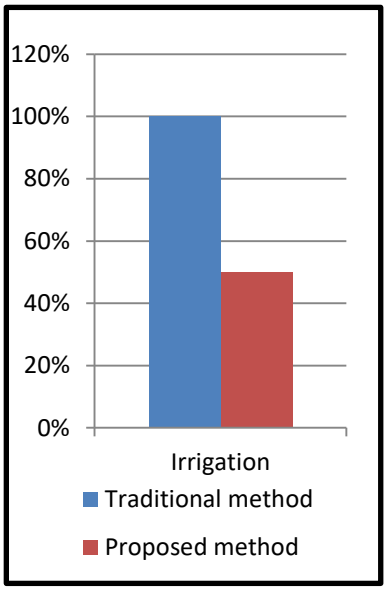

Fig.6a. Water Requirement

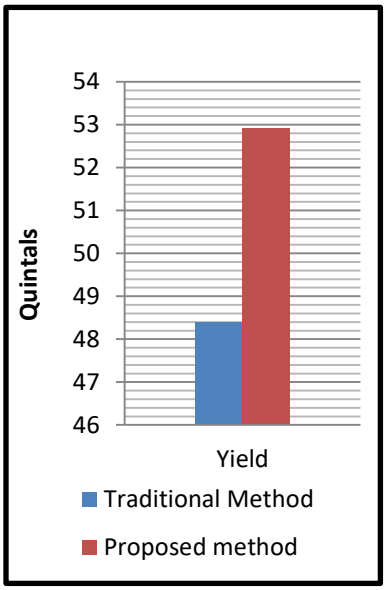

Fig.6b.Crop Yield per Hectare

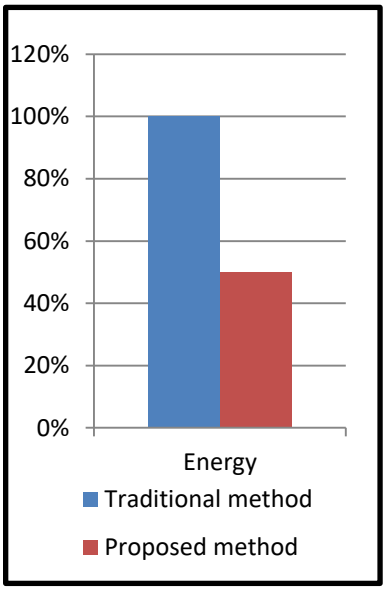

Fig.6c. Electricity/Diesel consumption by tube wells

Results of soil and water samples that were taken before the cultivation of crop are shown below:

WATER ANALYSIS

pH	milli equivalent per litre			Calcium	Residual Sodium Carbonate	Conductance (Micro-mhos/cm)
	Carbonates	Bicarbonate	Chloride			
7.3	Nil	9.2	1.6	7.9	1.3	1090

Source: Samples were tested from Punjab Agricultural University, Ludhiana.

SOIL ANALYSIS

Particulars	pH	Electrical conductivity (mmhos/cm)	Phosphorus (kg/Acre)	Potash (kg/Acre)
Soil sample A (Field with plastic lining)	8.1	0.21	5.0	81
Soil sample B (Normal field)	8.1	0.24	5.0	90

Source: Samples were tested from Punjab Agricultural University, Ludhiana.

Cost analysis assisted to design and develop the economic model for the production of Paddy crop as mentioned below:

Cost of sheet and labor for five years per hectare=Rs. 40,000

COST ANALYSIS

	Traditional Method		Suggested Method (biofertilizers and bio-pesticides)		Suggested Method (Chemical fertilizers and pesticides)	
Particulars	Rice (Rs.)	Wheat (Rs.)	Rice (Rs.)	Wheat (Rs.)	Rice (Rs.)	Wheat (Rs.)
Labor	7,500	2,500	7,500	2,500	7,500	2,500
Diesel	10,000	4,500	5,000	3,000	5,000	3,000
Fertilizers	5,000	5,000	1,000	1,000	1,500	1,500
Pesticides	10,000	2,300	1,000	1,500	6,000	1,500
Spraying (Labor)	2,000	2,000	1,000	1,000	1,500	1,500
Harvesting	10,000	7,700	10,000	7,700	10,000	7,700
Total	44,500	24,000	25,500	16,700	36,500	17,700

Content	**Traditional method**	**Suggested method (biofertilizers and biopesticides)**	**Suggested method (Chemical fertilizers and pesticides)**
Cost (Rs.) of rice and wheat production for one year per hectare	68,500	42,200	54,200
Cost (Rs.) of rice and wheat production for five year per hectare	3,42,500	2,11,000+40,000 =2,51,000	2,71,000+40,000 =3,11,000
Saving per hectare per five year	**0**	**91,500**	**21,500**

Savings made after five years

The conclusions drawn from investigation are:

- ✓ There is about 50% decline in the consumption of water to grow paddy by adopting this innovative method.
- ✓ There is 10% increase in yield in proposed method as compare to traditional method.
- ✓ 50% of electricity or diesel expenditure is saved by farmers, who use electric or diesel pumps to irrigate crop because only 50% water is required for irrigation.
- ✓ Due to underlying degradable plastic sheet, the fertilizers do not percolate into the ground and thus prevents underground water pollution and soil pollution.

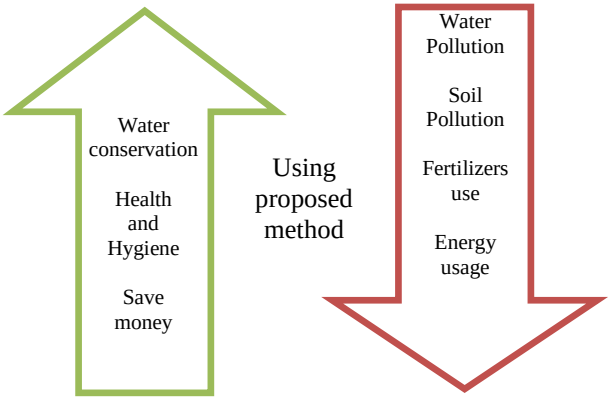

ACKNOWLEDGEMENT

We extend our greatest gratitude to people involved including TERI university (New Delhi) for providing financial assistance and German experts for their valuable guidance.

REFERENCES

Alrakabi, M., G. Singh, A. Bhalla, S. Kumar, A. Srivastava, B. Rai, N. Singh, J. Shahi and D. Mehta, (2013). Study of uranium contamination of ground water in Punjab state in India using X-ray fluorescence technique, Journal of Radioanalytical and Nuclear Chemistry 294 (2): 221-227.

Bhatt, R. and P. Singh, (2021) Adoption status crop Reduction Practices in direct seeded rice: A case study of Kapurthala District of Punjab (India), Indian Journal of Extension Education, 57: 24 -27.

Beyrouty, C.A., R.J. Norman, B.R. Wells, N.A. Slaton, B.C. Grigg, Y.H. Teo and E.E. Gbur, (1997), Distribution and Dynamics of the Rice Root System, (JSSR, Tokyo), 14-15.

Gupta, S. (2011), Ground Water Management in Alluvial Areas Regional Director Central Ground Water Board, New Delhi, 2.

Hui, S. (2011), Green roof urban farming for buildings in high density urban cities. (Invited paper for Hainam China World Green Roof Conference).

Kaur, B. (2011) Indian Journal of Agricultural Economics (Vol.66, No.3), Impact of Climate Change and Cropping Pattern on Ground Water Resources of Punjab, 374.

Singh, G., A. Bhalla, S. Kumar, M. Alrakabi, S. Kumar, A. Srivastava, B. Rai, N. Singh, J. Shahi, and D. Mehta, (2013). Reply to query related to Study of uranium contamination of ground water in Punjab state in India using X-ray fluorescence technique, Journal of Radioanalytical and Nuclear Chemistry 298(1): 731-733.

Singh, K. (2011). Dynamics of Hydraulic Properties of Puddled Soils, Hydraulic Conductivity - Issues, Determination and Applications, Prof. Lakshmanan Elango (Ed.), 29.

Singh, K. (2012) Electricity Subsidy in Punjab Agriculture: Extent and Impact, Indian Journal of Agricultural Economics, 67(4): 619.

Abbreviations

HDPE – High Density Polyethylene

PHYSICO-CHEMICAL ANALYSIS OF GROUND WATER, SOIL AND ITS EFFECTS ON THE GROWTH OF *PHASEOLUS AUREUS*

Jaswinder Kaur* and Maninder Kaur

*Department of Environmental Studies, Lyallpur Khalsa College, Jalandhar

Department of Botanical Sciences, Periyar University, Tamil Nadu

ABSTRACT

Excessive use of fertilizers in the era of industrial revolution has resulted in accumulation of different salts in agriculture soil and groundwater. Salinity is a major constraint to the crop production in District Bathinda of Punjab (India) where plants are subjected to high sodic conditions of soil and water. The present investigation was conducted to analyze the physico-chemical characteristics of groundwater, soil and its effects on the growth of *Phaseolus aureus*. Certified seeds of *Phaseolus aureus* were sown in three sets, treated with different concentration of KCl and NaCl (Control, 0.01M, 0.02M, 0.03M and 0.04M) to study the morphological and biochemical parameters. The soil analysis showed that it was medium in nitrogen and phosphorus content but had higher values of potassium content than critical limits. The ground water was found to be slightly alkaline in nature. Higher concentration of salts like KCl and NaCl showed impaired seed germination, less nodule formation, less plant development and decline in crop yield with low protein content. Therefore, introduction of salt tolerant varieties of *Phaseolus spp*. and introduction of appropriate methods of irrigation like furrow irrigation and sprinkling can be chosen to supplement the problem of soil salinity for agriculture by the farmers.

Keywords: *Phaseolus aureus*, Physico-Chemical analysis, Ground water, Protein content

INTRODUCTION

Excessive use of fertilizers in the era of industrial revolution is to bring sufficiency in the production of food grains. It also results in the accumulation of different salts in agricultural soil as well as ground water. Excessive amount of salt in the soil adversely affects plant growth and development. Nearly 20% of the world's cultivated area and nearly half of the world's irrigated lands are affected by salinity (Zhu, J.K., 2001). Due to excessive availability of canal water for agriculture and use of phosphate fertilizers in the waterlogged areas, there is increase in the problem of salinity in Bathinda District of Punjab. (Singh et.al, 2013). Agro-chemical processes are also potential source of uranium contamination of groundwater (Alrakabi et.al., 2013). Overuse of agro-chemicals in agricultural land and release of inefficiently treated industrial effluents is responsible for deteriorating the groundwater quality of Mansa District in Punjab (Sharma et.al., 2021). The potentially toxic elements pose significant health risk via groundwater consumption. There was dominance of Arsenic and Mercury in groundwater contamination over uranium leading to more risk of cancer in Bathinda District in Punjab (Sharma et.al., 2021).

Salinity is major constraint to the crop production in District Bathinda of Punjab (India) where plants are subjected to high sodic conditions of soil and water. The processes such as seed germination, seedling growth and vigour, vegetable growth, flowering and fruits set are adversely affected by high salt concentration which reduce quality of produce and economic yield. The salts get accumulated in soil due to high evaporative demand and insufficient leaching of ions because of low precipitation. Leguminosae is a salt sensitive family in which limited variability for salinity tolerance has been detected. Legumes have capacity to develop symbiotic association which leads to sustainable agricultural practices and reduce in use of agrochemicals. Keeping the above scenario in mind, Mung Bean, *Phaseolus aureus* Linn. Var. 668; Family Leguminosae was selected as the study crop during the present investigation with following objectives:

(i) to study the physico-chemical analysis of ground water and soil of Bathinda, Punjab (India).

Corresponding author: environmentlkc@gmail.com
Received: September 10, 2022, Accepted: December 5, 2022

(ii) to study the effect of different concentrations of NaCl and KCl on germination and protein content of *Phaseolus aureus*.

MATERIAL AND METHODS

Ground water samples used for analysis were collected from pumps installed in DAV College Bathinda. The ground water was analyzed for its physico-chemical characteristics following AWWA (American Waste Water Analysis), APHA (American Public Health Association), WEF (Water Environment Federation) 1995 and organic nitrogen content by using semi-micro Kjeldhal method (1983). The estimation of potassium content was determined by Flame photometric method given by Yadav and Khera (1993). The soil collected from the depth of six inches from agriculture farm of DAV College, Bathinda was used for analysis. The physico-chemical characteristics of soil were determined by following methodology given by AWWA, APHA, WEF(1995). The nitrogen content in the soil sample was determined by using semi-micro Kjeldhal method (1983), phosphorus and potassium content by following methods suggested by Olsen et.al. (1954) and Merwin and Peech (1950), respectively. The critical limits of these contents for soil analysis were compared according to standards given by Department of Soil Sciences, Punjab Agricultural University Ludhiana (Punjab) (Table 1).

Table 1: Critical limits of Standard Values for Soil Analysis

	Low	Medium	High
Available Nitrogen (Kg/ha)	<272	272-422	>422
Available Phosphorus (Kg/ha)	<12.4	12.4-22.4	>22.4
Available Potassium (Kg/ha)	<114	114-277	>277

Source: Department of Soil Sciences, Punjab Agriculture University, Ludhiana

Certified seeds of *Phaseolus aureus* Linn. Var. 668 procured from PAU Ludhiana were sown in petriplates on wet Whatman filter paper no. 1 in sterile conditions. The seedlings were treated with different concentrations of KCl and NaCl (Control, 0.01M, 0.02M, 0.03M and 0.04M) to study the morphological and biochemical parameters like germination percentage, shoot & root length, and protein content. The protein content was estimated by following the protocol of Lowry(1951). Morphological and biochemical parameters were statistically analyzed by calculating the mean value and standard deviation (SD).

RESULTS

The physico-chemical analysis of ground water was slightly alkaline in nature (Table 2). It showed the dominance of nitrogen content. Potassium content was lower than sodium content. The concentration of carbonate content was very low as compared bicarbonate content. The results were in conformity with physico-chemical analysis performed by Brar et. al. (2002) on water samples taken from south western region of Punjab (India). Analysis of soil revealed that it was medium for nitrogen and phosphate content and has higher potassium content (Table 3) than critical limits according to standards given by Punjab Agriculture University Ludhiana (Punjab). Higher concentrations of sodium ions affected the soil texture and its properties.

Table 2: Physico- Chemical Parameters of Groundwater

Parameter	Observation/concentration
Color	Slight brown tinge
Odor	Odorless
pH	8.2
Temperature	20°C
Electrical conductivity	13 m mhos
Chlorides	52.5 mg/ l
Sodium	44.4 mg/ l
Potassium	21.1 mg/ l
Nitrogen	61 mg/ l
Carbonates	0.8 mg/ l
Bicarbonates	18.0 mg/ l
Total solids	230 mg/ l
Total dissolved solids	191 mg/ l

Table 3: Physico- Chemical Parameters of Soil

Parameter	Values
Color	Light brown
pH	8.4
Temperature	20°C
Electrical conductivity	21 m mhos
Available phosphorus	18.5 Kg/ha
Available potassium	352.8 Kg/ha
Available nitrogen	325.3 Kg/ha

The presence of salts in excess rendered the availability of other nutrients like nitrogen and potassium. So, the major factor behind the less plant growth in saline soil is non-availability of nitrogen and potassium. Percentage germination decreased with increase in concentration of KCl and NaCl solutions. It was found maximum in control (83%) and minimum in 0.04M in NaCl (20%). Shoot length was recorded in 3, 6 and 9 days old seedlings. It was maximum in control (4.5, 5.7 and 6.6 cm respectively) and decreased with increasing concentrations of NaCl and KCl. It was found minimum in 0.04M NaCl solution (1.4, 2.4 and 3.1 cm respectively) as shown in Table 4. Average Root length also decreased with increasing concentrations of NaCl and KCl solution. In 3, 6 and 9 days old seedlings, it was maximum in control (4.9, 6.5 and 6.9 cm respectively) and was minimum in 0.04M in NaCl solution (3.4, 4.8 and 5.3 cm respectively) as shown in Table 4. Reduction in root length in KCl was less as compared to NaCl. The root protein content showed maximum value 0.280 mg/g fw and minimum value 0.11 mg/g fw. The shoot protein content also decreased with increasing concentration of NaCl and KCl solution (Table 5). Similar results were also observed by Brar et al (2002). Physico-chemical analysis of sewage water, soil and its effects on the growth of potato were also determined by Kaur and Kaur 2005. A field study was also carried out by Sidhu et. at. 2012 for physico-chemical analysis of soil and micronutrient concentration of different vegetables at regional station Bathinda. The results are comparable with the present investigation.

Table 4: Effect of Different Concentration of NaCl and KCl on Morphology of *Phaseolus aureus*

Concentration	Root and Shoot length (cm)					
	3 days old		6 days old		9 days old	
	Root	Shoot	Root	Shoot	Root	Shoot
Control	4.9±1.1	4.5±1.0	6.5±1.6	5.7±0.3	6.9±0.6	6.6±0.3
0.01M NaCl	4.5±0.2	3.8±0.3	6.4±0.7	5.5±0.1	6.8±0.1	6.4±0.1
0.02M NaCl	4.4±0.5	3.7±0.1	5.8±1.0	5.1±0.4	6.6±0.1	6.1±0.8
0.03M NaCl	4.0±0.1	3.0±0.8	5.0±0.2	4.4±0.5	6.6±0.1	5.4±0.9
0.04M NaCl	3.4±0.5	1.4±0.4	4.8±0.2	2.4±0.8	5.3±0.3	3.1±1.2
	Root	**Shoot**	**Root**	**Shoot**	**Root**	**Shoot**
Control	4.9±1.1	4.5±1.0	6.5±1.6	5.7±0.3	6.9±0.6	6.6±0.3
0.01M KCl	4.8±0.2	4.3±0.1	6.4±0.7	5.4±0.3	6.8±0.2	6.5±1.6
0.02M KCl	4.8±0.0	3.4±0.5	5.8±1.0	5.1±0.4	6.7±0.1	6.4±0.7
0.03M KCl	4.5±0.2	3.0±0.8	5.7±0.2	4.8±0.2	6.6±0.1	5.4±0.3
0.04M KCl	4.4±0.5	2.7±0.2	5.4±0.3	4.0±0.1	6.4±0.7	4.5±0.2

*Data Shown are Mean ±SE of three replicates.

Table 5: Effect of different concentrations of NaCl and KCl on protein content of 9 day old seedlings of *Phaseolus aureus*

Concentration	Protein content (mg/ g fw)	
	Root	**Shoot**
Control	0.280	0.131
0.01M NaCl	0.240	0.105
0.02M NaCl	0.200	0.102
0.03M NaCl	0.170	0.096
0.04M NaCl	0.110	0.083
	Root	**Shoot**
Control	0.280	0.131
0.01M KCl	0.276	0.122
0.02M KCl	0.243	0.118
0.03M KCl	0.203	0.101
0.04M KCl	0.167	0.099

In the end, it can be concluded that higher concentration of salts like KCl and NaCl show impaired seed germination, less nodule formation, less plant development and decline in crop yield with low protein content. To fight against salt stress, introduction of salt tolerant varieties like Phaseolus spp. from Leguminosae family can be suggested for cultivation in Bathinda District. Another suggestion is the selection of appropriate methods of irrigation like furrow irrigation and sprinkling can be chosen to supplement the problem of soil salinity for agriculture by the farmers. With furrow irrigation method, there is tendency for the salts to accumulate in the ridges, because the leaching occurs only in the furrows. Wide-bottomed furrows that resemble narrow border strips have certain advantages for wetting the soil surface uniformly thereby, controlling salt accumulation in large fraction of the root zone. As the present studied crop is drought tolerant but susceptible to waterlogging so sprinkling method can also help in its cultivation as well as to check soil salinity.

ACKNOWLEDGEMENT

We extend our greatest gratitude to Department of Soil Sciences, Panjab Agriculture University, Ludhiana, Punjab for their valuable guidance.

REFERENCES

Alrakabi, M., G. Singh, A. Bhalla, S. Kumar, A. Srivastava, B. Rai, N. Singh, J. Shahi and D. Mehta, (2013). Study of uranium contamination of ground water in Punjab state

in India using X-ray fluorescence technique, Journal of Radioanalytical and Nuclear Chemistry 294 (2): 221-227.

Apha, Awwa, Wef 1995. Standard Methods for the examination of water and waste water (eds. A.D. Eaton, L.S. Clesceri and A.E. Greenberg, Eds.). American Public Health Association, Washington, D.C.

Brar, J.S. et al. 2002. An appraisal of underground irrigation water quality of south–western region of Punjab, International Journal of Tropical Agriculture, 20.

Kaur, J. and S. Kaur, 2005. Physico-chemical analysis of sewage water and its effects on parameters of soil and *Solanum tuberosum* Linn. Panjab University Research Journal Sci, 55: 63-73.

Kjeldahl, J. 1983. A new method for the determination of nitrogen in organic matter, J. Anal. Chem. 22: 366.

Lowry, O.H., N.J. Rosebrough, A.L. Farr, and R.J. Randall, 1951. Protein measurement with folin-phenol reagent. J. Biol. Chem. 193: 265-275.

Merwin, H.D., M. Peech, 1950. Exchangeability of soil potassium in sand, silt and clay fractions as influenced by the nature of complimentary exchangeable cations, Soil Sci. Am. Proc 15: 125-128.

Olsen, S.R., C.V. Cole, F.S. Watanabe, and L.A. Dean, 1954. Estimation of available phosphorus by extraction with sodium bicarbonate. U.S. Dept. Agric. Circ. 938.

Sidhu, A.S., J.S. Manchanda, R.P.S. Dalal, and N. Garg, 2011, Micronutrient status of soils and different vegetable crops grown in sewage water irrigated fields. Indian Journals.com, 11:420-424.

Singh, G., A. Bhalla, S. Kumar, M. Alrakabi, S. Kumar, A. Srivastava, B. Rai, N. Singh, J. Shahi and D. Mehta, (2013). Reply to query related to Study of uranium contamination of ground water in Punjab state in India using X-ray fluorescence technique, Journal of Radioanalytical and Nuclear Chemistry 298(1): 731-733

Sharma, T., B.S. Bajwa, and I. Kaur, 2021, Contamination of ground water by potentially toxic elements in ground water and potential risk to groundwater user in Bathinda and Faridkot districts of Punjab. Environment Earth Sciences 80: 250.

Sharma, T., P.K. Litoria, B.S. Bajwa, and I. Kaur, 2021. Appraisal of ground water quality and associated risks in Mansa District of Punjab (India). Environmental Monitoring and Assessment Sciences 193: 159.

Yadav, B.R. and M.S. Khera, 1993. Analysis of irrigation waters. In: Methods of analysis of soil, plants, water and fertilizers (H.L.S. Tandon, Ed.). Fertilizers Development and Consultation Organization, New Delhi 83-116.

Zhu, J.K. (2001) Plant Salt Tolerance. Trends in Plant Science, 6, 66-71.

ABBREVIATIONS

APHA – American Public Health Education
AWWA – American Waste Water Analysis
WEF – Water Environment Federation

ON A COMPARATIVE ANALYSIS OF VARIOUS MACHINE LEARNING MODELS TO PREDICT THE INVARIANT MASS OF DIELECTRONS IN 2-110 GEV RANGE

Ojas Bhardwaj and Shivaansh Raturi
Department of Physics, Panjab University, Chandigarh-160014

ABSTRACT

The invariant mass of a scattering system is a well known quantity and is useful in the calculations of dynamic parameters of a scattering event. This paper sets out to introduce, build, compare and demonstrate the utility of various regression models based on machine learning techniques, using data [1] of 100, 000 electron-electron production events in the $2 - 110$ *GeV* range, detected by the Compact Muon Solenoid (CMS) at CERN, to predict the invariant mass of the dielectron system for a given set of test energies and momenta. Of the models evaluated, the LGBM regressor was found to have the highest accuracy of 92.34%. This method can be useful to differentiate abnormal collision results from expected results.

Keywords: Electron-electron seattering machine learning, regression models

INTRODUCTION

Dielectron systems are formed in high-energy collider experiments like the LHC as decay products of heavier collision products [2]. Above the electroweak energy scale of ~90 *GeV*, the decay of Z^0 boson is one of the primary modes of production of dielectrons. Thus a collection of dielectron events with the center of mass energy around the electroweak scale should allow for the reconstruction of the Z^0 peak signature. We shall be using natural units ($c = \hbar = 1$) in the following sections.

Brief overview of the invariant mass of composite systems

The invariant mass is invariant under Lorentz transformations characterized by the system's total energy and momentum, i.e. it is the same in all frames of reference related by Lorentz transformations. In the case of a two-body system, where an object is moving towards another object which is initially at rest, the magnitude of the invariant mass of this two-body system is different from the sum of rest mass (i.e. their respective mass when stationary). For a more general *n* particle system, because the invariant mass is a Lorentz invariant quantity, the following form holds true in all frames of reference:

$$\mathrm{M}_{inv}^2 = \left(\sum_{i=1}^{n} E_i\right)^2 - \left(\sum_{i=1}^{n} p_i\right)^2 \quad (1)$$

Using Einstein's relation: $E_i^2 = m_i^2 + p_i^2$, where m_i is the rest mass of the $i-th$ particle and p_i is the momentum, for the special case of 2 particles, eq (1) can be simplified to:

$$M_{inv}^2 = m_1^2 + m_2^2 + 2(E_1E_2 - \overrightarrow{p_1}.\overrightarrow{p_2}) \quad (2)$$

Equation (2) can be rewritten in a more standard form by introducing the parameter pseudorapidity [3] η :

$$\eta \equiv -\ln\left[\tan\left(\frac{\theta}{2}\right)\right] \quad (3)$$

Where θ is the angle between the 3-momentum of the particle and the beam axis. Pseudorapidity can be thought of as one of the coordinates specifying the position of the colliding particles in the center of momentum frame, the other coordinate being the azimuthal angle ϕ.

These are measurables already known in a collider experiment. If p_T is the transverse momentum of the particle after the collision, and the particles move at relativistic speeds ($E >> m$) equation (2) can be reduced to [3]:

Corresponding author: shivaanshraturi07@gmail.com
Received: August 09, 2022, Accepted: October 28, 2022

$$M_{inv}^2 = 2p_{T1}p_{T2}\left(cosh(\eta_1 - \eta_2) - cos(\emptyset_1 - \emptyset_2)\right) \quad (4)$$

If we do not have knowledge of equation (4), we cannot use it to calculate the invariant mass which we may call our target variable henceforth. However, by knowing E_1, E_2, p_1, p_2, p_T , η_1, η_2, ϕ_1 and ϕ_2, which we shall refer to as the predictor variables and training a machine learning model we can predict the distribution of invariant mass of the dielectron system with reasonable accuracy.

DATASET DESCRIPTION AND METHODOLOGY

The dataset [1] used for analysis is a publically available open dataset released by the CMS (Compact Muon Solenoid) collaboration at CERN and was acquired through CERN's opendata portal.

The dataset consists of 100,000 dielectron events in the invariant mass range $2 - 110$ *GeV*. The data consists of 19 attributes: Run number *Run*, Event number *Event*, energies of the two electrons E_1, E_2, components of the incoming 3-momenta of the two p_{1x}, p_{1y}, p_{1z},p_{2x}, p_{2y}, p_{2z}, transverse momentum of the products p_{T1}, p_{T2}, pseudorapidities η_1, η_2, azimuthal angles ϕ_1, ϕ_2, charges Q_1, Q_2 and invariant mass M. This data is an example of a labeled dataset where the all the observed variables have been labeled previously.

Data processing

System specifications of the machine used are as follows: **Operating system** Microsoft Windows 10, *build 19045* (64 bit), **Processor** Intel*(R)* Core*(TM) i5-8250U* CPU @ 1.60 GHz, **RAM** 8.00 GB.

The data file was processed in *Python v3.9* using *Jupyter Notebook* computational environment, where it was subjected to cleaning algorithms (discussed below) to ensure that the integrity of the data was not compromised.

Python packages used were: *Numpy* and *Scipy* for standard mathematical and statistical functions, *Pandas* for interacting with the dataframe environments, *Mat-plotlib* and *Seaborn* for plotting and data visualization, and *ScikitLearn* for implementing machine learning algorithms.

The cleaning process comprised of checking for missing values and removing duplicate values and outliers which may affect the accuracy of the model. Duplicates in the data can be removed by using the *pandas* library function *pandas.drop-duplicates()*. The raw data was then searched for missing or *NaN* values using another *pandas* library function *pandas.isnull()* and it was found that 85 values of the invariant mass were null values and thus the observation data corresponding to these values were dropped from the working dataframe using the function *pandas.dropna()*.

Restricting the dataset

The observational dataset ranges from 2 to 110 *GeV*. The vast number of decay modes at low energies leads to uncertainty about the source of dielectron peaks. Moreover, to isolate the electroweak sector from redundant events, it is necessary to place a restriction on the energy range under analysis. To reject low energy background sources most efficiently, a prefilter algorithm was implemented. It was found that the cut value $m < 60$ *GeV* is optimal for the analysis of the dielectrons produced through Z^0 decay. This selection criterion leads to better signal to background ratio.

Outlier detection

An outlier is an extremely high or extremely low data point relative to the nearest data point and the rest of the neighboring co-existing values in a dataset. To smoothen out and clean the data one has to either remove the outlying data point or replace it with an appropriate value. To identify the outliers, Z-scoring algorithm was used. One can also use other methods to identify outliers like the sorting method, in which one sorts the data to identify extreme (minimum and maximum) values which can then be replaced or removed, or plotting a box-and-whisker plot of the data. A Z-score is a numerical measurement that describes a value's relationship to the mean of a group of values. Z-score is measured in terms of standard deviations from the mean and is given by:

$$Z = \frac{(x_i - \pi)}{\sigma} \quad (5)$$

where x_i is the data point, μ is the mean of the dataset and σ is the (sample) standard deviation of the data of N sample points given by:

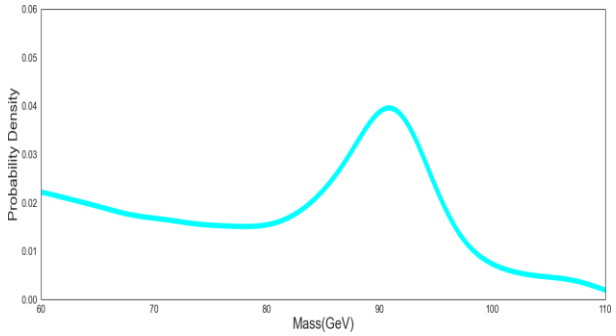

Figure 1: Kernel Density Estimate (KDE) for invariant mass. Notice the absence of the initial peak around 2 *GeV*.

$$\sigma = \sqrt{\frac{1}{N-1}\sum_i (x_i - \mu)^2}$$

Since N is very large $N - 1 \approx N$ thus the total standard deviation simplifies to:

$$\sigma = \sqrt{\langle x^2 \rangle - \langle x^2 \rangle}$$

where $\langle x \rangle \equiv \frac{1}{N}\sum_i x_i$ the sample mean. One can think of the Z score as a distance of a point from the mean measured in terms of standard deviation. If we assume that our data follows a normal distribution, a distance of 1σ from the mean will contain around 68% of the data, 2σ contains around 95% of the data and 3σ contains around 99.7% of the total data points. We have taken 3σ or $|Z| = 3$ as an acceptable Z- threshold as it contains enough data to not affect overall trends present in the data while removing outliers that may not be removed in a 3σ cleaning. Thus any point that lies at a distance greater than 3σ such that $|Z| > 3$ is considered an outlier else it is considered a normal point. An outlier data point is dropped upon identification.

Exploratory data analysis

The cleaned data is used as our final working dataset. To identify and understand any relationships that exist between the predictor variables (like momentum and energy) and the target variable (invariant mass), various kinds of data visualization tools were utilized.

A normalised histogram of the invariant masses for different energies was plotted, using the *Matplotlib* library function *hist()*, to give a probability distribution function or PDF. Fig. 2 shows the PDF for the invariant mass. We can infer the following from the PDF:

- The PDF is mainly described by a broad scattering background and a peak around *91 GeV*.
- The high energy peak corresponds to the production energy of Z^0-boson, one of the intermediate vector bosons of the weak force. The energy scales are above the threshold of electroweak unification, so a decay mode for electron-positron annihilation through the Z^0 is possible.
- The PDF is normalized, i.e. if $\rho(m)$ is the probability of observing mass in a range m to $m + dm$, then over the entire mass range, by unitarity:

$$\int_0^\infty \rho(m)dm = 1$$

- The expectation value of the dielectron invariant mass can be calculated by using:

$$\langle M_{inv} \rangle = \int_0^\infty mp(m)dm$$

where $\rho(m)$ is the normalised PDF and m is the invariant mass, and it came out to be *81.09 GeV*.

An equivalent representation to the histogram is a Kernel Density Estimate (KDE) shown in Fig. 3 created using the *Seaborn* library function *kdeplot()*. Notice the low energy peak disappears in the KDE plot. Any accurate prediction model must be able to reproduce this plot. KDE plots were also made for the predictor variables like momenta, energies and pseudorapidities (Fig.3).

- The KDEs of the predictor variables show that the majority of scattering events took place at low energies and at low momenta (as can be seen from Fig.3(a),3(b),3(c) and 3(e)).
- By conservation of momentum, the total directional sum of the transverse momenta must be zero. Any deviations between the two transverse momenta which leads to"missing" momenta must be because of particles like neutrinos which are not seen by the detector.
- From Fig.3(f) we see the primary scattering angles (as expressed through pseudorapidity). There is a symmetry in the graph because the beam can scatter at any angle ϕ between the two maxima and thus, it appears as a ring.

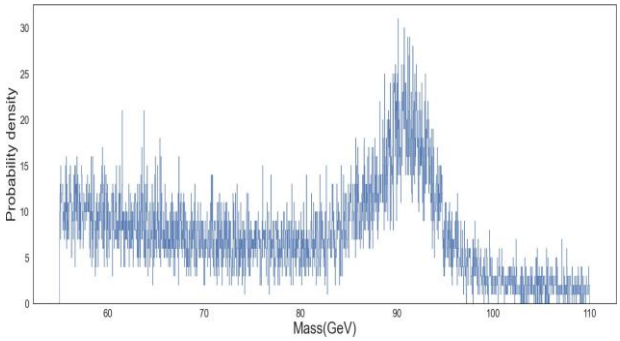

Figure 2: Probability Density Function (PDF) for invariant mass. Notice the peak around *91 GeV* indicates the presence of Z^0 boson.

To see the relationships between the predictor variables and the target variable, scatterplots were created (Fig. 5). A correlation heatmap was also constructed to quantify the correlations and determine the parameters which affected the mass most significantly using *seaborn.heatmap()* and *pandas.corr()*. Fig. 4 shows the correlation heatmap for the working dataset. The major observations are:

- The parameters which had a significant impact on the mass were E_1, E_2, p_{T1} and p_{T2} as expected. Thus for a linear regression training model these are the most consequential criterion.

- The energies E_1 and E_2 had a strong correlation with the transverse momenta p_{T1} and p_{T2}, which is expected. No other parameters had a significant cross- correlation with either the invariant mass or any other parameters.

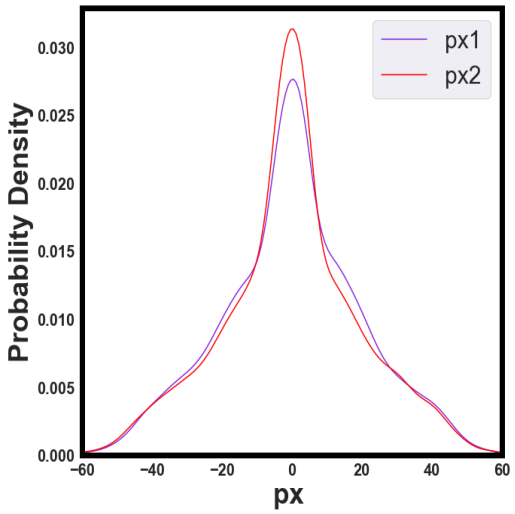

(a) px1 and px2 kernel density estimate

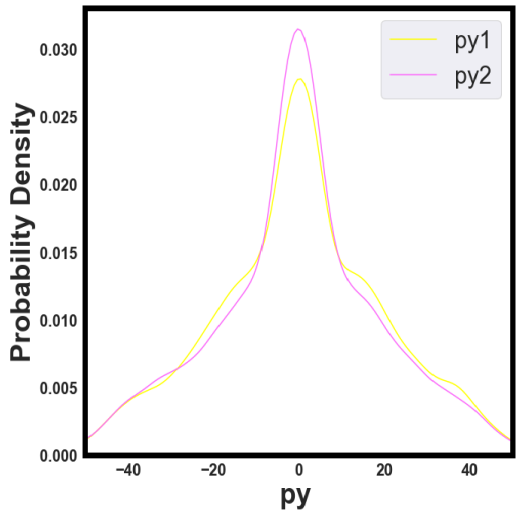

(b) py1 and py2 kernel density estimate

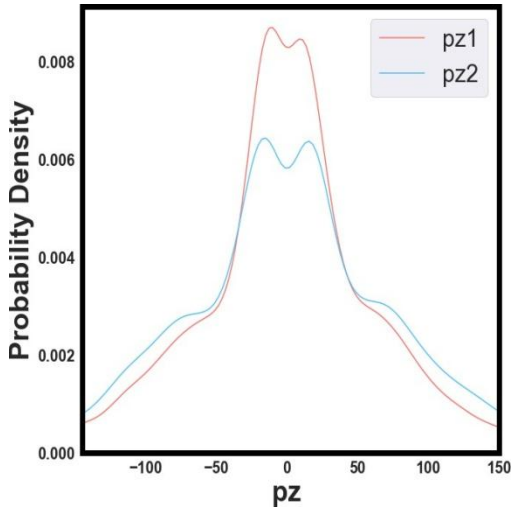

(c) pz1 and pz2 kernel density estimate

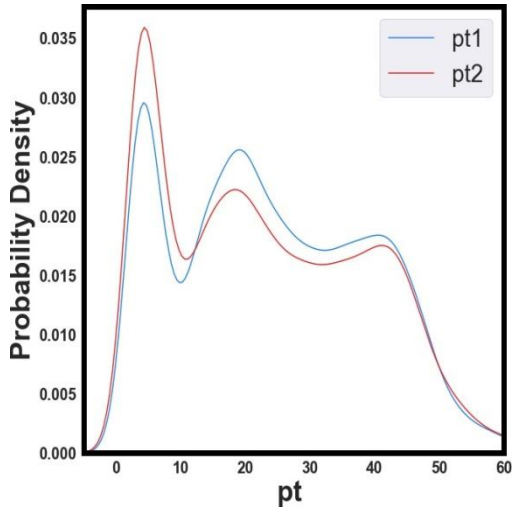

(d) pt1 and pt2 kernel density estimate

Splitting training and testing data

To create a machine learning model, one needs to train an algorithm using the observed data. To see if the predictions of the model are correct, one needs to compare them with another distinct set of observations. Thus the data used to train the model is naturally called training data while the data used to check the accuracy of the model is called testing data. Ideally, a model should be trained on all of the dataset but if no other distinct set of observations is available for testing, both the training and testing data can be taken from the same source dataset.

Training and testing data were split from the original dataset by randomly per- muting the indices of the data frame and the ratio of training data to testing data was chosen to be 80 : 20, although 70 : 30 is also a good choice. An alternate way to quickly split the dataset is to use *train test split()* function in the *sklearn* library.

The problem of predicting the target variable for different values of a predic- tor variable requires a regression-type machine learning model. Various regression algorithms which are used to construct these models are discussed as follows:

Brief description of the modeling algorithms used

We now explore some of the most common regression algorithms which can be used to train machine learning models to predict results for any given set of predictor variables.

Linear regressor

Linear Regression fits a linear model with coefficients $w = (w_1, w_2, \ldots, w_p)$ to min- imize the residual sum of squares between the observed targets in the dataset, and the targets predicted by the linear approximation [4]:

$$\mathcal{Y} = w_0 + w_1 x_1 + w_2 x_2 + \cdots + w_k x_k \quad (6)$$

If $y_1, y_2, \ldots y_n$ are observed values of a target variable, residuals or the loss function between the observed and fitted values are given by:

$$\mathrm{R} = \sum_{i=1}^{n} (y_i - \sum_{j=1}^{k} w_j x_{ij})^2 \quad (7)$$

By choosing w_j, R can be minimized, giving the equation of the fitted target variable. Here y is the target variable while $x_1, x_2, \ldots$ are the predictor variables. Essentially, the machine is trained to extrapolate by fitting a linear curve through the training data. It is the simplest kind of regression algorithm thus it can be taken as a good benchmark to compare the models with. The algorithm fails to accurately describe more complicated relationships between the target and predictors.

Linear regression training algorithm was implemented using *sklearn* library's inbuilt function *linear_model. LinearRegression()*

Lasso regressor

Lasso (Least Absolute Shrinkage and Selection Operator) or L1 is a type of linear regressor that uses shrinkage, that is where data values are shrunk towards a central point [5]. Least squares regression isn't defined at all when the number of predictors exceeds the number of observations. This leads to overfitting a model and failure to find unique solutions. Least squares also has issues dealing with multicollinearity in data. The major difference between a normal linear regressor and lasso regressor is the bias or tuning parameter λ (calculated using cross validation). The bias introduces a slightly worse fitting line but the overall variance of the data is lower than the linear fit. For a lasso regressor, equation (11) is modified to:

$$\mathrm{R} = \sum_{i=1}^{n} (y_i - \sum_{j=1}^{k} w_j x_{ij})^2 + \lambda \sum_{j=1}^{k} |w_j| \quad (8)$$

To implement the Lasso regression training algorithm *sklearn* library's inbuilt function *linear_model. Lasso()* was used.

Ridge Linear regressor

Ridge or L2 is a type of linear regressor, which similar to the Lasso regressor, uses shrinkage [5]. The difference between Ridge and Lasso regressor is only in the regularization function:

$$\mathrm{R} = \sum_{i=1}^{n} (y_i - \sum_{j=1}^{k} w_j x_{ij})^2 + \lambda \sum_{j=1}^{k} w_j^2 \quad (9)$$

A ridge regressor is prefferable for dealing with problems related to colinearity while a lasso regressor is preferable

for dealing with overfitting. Ridge regression training algorithm can be implemented using *sklearn* library's inbuilt function *linear_model.Ridge()* was used.

Decision Tree regressor

The goal of a decision tree is to create a model that predicts the value of a target variable by learning simple decision rules inferred from the data features [5]. It breaks down a dataset into smaller subsets while at the same time an associated decision tree is incrementally developed. The final result is a tree with decision nodes and leaf nodes. The main advantage of decision tree is that non-linearity does not affect the model's performance and the number of hyper-parameters to be tuned is almost null. Also decision trees are not largely influenced by outliers or missing values however overfitting is one of the practical difficulties for decision tree models. Overfitting can be overcome using a *Random Forest* algorithm. Decision tree regressor was implemented using the *sklearn* function *tree. DecisionTreeRegressor()*.

Gradient Boost regressor

Gradient boosting is a machine learning technique used in regression and classification tasks, among others [6]. It is an iterative algorithm which builds a fairly accurate model using an ensemble of relatively inaccurate models (like simpler linear regressors or decision tree regressors.) This estimator builds an additive model in a forward stage-wise fashion; it allows for the optimization of arbitrary differentiable loss functions. In each stage a regression tree is fit on the negative gradient of the given loss function $L(y_i, \gamma_i)$. An initial "guess" model F_0 is created. An estimator function h is added to it creating the second stage model F_1. The difference between the new and old models is a measure of the loss function L. The estimator h can be found by minimizing the loss function and the process can then be iterated for an even more accurate predictor. More formally the recurrence between the k and $k + 1$ stages of the models can be written as [6]:

$$F_{k+1} = F_k + \arg\ min\left[\sum_i \left(L\left(y_i, F_k(x_i) + \gamma_{k+1} h_{k+1}(x_i)\right)\right)\right]$$

by minimizing the loss function

$$F_{k+1} = F_k - \gamma_{k+1} \sum_i \left[\frac{\partial L\left(y_i, F_k(x_i)\right)}{\partial F_k(x_i)}\right] \quad (9)$$

where γ_{k+1} is given by:

$$\gamma_{k+1} = \arg\min \sum_i L\left(y_i, F_{k+1}(x_i)\right)$$

The algorithm was implemented using *sklearn's ensemble.GradientBoostingRegressor()*.

LGBM regressor

Light Gradient Boosting Model is a type of gradient boosting framework based on decision trees to increase the efficiency of the gradient boosting model. LGBM uses Gradient-based One Side Sampling (GOSS) and Exclusive Feature Bundling (EFB) which overcome the shortcomings of regular gradient boosting algorithms. GOSS keeps under-trained data instances (i.e. the instances with large gradients that affect the performance of the model the most) and randomly drops instances with small gradients to retain the accuracy of information. This treatment can lead to a more accurate gain estimation than uniformly random sampling, with the same target sampling rate. In a sparse feature space, many features are mutually exclusive, i.e., they never take nonzero values simultaneously. The exclusive features can be safely bundled into a single feature called an Exclusive Feature Bundle.

The regressor was implemented using *sklearn's lightgbm.LGBMregressor()* [7].

Model Evaluation

After training the model on the dataset it is necessary to test its accuracy. To assess and compare the various trained models we used the standard statistical r^2 scoring metric. If y_i and f_i represent the true values and predicted values of the data and if $\bar{y}$ is the average of the true values, the coefficient of determination or R^2 is defined as

$$r^2 \equiv \left(1 - \frac{u}{v}\right) \quad (11)$$

where u is the residual sum of squares, $u \equiv \sum_i (y_i - f_i)^2$, and u is the total sum of squares, $u \equiv \sum_i (y_i - \bar{y})^2$. We shall henceforth use r^2 and model accuracy interchangeably.

To evaluate and score the models we used the *sklearn* library's inbuilt function *linear_model(). Linearregression().score()*.

RESULTS AND DISCUSSION

On a comparative analysis it was found that the model which attained the highest accuracy was Light Gradient Boosting regressor while the least accurate one was Ridge linear regressor. In general linear regressors performed worse than decision tree and gradient boosting regressors, which is quite natural because of the inefficiencies of linear regression algorithms. The predictions of the different models are discussed in more detail as follows:

Linear regressors

The linearly trained models were the worst performing of the models evaluated, which is reasonable considering the relatively small linear regression coefficients between the mass and energies. The simple linear regression model was only able to achieve a model accuracy of 29.26%. From Fig. 4 we see that even the most significant variables do not show a strong linear correlation with the target variable. This elucidates the necessity for using non linear regressors like decision tree or gradient boost. Fig. 6 shows the kernel density estimate of the invariant mass PDF as predicted by the model trained on linear regression algorithm.

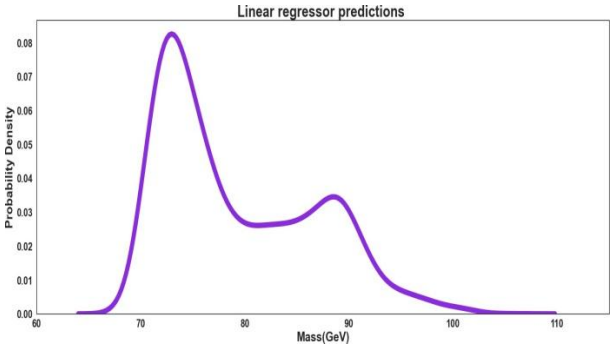

Figure 6: PDF for invariant mass as predicted by linear regression model.

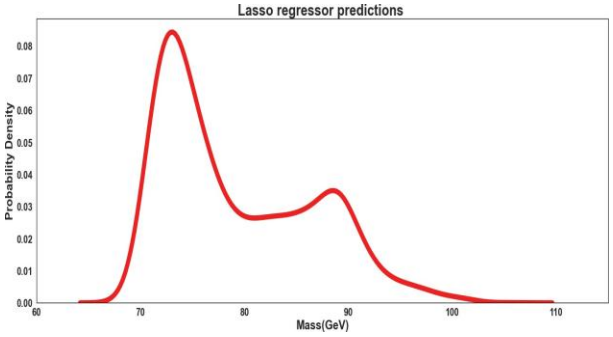

Figure 7: PDF for invariant mass as predicted by the lasso linear regression model.

Lasso and Ridge linear regressors had an even worse performance than the simple linear regression model, with model accuracies of 29.23% and 29.26% respectively. The possible explanation of this could be in the fact that lasso and ridge use an overall worse fitting regression line than the normal linear model. This bias in the fit reduces the overall variance but may also contribute to worse performances, especially for non linear data. The difference between lasso and ridge predictions can be explained on the basis of the order of the biasing terms in the two: for lasso biasing is of the order $O(w_j)$ while ridge has a bias term of the order $O(w_j^2)$, where w_j is the fitting coefficient (slope) for the parameter x_j. As speculated before, the more the bias, the worse is the prediction of the model. Fig. 7 and 8 show the predicted PDFs for lasso and ridge linear regressors respectively.

Decision tree regressor

The decision tree regression model was able to perform significantly better than the linear regressors with an overall model accuracy of 79.01%. The higher performance can be ascribed to the indifference of decision tree models to non linearity and outliers. The innacuracies in the model may be attributed to the tendency of decision tree to overfit the data. Fig. 9 shows the model prediction for the invariant mass PDF by decision tree model.

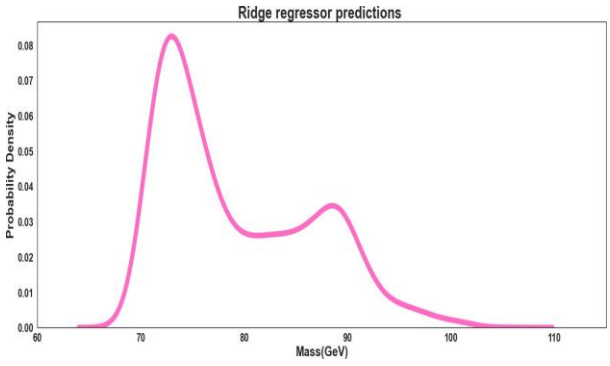

Figure 8: PDF for invariant mass as predicted by the ridge linear regression model. Notice that many defining features of the original PDF like the Z^0 peak are absent in all the linear models.

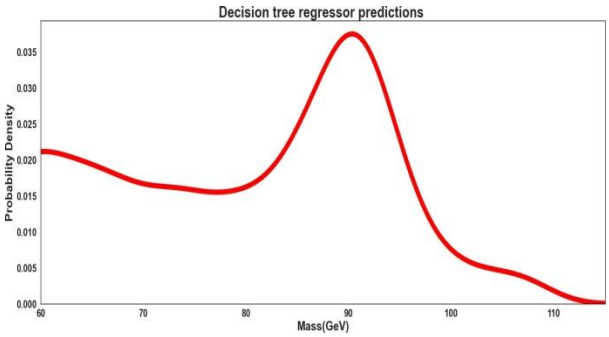

Figure 9: PDF for invariant mass as predicted by the decision tree regression model. The prediction follows the original PDF much more closely than the linear regressors.

Gradient Boosting regressors

The gradient boosting algorithms were overall the best performing ones. The simple gradient boost regressor was able to achieve a model accuracy of 80.42%. Fig. 10 shows the PDF prediction by gradient boosting algorithm based model.

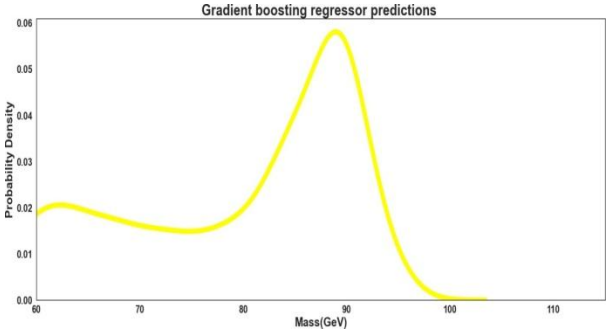

Figure 10: PDF for invariant mass as predicted by the gradient boosting regression model.

The Light Gradient Boosting Model (LGBM) regressor was the best performing model of the models evaluated, with a model accuracy of 92.34%. Gradient boosting models already incorporate within them attributes of linear and decision tree models and the iterative correction helps them achieve their high accuracy. Fig. 11 shows the predicted mass PDF made using the LGBM regressor.

If one desires even higher accuracy there are more advanced regression algorithms like CatBoost which require more computing power.

CONCLUSION

This paper set out to show the utility of machine learning techniques through the example of a physical problem. An exploratory data analysis of the dataset revealed that the invariant mass of a dielectron system is most significantly dependent on the energies of the particles E_1, E_2 and their transeverse momenta p_{T1} and p_{T2}. In the regression models evaluated, the LGBM regressor showed the highest model accuracy of 92.34%. Figure 12 shows a comaprative plot between the original mass PDF and the one predicted by the LGBM regressor; it can be seen that the high energy peak is predicted very well even though the model suffers from inaccuracies at low masses. Models which used linear regression performed significantly worse than classifier regressors like decision tree regressor and non linear gradient boosting models like LGBM. It is recommended to use even more advanced regression algorithms like CatBoost if more accurate model is required. The predictor models can be used as a test to distinguish abnormal events from regular ones.

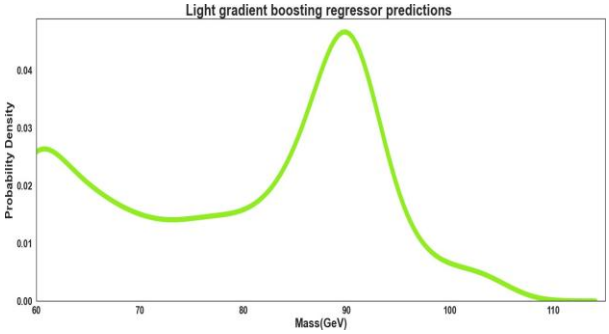

Figure 11: PDF for invariant mass as predicted by light gradient boosting regression model. The PDF follows the observed PDF quite closely, attesting to the accuracy of the model.

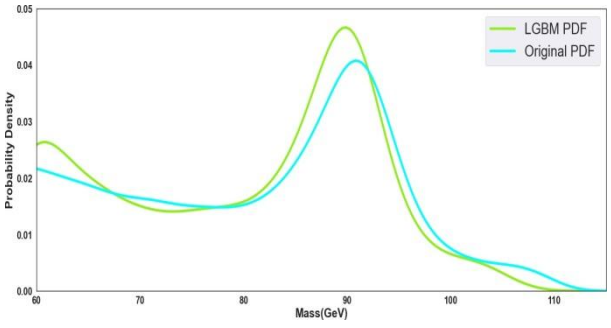

Figure 12: Comaprison between the original PDF and the one predicted by light GBM regressor, the best performing regressor from the models analyzed

REFERENCES

McCauley T. “Events with two electrons from 2010”. In: *CERN Open Data Portal* (2014).

Shreyasi Acharya et al. “Dielectron production in proton-proton collisions at $s = \sqrt{s} = 7\ TeV$”. In: *Journal of high energy physics* 2018.9 (2018), pp. 1–47.

Vincenzo Chiochia. *Phenomenology of Particle Physics Chapter 4, ETH, Zurich*. 2010. URL: https://edu.itp.phys.ethz.ch/hs10/ppp1/.

Lars Buitinck et al. “API design for machine learning software: experiences from the scikit-learn project”. In: *arXiv preprint arXiv:1309.0238* (2013).

Fabian Pedregosa et al. “Scikit-learn: Machine learning in Python”. In: *the Jour- nal of machine Learning research* 12 (2011), pp. 2825–2830.

Trevor Hastie et al. *The elements of statistical learning: data mining, inference, and prediction*. Vol. 2. Springer, 2009.

Guolin Ke et al. “Lightgbm: A highly efficient gradient boosting decision tree”. In: *Advances in neural information processing systems* 30 (2017).

PARAMETER FITTING IN A THEORETICAL MODEL EMBLEMATIC OF PREDICTIVE NATURE

Pooja Kaushal*

Centre for Medical Physics, Panjab University, Chandigarh-160014, India

ABSTRACT

Dynamical Cluster-decay Model (DCM) is a Quantum Mechanical Fragmentation Theory-based non-statistical theoretical model, that uses collective clusterization approach, to investigate the role of shell effects in cluster radioactivity, fusion and fission phenomena observed in heavy-ion reactions at low energies. DCM uses only one fitting-param00eter, *viz.*, the neck-length (barrier-lowering) parameter, ΔR, which is a measure of the distance of closed approach (minimum separation distance) of the two deformed and oriented nuclei involved in a nuclear reaction. In any heavy-ion reaction, the parameter best fits the observed experimental decay channel cross sections and simultaneously enables one to predict non-compound nucleus (nCN) and fusion-fission (ff) cross sections. The trends of compound nucleus formation, P_{CN} and survival probability, P_{surv} *w.r.t.* compound nucleus excitation energies, E^*_{CN} give credence to the predicted nCN and ff cross sections. Interestingly, the prediction of possible target-projectile combinations for the formation of any radioactive or non-radioactive compound nucleus is nearly independent of ΔR-value. Furthermore, the near constancy or smooth variation of ΔR-values with E^*_{CN} obtained in decay analysis of a compound nuclear system, formed via various reactions, where experimental results are available, enables one to make valuable predictions. For instance, this independence of ΔR-values *w.r.t.* entrance channel nuclei, can be utilized to predict channel cross sections, σ_{xn} for decay of the *same* compound nucleus formed by a *different* target-projectile combination for which experiments have not been performed yet. Quoting a specific result to further highlight DCM's predictive nature; an important outcome is obtained when the ΔR-value is attained for an exact fit of the (total) fusion cross section $\sigma_{fus} = \sum_{x=1}^{6} \sigma_{xn}$ for ^{9}Li projectile on ^{208}Pb target at a given laboratory energy, E_{Lab}. The use of *same* ΔR-value at the *same* laboratory energy E_{Lab}, as for the decay of ^{217}At* formed in ^{9}Li+^{208}Pb reaction, almost exactly fits the (total) fusion cross section, σ_{fusion} for all other ^{9}Li induced reactions on different targets. Such a result could be used to predict σ_{fusion} for ^{9}Li-induced reactions where experimental data are not available. This article unveils the predicting potential of DCM with an elaborate discussion on all the above mentioned aspects using various compound nuclear systems.

Keywords: Heavy-ion reactions, Quantum Mechanical Fragmentation Theory, Dynamical Cluster-decay Model, ΔR-parameter, compound nucleus formation probability, compound nucleus survival probability

INTRODUCTION

Heavy-ion reactions at low energies involve formation of compound nuclei with energy per nucleon, E/A < 15 MeV/A. The highly excited compound nucleus so formed carries large angular momentum and decays by emitting light particles (n, p, α) and γ-rays. This evaporation residue cross section, σ_{ER} is accompanied by the intermediate mass fragments, σ_{IMF} with masses $5 \le A \le 20$ and charges $2 < Z < 10$, near symmetric fission (nSF) and symmetric fission (SF) components. The contribution of IMFs, also known as "complex fragments" or "clusters" is however small, i.e., $\sigma_{IMFs} \approx$ 5-10% σ_{ER}. So depending upon the mass of compound nucleus formed, different combinations of above three processes are possible. It may happen that any one of the three (ER, IMFs and ff) is the dominant decay mode. Fusion-fission cross-section, σ_{ff} comprises of IMFs, SF and nSF components, i.e., $\sigma_{ff} = \sigma_{IMF} + \sigma_{SF} + \sigma_{nSF}$. Thus, the CN formation cross section, σ_{CN} is the sum of ER and ff cross sections, $\sigma_{CN} = \sigma_{ER} + \sigma_{ff}$. Hence, the probability that the fused system will de-excite by emission of neutrons or light particles (equivalently, the Evaporation Residue) rather than fission, is the compound nucleus survival probability P_{surv} (Chopra *et al.*, 2015), defined as

$$P_{surv} = \frac{\sigma_{ER}}{\sigma_{CN}} = \frac{\sigma_{ER}}{(\sigma_{ER} + \sigma_{ff})} \tag{1}$$

For instance, compound nuclear systems such ^{117}Sb* (Kaushal, 2020) and ^{120}Te* (Kaushal, 2020) have evaporation residues (mainly neutrons) as the predominant decay mode. So, for fissionless decay,

Corresponding author: poojaphysics7@gmail.com
Received: September 16, 2022, Accepted: November 15, 2022

P_{surv} = 1. For $^{215}Fr^*$, $^{220}Th^*$ and $^{246}Bk^*$ compound nuclei, P_{surv} increases with increasing excitation energy E^*_{CN} (see, for instance, Fig. 9(c)). This happens because of the strongly differing relative magnitudes of σ_{ER} and σ_{ff} and their variations with E^*_{CN} (refer Fig. 4 in Chopra *et al.*, 2015). For $^{202}Po^*$ (Morton *et al.*, 2000; Rafiei *et al.*, 2008), P_{surv} decreases with increasing E^*_{CN}. This essentially means that fission becomes more prominent, i.e., the fusion-fission component, σ_{ff} increases with increasing E^*_{CN}. P_{surv} = 0 when fission constitutes the predominant decay mode, implying that no neutron or light particle emission occurs.

Further, if a compound nucleus with excitation energy ranging 10−20 MeV, de-excites via emission of 1−2 neutrons, it is known as "cold fusion" reaction as for $^{117}Sb^*$ and $^{120}Te^*$. Cold fusion reactions are characterized by lowest interaction barrier accompanied by largest interaction radius with elongated, "non-compact" nuclear shape (refer Fig. 5 (a,d)). On the other hand, $^{202}Po^*$(Kaushal and Sharma, 2019), $^{217}At^*$ (Kaur *et al.*, 2017) and $^{220}Th^*$ (Hemdeep *et al.*, 2018) involve "hot fusion" phenomena as the compound nucleus excitation range is 40−50 MeV for these nuclei and the emitted number of neutrons are more than 2. Hot fusion reactions involve largest interaction barrier and smallest (most compact) interaction radius corresponding to "compact" nuclear shape (see, for instance, Fig. 5 (b,c)).

It has been observed experimentally that on the basis of excitation energy, angular momentum and mass asymmetry [associated with the product (Z_pZ_t) of the atomic numbers of the projectile (Z_p) and target (Z_t)] of the entrance channel, the resultant composite system of a heavy-ion collision, may either form an equilibrated compound nucleus or the projectile gets captured by the target for a short duration of time, reseparating prior to the evolution of the final equilibrated compound nucleus. The charge product Z_pZ_t of the entrance channel is another major factor that plays a decisive role in dynamical evolution of trajectories of heavy-ion reactions. Theoretical explanation of asymmetric shape, taking into account the fragment shell properties, was given by Meitner as early in 1950 (Meitner, 1950). Fission dynamics of different isotopes of a nucleus, neutron to proton ratio (N/Z) and contributions from near scission configurations are other major factors that affect the fusion-fission dynamics. Therefore, these low energy heavy-ion reactions can further be categorized as (i) fusion reactions and (ii) fusion-fission reactions. Fusion reactions are pure compound nucleus processes. Here absolute transmittal of mass, kinetic energy, and angular momentum takes place between the entrance channel. The complete rotation of the composite system so formed results in the formation of a fully equilibrated compound nucleus with complete identity loss of the interacting entities. The hot and rotating compound nucleus then decays via the processes (ER, IMF, ff) already discussed earlier. The next category comprises of the Fusion-fission reactions wherein the pure compound nucleus-content is small. These primarily include fusion-fission (ff) and non-compound nucleus (nCN) contributions. In heavy ion collisions, forming of evaporation residues (ER) is profoundly repressed by fission and quasi-fission-like non-compound nucleus (nCN) processes (Swiatecki, 1981; Bjornholm *et al.*, 1982; Blocki *et al.* 1986). These nCN processes could be quasi-fission (qf), Deep Inelastic Collision (DIC), fast fission and Incomplete Fusion (ICF). The beam energy and mass-asymmetry of the entrance channel nuclei (target-projectile) play a decisive role in differentiating these nCN processes from one another.

So, the (total) fusion cross section comprises of compound nucleus (CN) and quasi-fission (qf-like) non-compound nucleus (nCN) components and is defined as, σfusion = σCN + σqf, with σCN as the CN formation cross section (sum of ER and ff cross sections, σCN = σER + σff), and σqf as the non-compound nucleus, quasi-fission cross section. Hence, the (total) fusion cross section is essentially the sum of ER, ff and qf components, i.e., σfusion = σER + σff + σqf . As in Eq. 1, one can define compound nucleus fusion/ formation probability, PCN (Kaur *et al.*, 2014) as :

$$P_{CN} = \frac{\sigma_{CN}}{\sigma_{fusion}} = 1 - \frac{\sigma_{nCN}}{\sigma_{fusion}} \tag{2}$$

The sticking time is another major factor that determines the future of the composite system after collision of target and projectile. It is anticipated that the sticking time is associated with compound nucleus formation probability, P_{CN} . For the case of fission following fusion, the projectile-target system sticks together for additional period (10^{-18}–10^{-16} sec) and typically completes several collisions/rotations. However, if the time of interaction is short ($\sim 10^{-20}$

sec), the system splits into fragments before a complete equilibration. It can be readily inferred from Eq. 2 that P_{CN} = 1 when contribution from non-compound nucleus processes is zero, which leads to the formation of a pure compound nucleus. However as non-compound nucleus processes start to dominate, the value of P_{CN} decreases from its maximum value of unity (see Fig. 9(b)). For instance, $P_{CN} << 1$ for $^{217}At^{*}$ formed in $^{9}Li+^{208}Pb$ reaction (Kaur *et al*., 2017). σ_{nCN} contributes towards most (99%) of the σ_{fusion} at all the considered incident energies. Theoretical analysis indicates that ^{9}Li projectile gets captured by the target nucleus prior to Coulomb barrier penetration. This results in transfer of few nucleons between them instead of complete capture. This process is similar to quasi-fission (qf)-like non-compound nucleus (nCN) process. Thereafter, the system approaches to N/Z equilibrium. It is evident from above discussion that P_{CN} (Eq. 2) takes care of nCN effects and P_{surv} (Eq. 1) looks after the ff processes.

So, in order to interpret the true nature of any experimental data, a theoretical model with good "quantum numbers" or "degrees-of-freedom" is necessary. One such model to investigate heavy-ion reactions at low energies in terms of quantum mechanical fragmentation theory (QMFT) (Maruhn *et al*., 1974; Gupta *et al*., 1975; Gupta *et al*., 1999) is the dynamical cluster-decay model (DCM).

Dynamical cluster-decay model

Based on QMFT, the theoretical models are broadly classified as (i) the cluster models, where the preformation probability, $P_0 \neq 1$, and (ii) the fission models, where $P_0 \approx 1$. Inclusion of preformation probability attributes structure effects in the decaying nucleus. Thus, in case of cluster decay, it is assumed that the cluster gets pre-formed in the mother/decaying nucleus prior to its penetration into the nuclear interaction barrier. This aspect is completely ignored in fission models. DCM (Gupta *et al*., 2005; Singh *et al*., 2008; Sharma *et al*., 2011) is a QMFT-based cluster model based on the assumption that the heavy clusters are assumed to be pre-born inside the parent nucleus prior to their penetration across the interaction potential barrier with respective Q-value. DCM uses only one parameter, the neck-length, ΔR. It is the value of this parameter that fixes both preformation and penetration points of the resulting interaction potential of the incoming/outgoing fragments. The model has been successfully applied over the years to study the compound nucleus formation, P_{CN} , and survival probabilities, P_{surv} at various center-of-mass energies. Thus, formation and decay mechanism of various compound nuclear systems can be effectively understood within the framework of DCM. Apart from using the available experimental data for drawing conclusions regarding the decay mechanisms involved in a particular heavy-ion reaction, the model is also capable of making predictions. This article mainly highlights the predicting potential of DCM using various compound nuclear systems: (i) Use of DCM in prediction of various target-projectile combinations for formation of "cold" nuclei is illustrated using $^{117}Sb^{*}$ and $^{202}Po^{*}$. This prediction is independent of ΔR-value. (ii) Prediction of non-compound nucleus and fusion-fission cross sections in compound nucleus decays is demonstrated using $^{220}Th^{*}$ formed in various heavy-ion reactions that include ^{16}O + ^{204}Pb, ^{40}Ar + ^{180}Hf, ^{48}Ca + ^{172}Yb and ^{82}Se + ^{138}Ba target-projectile combinations. Near constancy or smooth variation of ΔR-values with compound nucleus excitation energy, E^{*}_{CN} , is employed for this purpose. (iii) Finally, how DCM can be used to make predictions at energies where experimental data is not available is illustrated using $^{217}At^{*}$ compound nucleus formed in $^{9}Li+^{208}Pb$ hot fusion reaction. Here empirical value of the parameter, ΔR, at a fixed value of laboratory energy, E_{Lab} is obtained for an exact fit of the experimental (total) fusion cross section $\sigma_{fus} = \sum_{x=1}^{6} \sigma_{xn}$ corresponding to decay of $^{217}At^{*}$ formed via ^{9}Li + ^{208}Pb target-projectile combination. The *same* ΔR-value at the *same* laboratory energy is then used to predict the total fusion cross sections for ^{9}Li-induced reactions on different targets where experimental data are not available. All these aspects are elaborately discussed in subsequent sections after a detailed account of model's theory.

THEORETICAL MODEL

DCM is a non-statistical model used to interpret decay of hot and rotating compound nuclei formed in low-energy heavy-ion reactions. A semi-empirical statistical relation relates the nuclear temperature T (in MeV) to the CN excitation energy, E^{*}_{CN} (in MeV), as:

$$E^{*}_{CN}=E_{c.m.}+Q_{in}=(A/a)T^2-T \quad (3)$$

The parameter A/a is proportional to the nucleon number of the nucleus (LeCourteur and Lang, 1959; Okuducu, 2006), where the empirical constant "a" can take values from 9-11 depending upon the compound nucleus mass, A. Qin is the entrance or incoming channel Q value. In DCM, the emissions of light particles, intermediate-mass fragments, as well as fusion-fission fragments are treated on equal footings and that the heavy clusters are assumed to be pre-born inside the parent nucleus prior to their penetration across the interaction potential barrier with respective Q value. The probabilities of pre-formation inside the parent nucleus vary for clusters of different size/mass. Also, the barrier assault frequencies differ minutely for distinct clusters. So, decay is supposed to be a non-adiabatic and sudden process that occurs in two steps: (i) the cluster formation inside the parent nucleus and (ii) penetration of these preformed clusters through their respective interaction potential barriers. The basic approach is that the emitted cluster(s) are preborn/pre-formed in the parent nucleus with certain probability, which decreases as the size of cluster increases, thereby suggesting that the cluster-decay process will somewhere stop and that the fission process will take over. Since for cluster models, the preformation probability, Po ≠ 1, the nuclear structure aspect is taken care of in these models. For each value of angular momentum, ℓ, the preformation yields P0(Ai) of fragments Ai are given by the solution of the stationary Schrödinger equation in mass (and charge) asymmetry coordinates η, at a fixed R = Ra (the point of barrier penetration, refer Fig. 3)

$$\left\{-\frac{\hbar^2}{2\sqrt{B_{\eta\eta}}}\frac{\partial}{\partial\eta}\frac{1}{\sqrt{B_{\eta\eta}}}\frac{\partial}{\partial\eta}+V(R,\eta,T)\right\}\psi^{\nu}(\eta)=E^{\nu}\psi^{\nu}(\eta) \quad (4)$$

with ν = 0,1,2,3,... referring to ground-state (ν = 0) and excited-state solutions. The mass parameters, $B_{\eta\eta}$, are the smooth classical hydrodynamical masses, since at large T-values the shell effects are almost completely washed out. The preformation probability is $P_0(A_i)=|\psi_R(\eta(A_i))|^2\sqrt{B_{\eta\eta}}\frac{2}{A}$. The collective fragmentation potential V(R,η,T) in Eq. (4), which brings in the structure effects of the compound nucleus into the formalism, is calculated according to the Strutinsky renormalization procedure (B = V_{LDM} + δU; B is binding energy), as

$$V_R(\eta,T)=-\sum_{i=1}^{2}\left[V_{LDM}(A_i,Z_i,T)+\delta U_i\exp\left(-\frac{T^2}{T_0^2}\right)\right]+V_P(R,A_i,\beta_{\lambda i},\theta_i,\phi,T)$$
$$+V_C(R,Z_i,\beta_{\lambda i},\theta_i,\phi,T)+V_\ell(R,A_i,\beta_{\lambda i},\theta_i,\phi,T), \quad (5)$$

where V_C, V_P , and V_ℓ are the temperature- and orientation-dependent Coulomb, nuclear proximity and angular-momentum-dependent potentials, respectively (Gupta *et al*., 2005). δU are the empirical shell corrections , made T dependent to vanish exponentially with T_0 = 1.5 MeV (Jensen and Damgaard, 1973) and V_{LDM} is T -dependent liquid drop energy. The experimental binding energies split into V_{LDM} and δU components, incorporate the deformation effects of nuclei.

DEGREES-OF-FREEDOM :

In DCM, decay of a hot and rotating compound nucleus at temperature T and having angular momentum ℓ , is worked out in terms of (i) mass (and charge) asymmetries η = $(A_1 - A_2)/(A_1 + A_2)$ [and η_Z = $(Z_1 - Z_2)/(Z_1 + Z_2)$], (ii) relative separation coordinate R, (iii) multipole deformations $\beta_{\lambda i}$ (λ = 2,3,4; i = 1,2), (iv) orientations θ_i, and (v) the azimuthal angle ϕ, for the two nuclei, as shown in Fig. 1 for coplanar (ϕ = 0^o) and in Fig. 2 for non-coplanar (ϕ ≠ 0^o) configurations. The importance of inclusion of these important variables referred to as "quantum numbers" or "degrees-of-freedom" in the introduction is highlighted in the following text:

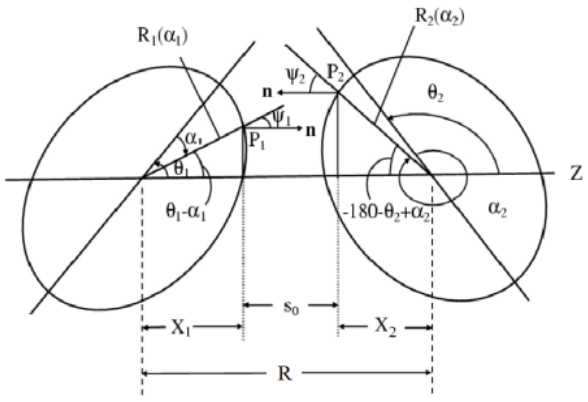

Figure 1: Schematic representation of two equal or unequal axially symmetric deformed, oriented nuclei, coplanar nuclei (ϕ = 0^0), both lying in the same plane, for various θ_1 and θ_2 values lying in the range 0^0 to 180^0 (Gupta *et al*., 2004).

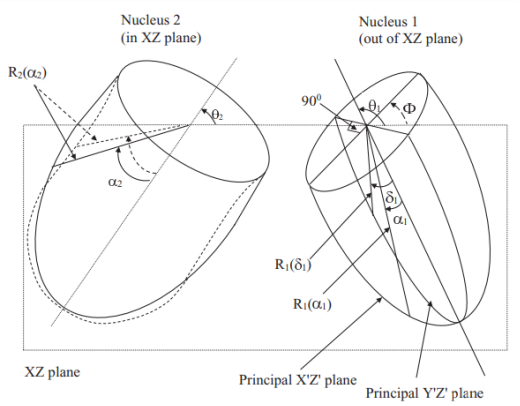

Figure 2: Two unequal nuclei (nucleus 1 is β_2 deformed and nucleus 2 is up to β_4), oriented at angles θ_1 and θ_2. Only the lower halves of the two nuclei are shown. Their principal planes X' Z' and XZ make an azimuthal angle ϕ, coming out of plane XZ, shown by a dashed line. Nucleus 2 is in the XZ plane and for the out-of-plane nucleus 1, another principal plane Y' Z', perpendicular to X' Z' plane, is also shown (Chopra *et al*., 2018).

(i) Mass (and charge) asymmetries:

Entrance channel mass asymmetry, $\eta = A_1-A_2/A_1+A_2$ (A_1, A_2 being mass numbers of the heavy and corresponding lighter nuclei, respectively) is an important quantity for understanding of the saddle point behaviour and its stability with respect to the Businaro-Gallone mass asymmetry, α_{BG} (Businaro *et al.*,1957). For $\eta < \alpha_{BG}$, mass transfer takes place from projectile to target nucleus resulting into dinuclear system that reseparates prior to is equilibration in all degrees of freedom, favoring more asymmetric shapes leading to quasi-fission. On the other hand, for $\eta > \alpha_{BG}$, the direction of mass drift is preferably in reverse order that leads to compound nucleus formation (Pant *et al*., 1996).

(ii) Relative separation coordinate:

The penetration of the preformed clusters is through the scattering potential V(R) which is the sum of deformations-orientations-and temperature-dependent Coulomb, nuclear proximity and angular momentum-dependent potentials, as

$$V(R,\ell,T) = V_c(R, Z_i, \beta_{\lambda i}, \theta_i, \Phi, T) + V_p(R, A_i, \beta_{\lambda i}, \theta_i, \Phi, T) + V_\ell(R, A_i, \beta_{\lambda i}, \theta_i, \Phi, T) \quad (6)$$

Thus, the interaction potential comprises of not only the repulsive Coulomb force, but also the attractive nuclear force, though short-ranged, but it is this force that plays a crucial role in compound nucleus formation process. In order to form a compound nucleus, the kinetic energy associated with the entrance channel should be sufficient enough to overcome the Coulomb barrier and come well into the nuclear attraction range. Depending upon the kinetic energy possessed by the colliding nuclei, the Coulomb barrier could either be crossed over or quantum mechanical tunneling of the barrier may occur. When the associated kinetic energy is not enough that the Coulomb barrier could be crossed, the composite system might not form a true compound nucleus. It then reseparates prematurely and decays via competing non-compound nuclear processes.

The scattering potential V (R) for a fixed η - value is illustrated in Fig. 3 for decay of $^{117}Sb^*$ compound nucleus to the ground state of ^{116}Sb via 1n-emission.

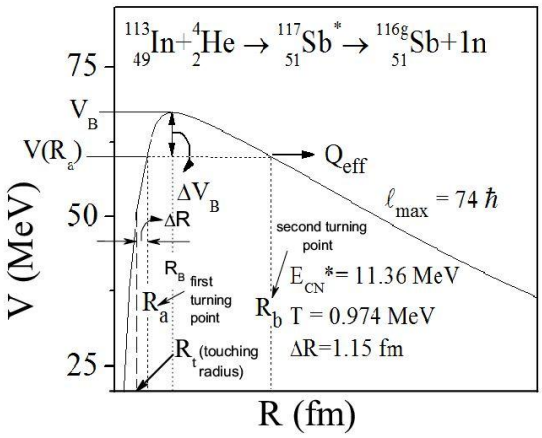

Figure 3: The scattering potential V (R) for decay of $^{117}Sb^*$ to the ground state of ^{116}Sb via 1n-emission for E^*_{CN} = 11.360 MeV (T = 0.974 MeV) at ℓ_{max} value. R_a and R_b, respectively, the first and second turning points, and $\Delta V_B = V(R_a)-V_B$, the barrier lowering parameter are also marked. The decay path is defined by V (R_a, ℓ) = Q_{eff} , beginning at R_a (= R_t + ΔR).

DCM involves the use of a single neck-length, ΔR parameter that attributes characteristic in-built barrier modification. For the decay of hot CN, the first turning point R_a, defining the point of fragment or cluster preformation P_0, and the penetration path for calculating penetrability P, is postulated by Gupta *et al.* (Gupta *et*

al., 2005; Gupta *et al*. 2006) as,

$$R_a(T) = R_1(\alpha_1,T) + R_2(\alpha_2,T) + \Delta R(\eta,T),$$
$$= R_t(\alpha,\eta,T) + \Delta R(\eta,T) \quad (7)$$

The temperature dependent ΔR(T), the neck-length [or barrier-lowering ΔV_B, refer to Eq. (10)] parameter, assimilates the deformation and neck formation effects between two nuclei, introduced within the extended orbiting cluster model of Gupta and collaborators (Khosla *et al*., 1990; Kumar and Gupta, 1997; Gupta *et al.* 1997). This method of introducing a neck-length parameter is similar to that used in the scission-point (Matuse *et al*., 1997) and saddle-point (Sanders, 1991; Sanders *et al*., 1999) statistical fission models. The R_i in Eq. (7) are the radius vectors given by

$$R_i(\alpha_i,T) = R_{0i}(T)\left[1+\sum_\lambda \beta_{\lambda i} Y_\lambda^{(0)}(\alpha_i)\right] \quad (8)$$

wherein T-dependent radii $R_{0i}(T)$ for the equivalent spherical nuclei (Royer and Mignen, 1992) are,

$$R_{0i}(T) = \left[1.28A_i^{1/3} - 0.76 + 0.8A_i^{-1/3}\right]\left(1+0.0007T^2\right) \quad (9)$$

Next, the potential at first turning point V (R_a,) is related to the top of the barrier $V_B(\ell)$ for each ℓ-value (refer Fig. 3), by defining their difference $\Delta V_B(\ell)$ as the effective lowering of the barrier

$$\Delta V_B(\ell) = V(R_a, \ell) - V_B(\ell) \quad (10)$$

Note, $\Delta V_B(\ell)$ for each ℓ is defined as a negative quantity since the actual barrier is effectively lowered. The parameter, ΔR, is generally positive but it can take negative values as well. The negative ΔR-value occurs as R_a (the first turning point of the penetration path) can always be chosen to start from $R_0(T)$ (radius for the equivalent spherical compound nucleus). Thus, the fitting parameter ΔR controls the barrier lowering and can take values such that $R_0 \le R_a \le R_B$, where R_B is the interaction barrier radius corresponding to barrier potential V_B (refer Fig. 3). The penetrability P in Eq. (13) or Eq. (14) is the WKB integral,

$$P = \exp\left[-\frac{2}{\hbar}\int_{R_a}^{R_b}\left\{2\mu\left[V(R,T) - Q_{eff}\right]\right\}dR\right] \quad (11)$$

solved analytically (Malik and Gupta, 1989), with the second turning point R_b [see Fig. 3] satisfying

$$V(R_a) = V(R_b) = Q_{eff}, \quad (12)$$

DCM can be applied to both positive and negative Q-value systems with appropriate inclusion of angular momentum and charge dispersion effects. For a given compound nucleus, the neck-length parameter in DCM is associated with the total kinetic energy. This effective Q-value is determined with regard to compound nucleus binding energy and the ground state binding energies of the emitted clusters/fragments (Gupta *et al*., 2002).

(iii) Multipole deformations:

Nuclear structure effects, which take into account the deformations of the fragments, strongly influence the heavy-ion reaction dynamics. In Heavy-ion reaction studies, the nuclear deformations of both the reaction partners play significant roles in determining the probability to form a compound nucleus. The higher order multipole deformations of the nuclei correspond to deviation from spherical nuclear shape. The nuclear deformations $\beta_{\lambda i}$ where λ=2,3,4 corresponds to quadrupole, octopole and hexadecapole oscillations of nuclear surface from its spheroidal shape (Fig. 4). The role of higher multipole deformations is of much interest as their inclusion leads to enhancement of fusion cross section in the synthesis of heavy and super-heavy nuclei (Sandulescu *et al*., 1997; Misicu and Greiner, 2004; Sawhney *et al*., 2011; Bao *et al*., 2016).

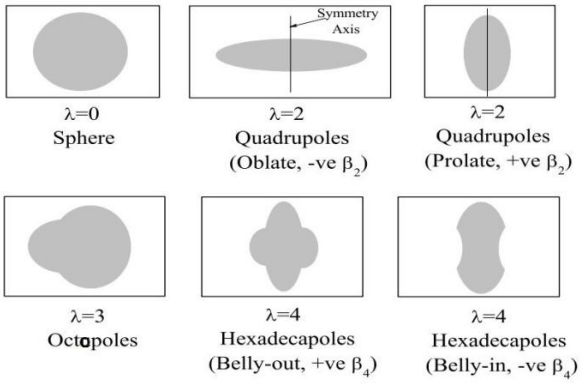

Figure 4 : Schematic diagram illustrating various multipole deformations in nuclei.

(iv) Orientations :

It is important to note that while considering deformed configuration of a nuclear system, their corresponding

orientations *w.r.t.* each other cannot be ignored. It has been shown by Gupta and collaborators on the basis of QMFT collaborators (Maruhn *et al*., 1974; Gupta *et al*., 1975; Gupta *et al*., 1999) that in collisions of deformed oriented nuclei, the barrier height V_B, and interaction radius R_B (refer Fig. 3), *i.e*., the shape of nuclear interaction potential gets affected which leads to enhancement of fusion cross sections. Therefore, along with deformations, appropriate choice of orientations of nuclei is equally important to understand the dynamics of heavy-ion reactions under extreme conditions. The orientations of two deformed nuclei are illustrated in Figs. 2 and 3. The angles α_i of radius vectors are measured in the clockwise direction from the nuclear symmetry axis and the orientation angles θ_i are measured anticlockwise from the collision Z axis (refer Fig. 2 and 3). For β_{2i} deformations, "optimum orientations, θ_i^{opt}" are assigned to hot fusion and cold fusion reactions characterized by "hot (compact)" and "cold (elongated)" configurations, respectively, corresponding to highest interaction barrier (or smallest, most compact interaction radius) and lowest interaction barrier (or largest interaction radius). This is shown schematically in Fig. 5 for oblate (a,b) and prolate (c,d) deformed nuclei with corresponding 'cold-elongated' optimum orientation in (a),(d) and 'hot-compact' in (b),(c). The optimum orientation angles are taken from Table 1 of Gupta *et al*., 2005. The criteria used for 'optimum' orientations is fixed using the signs of quadrupole deformations, i.e., oblate, prolate or spherical of two interacting nuclei which is not influenced by the +ve/-ve signs of hexadecapole deformations. However, for inclusion of higher order deformations, say upto β_4, or more, the "compact orientations", θ_{ci} refer to collisions occurring at smallest interaction radius (Gupta *et al*., 2005; Gupta *et al*. 2006). The idea of compactness with the effects of hexadecapole deformations (β_4) included is illustrated in Fig. 6 for prolate deformed+spherical nuclei for different magnitudes of hexadecapole (β_4) deformation. "Compact configuration" for the case of "hot-compact" reaction occurs for the collision in the direction of the minor axis of the deformed nucleus. This happens at 90^o orientation for spherical+deformed nucleus considered as equatorial compact (ec) configuration. For the prolate deformed nuclei with "small" +ve β_4 or -ve β_4 value gives rise to the same "equatorial $\theta \sim 90^o$ compact" configuration. However, large +ve β_4 value for prolate deformed nucleus results in the "non-equatorial $\theta<90^o$ compact" configuration represented as nec. Therefore, for proper understanding of nuclear reaction dynamics, an explicit inclusion of deformation and orientation effects becomes extremely important. In QMFT based DCM (Gupta *et al.* 2005; Singh *et al*. 2008; Sharma *et al*. 2011), along with inclusion of temperature and angular momentum, the deformations and orientation effects of the reaction partners/decay fragments are taken care. The orientation of the projectile *w.r.t.* the target nucleus at the time of collision plays an important role in deciding the final outcome of such a collision. The lateral or sideways contact (analogous to high capture barrier) of the projectile with target fosters the formation of compound nucleus, whereas an elongated contact (analogous to a lower barrier) enhances the quasi-fission probability (Hinde *et al*. 1995; Hinde *et al*. 1996; Denisov *et al*. 2002; Hinde *et al*., 2002).

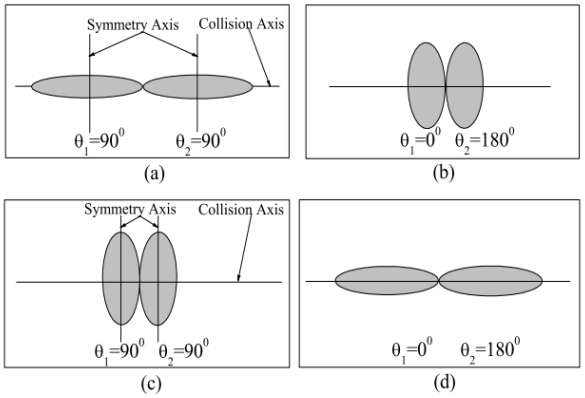

Figure 5: Schematic representation for deformed nuclei [(a),(b) oblate and (c),(d) prolate only] with corresponding "optimum orientations" for "cold, elongated" [(a), (d)] or "hot, compact"[(b), (c)] configurations, based on Table 1 of Gupta *et al*., 2005.

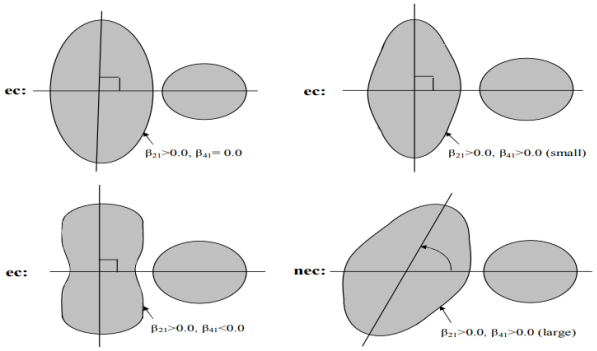

Figure 6: Representation of equatorial ($\theta=90^o$) and non-equatorial ($\theta<90^o$) "compact configurations" of prolate deformed+ spherical nuclei for different magnitudes of hexadecapole (β_4) deformation. This Fig. is taken from Gupta *et al*., 2006.

(v) Non-coplanarity :

In nature, deformed nuclei can however be oriented either in same plane ($\Phi = 0^0$, Fig. 1) or different planes ($\Phi_c \neq 0^0$, Fig. 2). The importance of non-coplanarity as an essential degree-of-freedom pertains to the fact that real or true outcome of a compound nucleus fusion reaction can be analyzed only by its inclusion (Chopra *et al.*, 2018). To calculate the cross sections for non-coplanar, $\phi \neq 0^\circ$ nuclei (refer to Fig. 2), the same formalism as for coplanar, $\phi = 0^\circ$ nuclei, discussed earlier is used wherein for the out-of-plane nucleus (i = 1 or 2), the corresponding radius parameter $R_i(\alpha_i)$ in Eq. 8 is replaced with its projected radius parameter $R_i^P(\alpha_i)$ in both Coulomb and nuclear proximity potentials (Manhas and Gupta, 2005). For the Coulomb potential, it enters via $R_i(\alpha_i)$, and for the proximity potential via the definitions of both the mean curvature radius $\bar{R}$ and the shortest distance s_0, i.e., the compact configurations with orientations θ_{ci} and ϕ_c. For further details, see Refs. (Gupta *et al*., 2005; Gupta *et al*.,2006).

CALCULATIONS AND RESULTS:

In terms of above noted coordinates, for partial waves, for each fragmentation (A_1,A_2), the CN decay or formation cross section is given by,

$$\sigma = \frac{\pi}{k^2}\sum_{\ell=0}^{\ell_c}(2\ell+1)P_0P; \qquad k=\sqrt{\frac{2\mu E_{c.m.}}{\hbar^2}} \tag{13}$$

where P_0 is the preformation probability referring to η motion at a fixed R-value and P, the penetrability, to R motion for a fixed η, both dependent on angular momentum ℓ and temperature T. μ is the reduced mass. ℓ_{max} is the maximum angular momentum, defined for light-particles evaporation residue cross section, $\sigma_{ER} \rightarrow 0$.

The same formula as above is applicable to the non-compound, quasi-fission (qf) decay process, where P_0 = 1 for the incoming channel since for qf process the target and projectile nuclei can be considered to have not yet lost their identities. Then, for P calculated as for the incoming channel η_{ic},

$$\sigma = \frac{\pi}{k^2}\sum_{\ell=0}^{\ell_c}(2\ell+1)P_{\eta c} \tag{14}$$

Thus, in DCM, the cross section for each (pair of) decay product is calculated as emission of preformed cluster(s) through their interaction barrier. Noting that Eq. (13) is defined in terms of the exit or decay channels alone, i.e., both the formation P_0 and then their emission via barrier penetration P are calculated only for decay channels (A_1, A_2), it follows from Eq. (13) that evaporation residue (ER) cross section is

$$\sigma_{ER} = \frac{\pi}{k^2}\sum_{x=1}^{4or5}\sigma_{xn} \tag{15}$$

and fusion-fission (ff) cross section is defined as

$$\sigma_{ff} = 2\sum_{A/2-x}^{A/2}\sigma_{(A_1,\,A_2)} \tag{16}$$

Based on above theory, the predictive potential of DCM is discussed in the following sections:

(i) Prediction of target-projectile combinations for compound nucleus formation :

DCM has been employed to identify possible "cold" target-projectile combinations for the synthesis of various radioactive and non-radioactive compound nuclear systems. The “cold” target-projectile (t,p) combinations refer to potential energy minima in the mass fragmentation potential V (A_i) (refer Eq. 5 and Fig. 7) of that particular compound nucleus. The mass fragmentation potential V (A_i) for the non-radioactive $^{117}Sb^*$ nucleus is presented in Fig. 7 for the optimum “cold fusion" configurations (Gupta *et al*., 2005) at compound nucleus excitation energy, E^*_{CN} = 11.36 MeV (equivalently, T = 0.974 MeV) at ℓ_{min}-value for a constant ΔR-value=1.1 fm. The "cold fusion" configurations are used here since DCM calculations are made in accordance with the experimental data (Yalçin *et al*., 2009) wherein $^{117}Sb^*$ decays via 1n emission for E^*_{CN} ranging from 11.36-14.72 MeV. It is important to note that the minimas obtained in V(A_i) refer to the possible (t,p) combinations, which are found to be nearly independent of ΔR-value (Niyti and Gupta, 2014). This means that even for a different value of the ΔR parameter, lying within the nuclear proximity limit of ~ 2.5 fm, the same combinations of target-projectile as in Fig. 7 will be obtained. The resulting “cold” (t,p) combinations (referring to minimas in V(A_i)) include:

^{4}He + ^{113}In, ^{6}Li + ^{111}Cd, ^{8}Be + ^{109}Ag, ^{12}C + ^{105}Rh, ^{19}F + ^{98}Mo, ^{23}Na + ^{94}Zr, ^{37}Cl + ^{80}Se, ^{40}Ar + ^{77}As, ^{43}K + ^{74}Ge, ^{46}Ca+^{71}Ga and ^{50}Ti+^{67}Cu. Interestingly, ^{4}He+^{113}In is one of the minima, the experimentally used target-projectile combination for ^{117}Sb* synthesis (Yalçin *et al*., 2009). Fig. 8 shows the corresponding scattering potentials V(R) (refer Eq. 6) for all the above DCM-proposed reactions forming ^{117}Sb* (enclosed within arrows). It is observed from Fig. 8 that the interaction barrier is the lowest for ^{6}Li + ^{111}Cd reaction and can be termed as the coldest fusion reaction for forming ^{117}Sb* since it lies the lowest in the graph. Therefore, the fusion cross section for ^{6}Li + ^{111}Cd combination is expected to be the largest. Also, ^{6}Li + ^{114}Cd target-projectile combination (Shroy *et al*., 1979) has been used by experimentalists to study ^{117}Sb. Along the same lines, "cold" target-projectile (t-p) combinations (referring to potential energy minima) are sought for the formation of radioactive ^{202}Po* in Fig. 7 corresponding to its mass fragmentation potential V(A_i). Here, the calculations are made for the compact "hot fusion" configurations (Gupta *et al*., 2006) at E^{*}_{CN} = 53.61 MeV, corresponding to ℓ_{max}-value for a constant ΔR = 1.1 fm using (β_{2i}–β_{4i}, θ_{ci}, $\Phi_c \neq 0^{\circ}$) configuration. The "hot fusion" configurations are used since DCM calculations are made for the available experimental data (Mayorov *et al*., 2014) wherein ^{202}Po* decays by emitting more than 2 neutrons for E^{*}_{CN} ranging $41 - 54$ MeV. Like for ^{117}Sb*, the minima in V (A_i) refer to the possible (t-p) combinations, which are also nearly independent of ΔR-value (Niyti and Gupta, 2014). The calculations are made for the "hot fusion" configurations supporting asymmetric fission. The resulting (t, p) combinations include: ^{6}He+^{196}Pb, ^{14}N+^{188}Ir, ^{24}Na+^{178}Ta, ^{27}Mg+^{175}Hf, ^{36}S+^{166}Er, ^{48}Ca+^{154}Gd, ^{66}Ni+^{136}Ba, ^{70}Zn+^{132}Xe, ^{83}Se+^{119}Sn, ^{88}Kr+^{114}Cd and ^{92}Sr+^{110}Pd. Interestingly, the experimentally used t-p combination, ^{48}Ca+^{154}Gd (Mayorov *et al*., 2014) is a minima in the V(A_i) graph. Fig. 8 shows the corresponding scattering potentials V(R) for all the above noted DCM-proposed reactions forming ^{202}Po* (enclosed within the arrows). The optimum (t-p) combination is one with lowest interaction barrier and smallest (most compact) interaction radius, which occurs for the most asymmetric ^{6}He+^{196}Pb combination, where both target and projectile are singly magic nuclei. Also, reactions induced by ^{6}He beams on ^{188,190,192}Os targets (Navin *et al*., 2004) have been analyzed experimentally. Note that it can be clearly seen from Fig. 8 that all cold-fusion reactions forming ^{117}Sb* have cold-elongated configurations and hence lie lower in the graph with longer interaction radius compared to all hot-fusion reactions forming ^{202}Po*. Thus, the QMFT-based DCM provides a theoretical basis for choosing (t–p) combinations for compound nucleus synthesis in the laboratory, which were otherwise chosen by the experimentalists on the basis of availability.

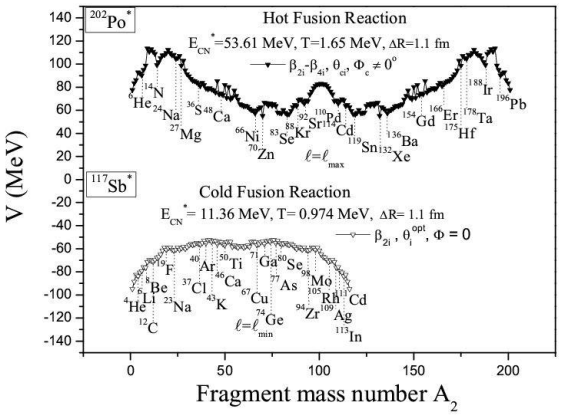

Figure 7 : Mass fragmentation potentials V(A_i), at ℓ_{min} value for ^{117}Sb* corresponding to E^{*}_{CN} = 11.36 MeV (equivalently, T = 0.974 MeV) and, at ℓ_{max} value for ^{202}Po* at E^{*}_{CN} = 53.61 MeV (T = 1.65 MeV), for a fixed ΔR = 1.1 fm, showing the possible target-projectile (t,p) combinations referring to minima in V (A_i).

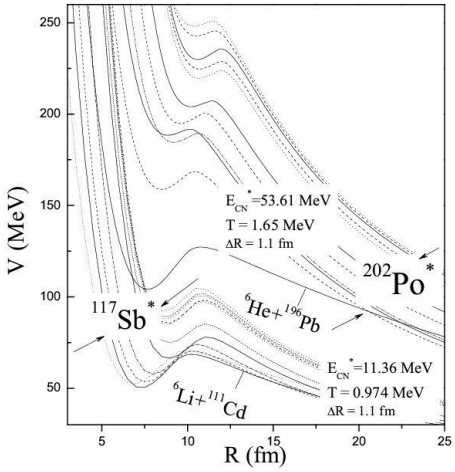

Figure 8 : Scattering potentials V(R) for "cold fusion" and "hot fusion" reactions noted in Fig. 7 for ^{117}Sb* and ^{202}Po* respectively. The "optimum" choice of t-p combinations is marked for both nuclei.

(ii) Prediction of non-compound nucleus and fusion-fission cross sections in compound nucleus decays:

The aim here is to demonstrate the above mentioned predicting capability of DCM using ^{220}Th* compound nucleus (Hemdeep *et al*., 2018). Experimental data for decay of ^{220}Th* formed in various entrance channel heavy-ion reactions ^{40}Ar + ^{180}Hf (Vermeulen *et al*., 1984; Kim *et al*., 2015), ^{48}Ca + ^{172}Yb (Sahm *et al*., 1985) and ^{82}Se + ^{138}Ba (Satou *et al*., 1985) is available. The radioactive ^{220}Th* formed via these entrance channels is a rare example wherein experimentally observed decay channels comprise of evaporation residues (ERs) consisting of light particles 3n, 4n, and 5n, with no fission component observed yet, over the compound nucleus excitation energy range *viz.* 25-47 MeV. Therefore, ^{220}Th* decay essentially involves "hot fusion" reaction configurations. Fig. 9(a) presents best-fitted ΔR-values that determine the first turning point R_a (refer Eq. 7 and Fig. 3), fitted empirically for each decay-channel cross section σ_{xn} at each E^*_{CN} for all the three reactions using higher order deformations, β_{2i}–β_{4i} with "compact" orientations θ_{ci} and $\phi \neq 0^{\circ}$, as a function of E^*_{CN}. Different ΔR-values for each decay channel represent different reaction times for different decay channels. Interestingly, independent of either the entrance channel or of CN excitation energy E^*_{CN}, ΔR-values remain nearly of constant value: ΔR^{CN}_{3n} = 1.86 ± 0.10, ΔR^{CN}_{4n} = 2.78 ± 0.02, and ΔR^{CN}_{5n} = 2.64 ± 0.07 fm for the pure compound nucleus process, and ΔR^{nCN}_{4n} = 1.18 ± 0.10 fm for the non-compound nucleus process. Note that the errors in ΔRs show larger deviations for pure CN decay via 3n and the nCN decay via 4n. Also, $\Delta R_{nCN} < \Delta R_{CN}$, i.e., the CN process occurs earlier than nCN on the reaction-time scale. This independence of ΔRs on both E^*_{CN} and entrance channel nuclei seems to be responsible for the above noted important result of the independence of the nCN cross section on entrance channel effects, despite the strongly varying channel cross sections σ_{xn} with excitation energy E^*_{CN} (see, e.g., Fig. 13 in Hemdeep *et al*., 2017).

Fig. 9(b) shows DCM-calculated compound nucleus formation probability P_{CN} (refer Eq. 2) as a function of excitation energy E^*_{CN} for the three entrance channels forming ^{220}Th* and the earlier studied case of ^{246}Bk* (Singh *et al*., 2008). The variation of P_{CN} with E^*_{CN} for strongly fissioning radioactive ^{220}Th* and ^{246}Bk* follow a similar trend. This indicates towards presence of nCN effects in ^{220}Th* which are observed only in 4n decay channel, 3n and 5n channels being pure compound nucleus decays (refer Fig. 9(a)). The variations of P_{surv} (Eq. 1) with E^*_{CN} is shown in Fig. 9(c) for three radioactive compound nuclei, *viz*., ^{220}Th* (three different entrance channels), ^{215}Fr* and ^{246}Bk*. As expected, P_{surv} increases with increasing E^*_{CN} in all cases owing to strongly differing relative magnitudes of evaporation residue and fusion-fission cross sections for all three radioactive nuclei (Also refer Fig. 4 in Chopra *et al*., 2015). Thus, the statistical characteristic properties for the decay of ^{220}Th* satisfy expected properties of a radioactive compound nucleus, giving credence to DCM calculations in predicting nCN and ff cross sections. It is to be noted that P_{CN} (Eq. 2) takes care of predicted nCN effects and P_{surv} (Eq. 1) looks after the predicted ff processes and similarity in their trends *w.r.t.* E^*_{CN} for radioactive nuclei of mass A_{CN}~200-250 supports DCM predicted nCN and ff cross sections.

Another point of interest to note from Fig. 9(a) is the role of magicity of the entrance channel reaction partners. It is noticed that for ^{48}Ca + ^{172}Yb reaction, involving doubly magic ^{48}Ca nucleus, the ΔR-values (filled circles) are the highest. Therefore, upper limits of ΔR will be more suitable for magic reaction partners. This is illustrated in Fig. 9(d) in predicting the decay channel cross sections $\sigma^{pred.}_{xn}$, for another reaction also forming ^{220}Th*, *viz*. ^{16}O + ^{204}Pb with both magic reaction partners, wherein only the evaporation residue cross sections $\sigma^{Expt.}_{ER}$ ($=\sum_{x=3}^{5}\sigma_{xn}$) are experimentally measured (Hinde *et al*., 2002). Note that the choice of x = 3 to 5 neutron channels is based on other reactions forming ^{220}Th* compound nucleus at similar excitation energies. Interestingly, DCM predicted sum ($=\sum_{x=3}^{5}\sigma_{xn}$) gives the measured σ_{ER} within a difference of a couple of percent. The upper limiting ΔR-values used in Fig. 9(d) for predicting cross sections for ^{16}O + ^{204}Pb reaction are ΔR^{CN}_{3n} = 1.96, ΔR^{CN}_{4n} = 2.80, ΔR^{CN}_{5n} = 2.71 and ΔR^{nCN}_{4n} = 1.28 fm. Thus, collective clusterization approach within DCM enables one to effectively predict non-compound nucleus and fusion-fission cross sections.

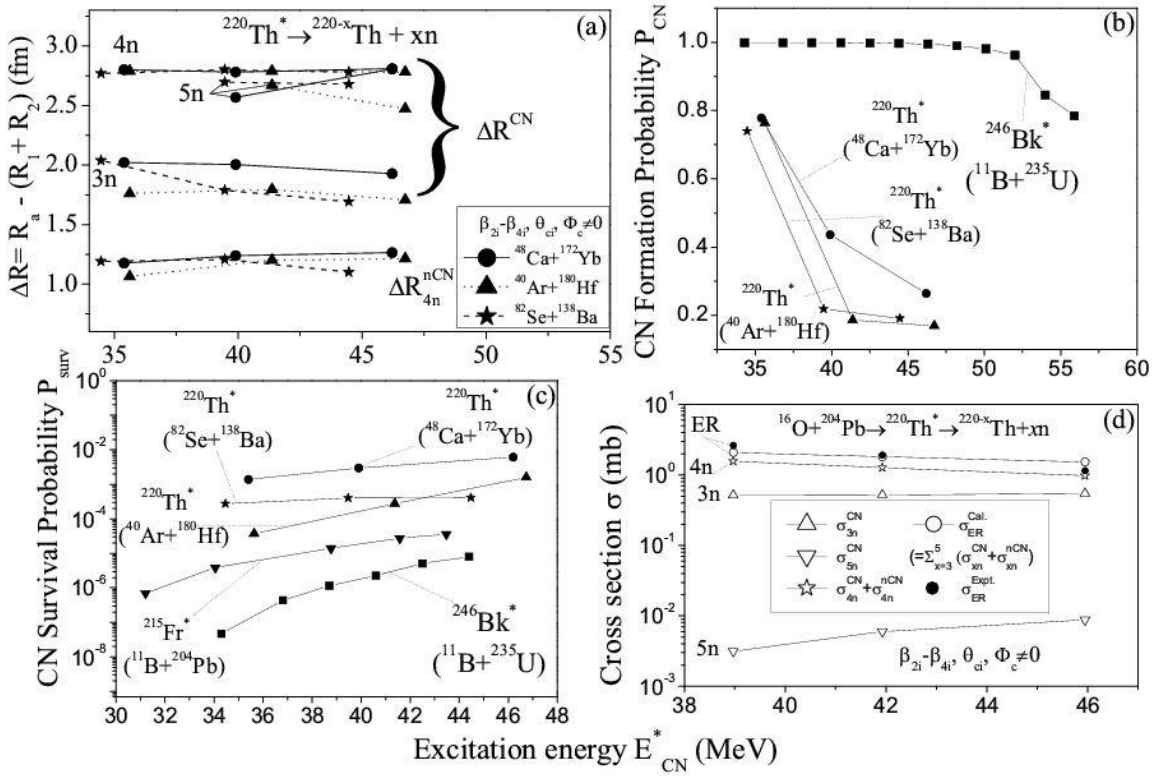

Figure 9: The variations of (a) best-fitted neck-length parameter ΔR for the CN and nCN processes in xn decays of ^{220}Th*, using higher-multipole deformations β_{2i}–β_{4i} with θ_{ci} for $\phi_c \neq 0^\circ$, for the three chosen reactions; (b) DCM-calculated P_{CN} and (c) P_{surv} compared with ^{215}Fr* and ^{246}Bk*; (d) DCM-predicted channel cross sections σ_{xn} and ER = $\sum_{x=3}^{5} \sigma_{xn}$ (open symbols) compared with experimental (Hinde *et al*., 2002) ER cross section σ_{ER} (filled circles); each as a function of E^*_{CN}.

(iii) Predictions at energies where experimental data is not available :

The aim here is to observe the behavior of a light neutron-rich radioactive beam (^{9}Li) on a doubly-magic target nucleus (^{208}Pb) for the (total) fusion cross section σ_{fusion} and analyze whether the results obtained can be used to make predictions elsewhere. The reaction ^{9}Li+^{208}Pb forming ^{217}At* is a "hot fusion" reaction since experimentally only the isotopic yield of heavy mass residues $^{211-214}$At* [equivalently, evaporation residue comprising of 3-6 neutrons] are measured. Therefore, the fusion-fission (ff) component, σ_{ff} is assumed to be negligible. For a fixed neck-length parameter ΔR, DCM calculations show that one is able to almost exactly fit $\sigma_{fusion} = \sum_{x=1}^{6} \sigma_{xn}$ for ^{9}Li on ^{208}Pb at all center-of-mass energies, $E_{c.m.}$ (Kaur *et al*., 2017).

Following an earlier work of Gupta and collaborators (Kaur *et al*., 2015) that for an empirically fixed neck-length parameter ΔR^{emp}, at a given incident laboratory energy E_{Lab}, an almost exact fit of the (total) fusion cross section $\sigma_{fusion} = \sum_{x=1}^{6} \sigma_{xn}$ for ^{9}Li projectile on ^{208}Pb and other targets is possible. The study therein shows that σ_{fusion} strongly depends on the target mass of the most abundant isotope and its (magic) shell structure. This result again shows the predictable nature of DCM. The neck-length parameter ΔR is *fixed empirically* for the decay of ^{217}At* formed in ^{9}Li + ^{208}Pb reaction at a *fixed* laboratory energy E_{Lab}, and then the total fusion cross section, σ_{fusion} is calculated for all other reactions using ^{9}Li as a projectile on different targets. Apparently, this procedure could be used to predict σ_{fusion} for ^{9}Li-induced reactions where experimental data are not available. Hence, the earlier work (Kaur *et al*., 2015) of the loosely bound projectile on different targets at the same beam energy is extended to calculate the total fusion cross sections σ_{fusion} for a given E_{Lab} energy at a fixed neck-length ΔR, using ^{9}Li as a projectile on ^{208}Pb target (Vinodkumar *et al*., 2009) and various isotopes of other targets (Al, Cu, Zn and Sn) from the intermediate energy regime of earlier experiments (Blank *et al*., 1993).

So, following the earlier works of Gupta and collaborators (Kaur *et al*., 2015), first the total fusion cross section for ^{217}At* formed in ^{9}Li + ^{208}Pb reaction at E_{Lab} = 29.86 MeV (equivalently, $E_{c.m.}$ = 28.5 MeV) is considered (Kaur *et al*., 2017). The best fitted neck-length parameter, for ^{9}Li + ^{208}Pb reaction at the above chosen E_{Lab}, is ΔR^{emp} = 1.556 fm. Now, using this ΔR-value, i.e., ΔR^{emp} = 1.556 fm, calculated for ^{9}Li + ^{208}Pb reaction forming ^{217}At* at E_{Lab} = 29.86 MeV, other most abundant and stable isotopes ^{27}Al, ^{67}Cu, ^{70}Zn and ^{120}Sn as targets, are chosen. The fusion cross section σ_{fusion} is then calculated for all of these ^{9}Li induced reactions at the above noted *fixed* value of neck-length parameter, ΔR^{emp} and *fixed* incident laboratory energy E_{Lab} = 29.86 MeV. Results of this calculation are presented in Fig. 10(a), compared with the experimental data for ^{217}At* and ^{79}As*. Apparently, this procedure could be used to predict the fusion cross section of ^{9}Li+^{120}Sn, ^{9}Li+^{67}Cu and ^{9}Li+^{27}Al reactions for which the experimental data are not available. Further, the calculated σ_{fusion} depends strongly on the target mass and its (magic) shell structure (refer Fig. 3 in Kaur *et al*., 2018), hence supporting DCM predictions. The above results of ^{9}Li induced reactions on different target nuclei are also utilized for another fixed value of ΔR^{emp} = 1.1777 fm and fixed beam energy E_{Lab} = 15 MeV, for ^{9}Li + ^{70}Zn (Loveland *et al*., 2006) and ^{9}Li + ^{208}Pb reaction (Vinodkumar *et al*., 2009) in Fig. 10(b). This result indicates that for empirically fixed ΔR-value, an almost same amount of modification in the barrier (refer Eq. 10) takes place in reactions induced by the same projectile (^{9}Li) possessing the same incident laboratory energy (E_{Lab}). Thus by systematic and detailed analysis, DCM can be employed to make predictions at energies where experimental data are not available.

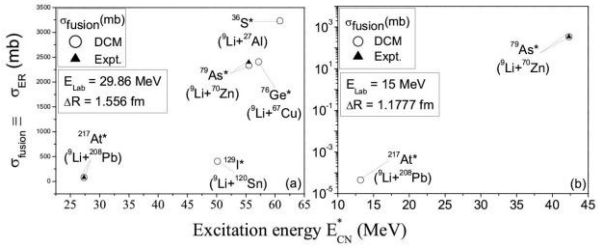

Figure 10: DCM-calculated σ_{fusion} (≡ σ_{ER}) for ^{9}Li induced reactions at (a) incident energy E_{Lab} = 29.86 MeV and for ΔR^{emp} = 1.556 fm, (b) Same as for (a) but for E_{Lab} = 15 MeV and ΔR = 1.1777 fm, compared with experimental data.

SUMMARY

Dynamical Cluster-decay model uses a non-statistical, collective clusterization approach to study heavy ion-reactions at low energies. The model is a quantum-mechanical fragmentation theory based cluster model wherein a compound nucleus decay involves a two step mechanism. Firsty, all possible decay fragments of a particular compound nucleus are considered to be pre-born inside the mother nucleus with certain preformation probabilities P_0, providing convincing knowledge regarding nuclear structure effects. Step two deals with penetration, as per the quantum concept of Gamow's α-decay theory, of these already preformed clusters through their respective interaction potential barriers with a tunneling probability *P*, obtained in R-motion using WKB-approximation. In DCM, decay of a hot and rotating compound nucleus at temperature T and having angular momentum ℓ, is worked out in terms of mass (and charge) asymmetries, relative separation coordinate, multipole deformations, orientations and non-coplanarity of the two nuclei. This article mainly highlights the predicting potential of DCM using ^{117}Sb*, ^{202}Po*, ^{220}Th* and ^{217}At* compound nuclear systems. Use of DCM in prediction of various target-projectile combinations for formation of "cold" nuclei is illustrated using ^{117}Sb* and ^{202}Po*. This prediction is independent of ΔR-value wherein ^{6}Li+^{111}Cd and ^{6}He+^{196}Pb were identified as the optimum target-projectile combinations for synthesis of ^{117}Sb* and ^{202}Po*, respectively. Predictions of pure compound nucleus (3*n*,5*n*), non-compound nucleus (4*n*) and fusion-fission cross sections are made in decay of ^{220}Th* formed via three heavy-ion reactions, *viz.* ^{40}Ar + ^{180}Hf, ^{48}Ca + ^{172}Yb and ^{82}Se + ^{138}Ba. The variations of compound nucleus formation probability P_{CN}, survival probability P_{surv}, and near constancy of ΔR-values, with compound nucleus excitation energy E^{*}_{CN}, are then employed to predict channel cross sections σ_{xn}, for decay of ^{220}Th* formed using ^{16}O + ^{204}Pb target-projectile combination. Finally, how DCM can be used to make predictions at energies where experimental data are not available is illustrated using ^{217}At* compound nucleus formed in ^{9}Li+^{208}Pb hot fusion reaction. Here empirical value of the parameter ΔR, at a fixed value of laboratory energy, E_{Lab} is obtained for an exact fit of the experimental (total) fusion cross section $\sigma_{fusion} = \sum_{x=1}^{6} \sigma_{xn}$ corresponding to decay of ^{217}At* formed via

^{9}Li + ^{208}Pb target-projectile combination. The *same* values for ΔR and laboratory energy are then used to predict the total fusion cross sections for ^{9}Li-induced reactions on ^{27}Al, ^{67}Cu, ^{70}Zn and ^{120}Sn targets and the results are compared with experimental data wherever available. The importance of such theoretical analysis pertains to the fact that a theory that judiciously incorporates adequate variables referred to as good "quantum numbers" or "degrees-of-freedom" is not only needed for a better understanding of the experimental data but the theoretical model itself should also be capable of making predictions, logical and sensible enough, for planning new experiments.

REFERENCES

Bao, X.J., S. Q. Guo, H. F. Zhang and J. Q. Li. 2016. Influence of hexadecapole deformation on production cross sections of superheavy nuclei. J. Phys. G: Nucl. Part. Phys. 43: 125105.

Blank, B., J.J. Gaimard, H. Geissel *et al*. 1993. Total and 2n-removal cross sections of the neutron-rich isotopes ^{8,9,11}Li. Nucl. Phys. A 555: 408.

Blocki, J. P., H. Feldmeier and W.J. Swiatecki. 1986. Dynamical hindrance to compound-nucleus formation in heavy-ion reactions. Nucl. Phys. A 459: 145.

Bjornholm, S. and W. J. Swiatecki. 1982. Dynamical Aspects of Nucleus-Nucleus Collisions. Nucl. Phys. A 391: 471.

Businaro, U. L. and S. Gallone. 1957. Asymmetric equilibrium shapes in the liquid drop model. Nuovo Cimento 5: 315.

Chopra, S. , A. Kaur and R. K. Gupta. 2015. Determination of the compound nucleus survival probability P_{surv} for various "hot" fusion reactions based on the dynamical cluster-decay model. Phys. Rev. C 91: 034613.

Chopra, S., Hemdeep, P. Kaushal and R. K. Gupta. 2018. Signatures of higher-multipole deformations and noncoplanarity as essential, additional degrees-of-freedom in heavy-ion reactions. Physical Review C 98: 041603(R).

Denisov, V. Yu. and W.Norenberg. 2002. Entrance channel potentials in the synthesis of the heaviest nuclei. Eur. Phys. J. A 15: 375.

Gupta, R. K. , W. Scheid and W. Greiner. 1975. Theory of Charge Dispersion in Nuclear Fission. Phys. Rev. Lett. 35: 353.

Gupta, R. K. , S. Kumar and W. Scheid. 1997. Structural Configurations in an Extended Orbiting Cluster Model for Molecular Resonance States. Int. J Mod. Phys. E 6: 259.

Gupta, R. K. and W. Greiner. 1999. Heavy Elements and Related New Phenomenon, edited by W. Greiner and R. K. Gupta, (World Scientific, Singapore) I: 397; ibid I: 536.

Gupta, R. K. , M. Balasubramaniam, C. Mazzocchi, M. La Commara and W. Scheid. 2002. Decay of excited ^{116}Ba* formed in the ^{58}Ni+^{58}Ni reaction via the emission of intermediate mass fragments. Phys. Rev. C 65: 024601.

Gupta, R. K., M. Balasubraniam, R. Kumar, D. Singh and C. Beck. 2004. Collective clusterization effects in light heavy ion reactions. Nucl. Phys. A 738: 479c.

Gupta, R. K. , N. Singh and M. Manhas. 2004. Generalized proximity potential for deformed, oriented nuclei. Phys. Rev. C 70: 034608.

Gupta, R. K., M. Balasubramaniam, R. Kumar, D. Singh, C. Beck and W. Greiner. 2005. Dynamical cluster-decay model for hot and rotating light-mass nuclear systems, applied to low-energy ^{32}S+^{24}Mg $\rightarrow$^{56}Ni$*$ reaction. Phys. Rev. C 71: 014601.

Gupta, R. K. , M. Balasubramaniam, R. Kumar, N. Singh, M. Manhas and W. Greiner. 2005. Optimum orientations of deformed nuclei for cold synthesis of superheavy elements and the role of higher multipole deformations. J. Phys. G: Nucl. Part. Phys. C 31: 631.

Gupta, R. K. , M. Manhas and W. Greiner. 2006. Compactness of the ^{48}Ca induced hot fusion reactions and the magnitudes of quadrupole and hexadecapole deformations. Phys. Rev. C 73: 054307.

Gupta, R. K., S. K. Arun, R. Kumar and Niyti. 2008. Int. Rev. Phys. (IREPHY) 2: 369.

Gupta, U., P. P. Singh, D. P. Singh, M. K. Sharma, A. Yadav, R. Kumar, B. P. Singh and R. Prasad.

2008. Observation of large incomplete fusion in $^{16}O+^{103}Rh$ system at ≈ 3-5 MeV/nucleon. Nucl. Phys. A 811: 77.

Hemdeep, S. Chopra, A. Kaur and R. K. Gupta. 2017. Formation and decay of the compound nucleus $^{220}Th^{*}$ within the dynamical cluster-decay model. Phys. Rev. C 95: 014609.

Hemdeep, S. Chopra, A. Kaur, P. Kaushal, and R. K. Gupta. 2018. Role of higher-multipole deformations and noncoplanarity in the decay of the compound nucleus $^{220}Th*$ within the dynamical cluster-decay model. Phys. Rev. C 97: 044623.

Hinde, D. J. and M. Dasgupta, *et al.* 1995. Fusion-Fission versus Quasifission: Effect of Nuclear Orientation. Phys. Rev. Lett. 74: 1295.

Hinde, D. J., M. Dasgupta, J. R. Leigh, J. C. Mein, C. R. Morton, J. O. Newton and H. Timmers. 1996. Conclusive evidence for the influence of nuclear orientation on quasifission. Phys. Rev. C 53: 1290.

Hinde, D. J. and A.C. Berriman, *et al*. 2002. Role of Entrance-channel Dynamics in Heavy Element Synthesis. J. Nucl. Radiochem. Sci. 3: 31.

Hinde, D. J., M. Dasgupta and A. Mukherjee. 2002. Severe Inhibition of Fusion by Quasifission in Reactions Forming ^{220}Th. Phys. Rev. Lett. 89: 282701.

Jensen, A. S. and J. Damgaard. 1973. Shell effects in a paired nucleus for finite excitation energies. Nucl. Phys. A 203: 578.

Kaur, A., S. Chopra and R. K. Gupta. 2014. Compound nucleus formation probability P_{CN} determined within the dynamical cluster-decay model for various "hot" fusion reactions. Phys. Rev. C 90: 024619.

Kaur, M., B. B. Singh, M. K. Sharma and R. K. Gupta. 2015. Decay analysis of compound nuclei with masses A ≈ 30– 200 formed in reactions involving loosely bound projectiles. Phys. Rev. C 92: 024623.

Kaur, A. , Hemdeep, P. Kaushal, B. R. Behera, R. K. Gupta. 2017. Dynamical Cluster-decay Model (DCM) applied to $^{9}Li+ ^{208}Pb$ reaction. Nuclear Physics A 966: 306-323.

Kaur, A., P. Kaushal, Hemdeep, R. K. Gupta. 2018. Decay analysis of compound nuclei formed in reactions with exotic neutron-rich ^{9}Li projectile and the synthesis of $^{217}At*$ within the dynamical cluster-decay model. Nuclear Physics A 969: 184-195.

Kaushal, P. and M. K. Sharma. 2019. Systematic decay analysis of $^{202}Po*$ compound nucleus using Dynamical Cluster-decay Model. Int. J. Mod. Phys. E 28: 1950105(1-25).

Kaushal, P. 2020. Analysis of the decay of the rare *p* nucleus $^{120}Te^{*}$ within a collective clusterization approach. Phys. Rev. C 101: 014615.

Kaushal, P. 2020. Analysis of $^{113}In(\alpha,n)^{116g/(or)m}Sb$ reaction at astrophysically interesting center-of-mass energies and synthesis of $^{117}Sb^{*}$ within the Dynamical Cluster-decay Model. Nucl. Phys. A 994: 121677.

Khosla, H. S. , S. S. Malik and R. K. Gupta. 1990. Two-centre shell model description of quasi-molecular resonance states in heavy-ion collisions. Nucl. Phys. A 513: 115.

Kim, K., Y. Kim, A. K. Nasirov, G. Mandaglio and G. Giardina. 2015. Effects of entrance channels on the evaporation residue yields in reactions leading to the ^{220}Th compound nucleus. Phys. Rev. C 91: 064608.

Kumar, S. and R.K. Gupta.1997. Neck formation and deformation effects in a preformed cluster model of exotic cluster decays. Phys. Rev. C 55: 218 .

LeCouteur, K. J. and D. W. Lang. 1959. Neutron evaporation and level densities in excited nuclei. Nucl. Phys. 13: 32.

Loveland, W., A.M. Vinodkumar, R.S. Naik *et al*. 2006. Subbarrier fusion of ^{9}Li with ^{70}Zn. Phys. Rev. C 74: 064609.

Malik, S. S. and R. K. Gupta. 1989. Theory of cluster radioactive decay and of cluster formation in nuclei. Phys. Rev. C 39: 1992.

Manhas, M. and R. K. Gupta. 2005. Proximity potential for deformed, oriented nuclei: "Gentle" fusion and "hugging" fusion. Phys. Rev. C 72: 024606.

Maruhn, J. and W. Greiner. 1974. Theory of Fission-Mass Distributions Demonstrated for ^{226}Ra,^{236}U,^{258}Fm. Phys. Rev. Lett. 32: 548.

Matsuse, T. , C. Beck, R. Nouicer and D. Mahboub. 1997. Extended Hauser-Feshbach Method for Statistical Binary-Decay of Light-Mass Systems. Phys. Rev. C 55: 1380.

Mayorov, D.A., T. A. Werke, M. C. Alfonso, M. E. Bennett and C. M. Folden III. 2014. Production cross sections of elements near the N=126 shell in ^{48}Ca-induced reactions with ^{154}Gd, ^{159}Tb, ^{162}Dy, and ^{165}Ho targets. Phy. Rev. C 90: 024602.

Meitner, L. 1950. Fission and nuclear shell model. Nature 165: 561.

Misicu, S. and W. Greiner. 2004. Influence of hexadecupole deformation and role of orientation in capture reactions with ^{48}Ca projectiles leading to superheavy nuclei. Phys. Rev. C 69: 054601.

Morton, C. R. , A. C. Berriman, R. D. Butt, M. Dasgupta, A. Godley, D. J. Hinde and J. O. Newton. 2000. Memory of the entrance-channel *K* distribution observed in fission at high angular momentum. Phys. Rev. C 62: 024607.

Navin, A., V. Tripathi, Y. Blumenfeld *et al*. 2004. Direct and compound reactions induced by unstable helium beams near the Coulomb barrier. Phys. Rev. C 70: 044601.

Niyti and R. K. Gupta. 2014. Synthesis of the doubly magic deformed nucleus $^{270}_{108}Hs_{162}$ in the decay of ^{274}Hs* formed via hot fusion reactions: Entrance-channel effects and role of magicity of ^{48}Ca and ^{270}Hs. Phys. Rev. C 89: 014603.

Okuducu, S. , S. Sönmezoğlu and E. Eser. 2006. Calculation of nuclear level density parameters of some deformed light nuclei using collective excitation modes. Phys. Rev. C 74: 034317.

Pant, L. M., A. Saxena, R. K. Choudhury and D. M. Nadkarni. 1996. Mass dependence of fragment anisotropy in the fission of ^{11}B+^{237}Np and ^{16}O+^{209}Bi systems. Phys. Rev. C 54: 4.

Rafiei, R., R. G. Thomas, D. J. Hinde, M. Dasgupta, C. R. Morton, L. R. Gasques, M. L. Brown and M. D. Rodriguez. 2008. Strong evidence for quasifission in asymmetric reactions forming ^{202}Po*. Phys. Rev. C 77: 024606.

Royer, G. and J. Mignen. 1992. Binary and ternary fission of hot and rotating nuclei. J. Phys. G: Nucl. Part. Phys. 18: 1781.

Sahm, C.C., H.G. Clerc, *et al*. 1985. Fusion probability of symmetric heavy, nuclear systems determined from evaporation-residue cross sections. Nucl. Phys. A 441: 316.

Sanders, S. J. 1991. Fusion-fission in nuclear systems with 40≤ACN≤80. Phys. Rev. C 44: 2676.

Sanders, S. J. , A. Szanto de Toledo and C. Beck. 1999. Binary Decay of Light Nuclear Systems. Phys. Rep. 311: 487.

Sandulescu, A., S. Misicu, F. Carstoiu, A. Florescu and W. Greiner.1997. Role of fragment higher static deformations in the cold binary fission of ^{252}Cf. Phys. Rev. C 57: 2321.

Satou, K., H. Ikezoe, S. Mitsuoka, K. Nishio and S. C. Jeong. 2002. Effect of shell structure in the fusion reactions ^{82}Se+^{134}Ba and ^{82}Se+^{138}Ba. Phys. Rev. C 65: 054602.

Sawhney, G. , M. K. Sharma and R. K. Gupta. 2011. Role of higher-multipole deformations in exotic ^{14}C cluster radioactivity. Phys. Rev. C 83: 064610.

Sharma, M. K. , G. Sawhney, R. K. Gupta and W. Greiner. 2011.The decay of the compound nucleus ^{215}Fr* formed in the ^{11}B+^{204}Pb and ^{18}O+^{197}Au reaction channels using the dynamical cluster-decay model. J. Phys. G: Nucl. Part. Phys. 38: 105101.

Shroy, R.E., A.K. Gaigalas, G. Schatz and D.B. Fossan. 1979. High spin states in odd-mass 113-119Sb: ΔJ bands on $\frac{9}{2^+}$ proton-hole states. Phys. Rev. C 19: 1324.

Singh, B. B. , M. K. Sharma, and R. K. Gupta. 2008. Decay of ^{246}Bk$*$ formed in similar entrance channel reactions of ^{11}B+^{235}U and ^{14}N+^{232}Th at low energies using the dynamical cluster-decay model. Phys. Rev. C 77: 054613.

Swiatecki, W. J. 1981. The dynamics of nuclear coalescence or reseparation. Phys. Scr. 24: 113.

Vermeulen, D., H.G. Clerc, C.C. Sahm, *et al.* 1984. Cross sections for evaporation residue production near the *N*=126 shell closure. Z Physik A 318: 157.

Vinodkumar, A.M., W. Loveland, P.H. Sprunger, *et al*. 2009. Fusion of ^{9}Li with ^{208}Pb. Phys. Rev. C 80: 054609.

Yalçin, C., *et al*. 2009. Odd p isotope ^{113}In: Measurement of α-induced reactions. Phys. Rev. C 79: 065801.

LATTICE DEFECT AND FERROMAGNETISM IN ZnO WITH TRANSITION METAL AND Ce IONS PREPARED BY CHEMICAL ROUTES

***K.C. Verma[1] and Navdeep Goyal[2]**

[1]*Materials Science & Sensor Applications (MSSA),*
CSIR-Central Scientific Instruments Organisation, Chandigarh 160030, India
[2]*Department of Physics, Panjab University, Chandigarh 160014, India*

ABSTRACT

Spintronic is an emerging field which has essential to develop semiconductors with ferromagnetically polarized carriers at room temperature. For such case, the spin as well as charge of carriers can be coupled with an external magnetic field to control devices. Therefore, we have reported a short review study from our previous experimental results on room temperature ferromagnetism in diluted magnetic semiconductors of ZnO with doping of transition metal ions, TM = Fe, Co, Cu, Ni. Co-doping effect of Ce ions into TM:ZnO is also given. Doping with TM and rare earth ions changes the properties of ZnO nanoparticles by introducing intrinsic donor defects. The mediation for ferromagnetic interactions in TM:ZnO might be included defect states (vacancies of Zn and oxygen) present in the samples. So, we report here defects formation in wurtzite lattice of ZnO due to changes in lattice constants (*a* & *c*) values with TM doping and also the oxygen vacancies evaluated on the nanostructural surfaces. We also summarized some chemical routes on the basis of their simplicity, time consuming and nanostructural growth in the form of shape/size of the ZnO based nanomaterials. X-ray diffraction patterns indicate that the dopant of Ni, Cu and Ce ions into ZnO found wurtzite type hexagonal phase and these dopants highly influenced the lattice constants as defect formation. Room temperature ferromagnetism is described due to bound magnetic polarons formation with Ni^{2+}, Cu^{2+}, Ce^{3+} ions into ZnO via oxygen vacancies. Zero field and field cooling SQUID measurement confirm the strength of antiferromagnetism in ZnO. Weak ferromagnetism at room temperature is observed in Ce co-doped Fe,Co:ZnO nanoparticles due to strong antiferromagnetic strength which observed sufficiently at low temperature. Higher value of saturation magnetization is observed in 3 mol% Fe and Co doping into ZnO which is enhanced with Ce co-doping. Thin film of pure ZnO with small size nanograins (average size 9 nm) shown room temperature ferromagnetism (M_s = 0.07 emu cm^{-3}).

Keywords: DMS ZnO; ferromagnetism; oxygen vacancies; chemical synthesis.

INTRODUCTION

Recent advances in ZnO-based diluted magnetic semiconductors (DMSs) are suitable in electronic control of their spin properties [Dietl *et al.* 2000; Verma *et al.* 2016]. During the past decades, the ferromagnetism for DMS ZnO has been predicted with doping of various transition metal (TM = Cr, Mn, Fe, Co, Ni, Cu) ions [Radovanovic *et al.* 2003]. Magnetic ordering in ZnO-based DMS appears to be sensitive with chemical ordering of the TM dopants and defects (vacancies and interstitials) [Sluiter *et al.* 2005]. Spintronic applications require that ferromagnetism has an intrinsic origin, *i.e.* not with magnetic TM atom clusters or impurity phases. Magnetic couplings and the energetics of chemical ordering of ZnO with 5% substitution of Ti, V, Cr, Mn, Fe, Co, Ni for Zn have been calculated by density functional theory (DFT) [Sluiter *et al.* 2005]. In ZnO, the isolated TM atoms thus have levels *e*-spin-down, t_2-spin-down, *e*-spin-up, and t_2-spin-up from low to high energy states. The hybridization for antiferromagnetic is most significant for half *d*-band filling due to superexchange process. As ferromagnetic ZnO:TM remains contested as the common native defects in the form of O vacancies, Zn interstitials, and Zn vacancies may assume to be responsible into the magnetic exchanges. DFT calculations with oxygen vacancies for Co, Mn revealed

Corresponding author: dkuldeep.physics@gmail.com; kcv0309@gmail.com
Received: October 03, 2022, Accepted: December 15, 2022

little effect on magnetic couplings because induced donor state is too deep pointedly affect the occupancy of the extended TM levels. In contrast, both Zn interstitials and Zn vacancies change the occupancy of extended TM levels. Both electron doping with Zn interstitials and hole doping with Zn vacancies make Co, Mn substituted ZnO to be strongly ferromagnetic [Sluiter *et al.* 2005]. Iqbal *et al.* 2009 shown room temperature ferromagnetism for Ni:ZnO which is interpreted by overlapping of polarons mediated through O vacancy. It is based on bound magnetic polaron (BMP) model. Chakraborti *et al.* 2007 investigated Cu doped ZnO. It is suggested that Cu is a potential magnetic ion which has ½ spin in the +2 state and neither metallic Cu or Cu_2O or CuO is ferromagnetic. However, Wan *et al.* 2013 shown room temperature ferromagnetism due to indirect double-exchange mechanism associated with dual donor, Zn_i and O vacancies, and variable-valance Cu ions. Recently, we have reported room temperature ferromagnetism in Co and Fe doped ZnO that enhances with more dopant ions [Kaur *et al.* 2014]. In TM:ZnO, the co-doping of rare earth ions is temporarily generates charge carriers in the lattice [Liu *et al.* 2014].

DMS materials are formed with TM ions doping, such as Mn and Cr, or rare earth ions into the host semiconductor [Pearton *et al.* 2007]. Both types of ions have partially filled *d* and *f* shells, respectively, which give rise to unpaired electrons. Magnetic behavior of such DMS materials depends upon the concentration of the TM ions, the carrier density, and the crystal quality. When 3d TM ions are substituted for the cations of the host ZnO, their electronic structure is influenced with strong 3d orbitals of the magnetic ion and the p orbitals of the neighboring anions. It involved the delocalized conduction band electrons and valence band holes. This TM doped ZnO also has a random diluted system of the localized magnetic moments associated with the magnetic atoms. Rare earth atoms have partially filled *f*-orbitals that carry high magnetic moments which originate on a single ion to participate into resulting magnetic coupling with TM ions via partially filled d-orbitals [Verma *et al.* 2016].

Electronic structure of 3 mol% Ce for Zn into $Zn_{0.97}Fe_{0.03}O$ and $Zn_{0.97}Co_{0.03}O$ DMS was studied by DFT calculations [Babu *et al.* 2014]. The ΔE, difference in binding energy enhancement of the relaxor wurtzite ZnO structure indicates that the Ce atom is more stable when replaced by those Zn atoms which is nearest neighbour to TM: Fe or Co ions with host Zn. Also, the doping of Ce ions into Fe:ZnO and Co:ZnO results into variations in bond length among Zn, O, Fe, Co and Ce atoms, which result to induce lattice defects (vacancies) in the wurtzite hexagonal structure [Verma *et al.* 2016]. Among rare earths, Ce has potential interest due to its features to form Ce oxide (CeO_2 and Ce_2O_3) to participate the redox coupling Ce^{3+}/Ce^{4+} with oxygen [Babu *et al.* 2014]. This ionic transformation of Ce ions in oxygen vacancies within Ni and Cu doped ZnO might to enhance ferromagnetic ordering.

In this paper, we have given some experimental results of $Zn_{0.95}Ni_{0.05}O$ (ZNiO), $Zn_{0.91}Ni_{0.05}Ce_{0.04}O$ (ZNiO:Ce), $Zn_{0.95}Cu_{0.05}O$ (ZCuO) and $Zn_{0.91}Cu_{0.05}Ce_{0.04}O$ (ZCuO:Ce) nanoparticles and also review our previous results on TM ions and Ce substituted ZnO nanomaterials.

Table 1: Synthesis methods used for fabricating diluted magnetic semiconductor of ZnO.

Chemical composition	**Synthesis method; Final product**	**Reaction time; Precursor salts**	**Brief synthesis procedure & heating conditions of processing**
$Zn_{0.94}TM_{0.03}Ce_{0.03}O$ [Verma *et al.* 2016]	Sol-gel based chemical process using PVA; Nanoparticles	Hours; Zn acetate, ferric chloride, Co chloride, Ce chloride	In this method, ethanol and acetic acid mixed in the ratio of 3:1. Zn acetate was added to it and stirred for 2 hrs. Dopants Fe, Co, Ce added in each sample in the desired stoichiometric ratio and again stirred for 1 h. Precursor solution (M) in each sample was mixed with PVA solution, *i.e.* M : PVA = 5 : 2. Solution was dried at 250 ^oC and annealed at 700 ^oC/2 h to get crystallization.
$Zn_{1-x}Co_xO$ [Ram *et al.* 2014]	Metallo-organic decomposition; Thin films	Days; $(C_7H_{15}COO)_2Zn$, $(C_7H_{15}COO)_2Co$, xylene	Film-coating solution was prepared from Zn and Co hexanoate in xylene. Solution was refluxed at 60°C with constant stirring for 2 hrs. to get homogeneous mixing. Poly ethylene glycol added dropwise to the coating solution as binder. Film was deposited on Si substrate by spin-coating technique with 4300 rpm/60 s and subjected to drying at 400°C/5 min. For crystallization, the films were annealed at 600°C for 3 hrs.

which the strong inter-atomic direct 5*d*-3*d* exchange is transmitted to 4*f* electrons via intra-atomic 4*f*-5*d* ferromagnetic exchange. The 5*d*-3*d* exchange is antiferromagnetic when 5*d* band is less than half full and the 3*d* band is more than half full. This is the case for RE metals with ferromagnetic 3d TM. TM spin couples antiparallel with RE ions spin and the resulting magnetization of sublattices couple parallel as described; J = L–S process. Therefore, the transition of $Ce^{3+} - V_{\ddot{O}}$ with TM ions is expected to be antiferromagnetic. In the report given by Verma *et al.* 2016 has found ZFC and FC at H = 500 Oe and T = 300-5 K for Ce substituted ZFO and ZCO indicates antiferromagnetic transitions converted into ferromagnetic states at low temperature via vacancies. Coey *et al.* 2005 reported that an electron trapped within defects/oxygen vacancies creates an F-centre. Exchange interactions between neighboring magnetic ions mediated by F-centre has BMP formation. Overlapping of such polarons contributes long-range ferromagnetic ordering in Ce substituted Fe,Co: ZnO nanoparticles.

Lattice defects and magnetism in Co and Fe doped ZnO

The synthesis method, morphology, lattice constant (*a* & *c*) and magnetization of $Zn_{1-x}Co_xO$ (ZC) [x = 0 (Z0), 0.01 (ZC1), 0.03 (ZC3) and 0.05 (ZC5)] and $Zn_{1-x}Fe_xO$ (ZF) [x = 0.01 (ZF1), 0.03 (ZF3) and 0.05 (ZF5)] nanorods are given in Table 2 [Kaur *et al.* 2014]. The ZC and ZF nanorods prepared by a sol-gel process. XRD pattern revealed the hexagonal wurtzite phase. TEM images show the average diameter 9-13, 66-73, 57-65, 43-47, 43-51, 12-15 and 11-13 nm, length 21-25, 197-207, 129-135, 115-120, 110-119, 49-53 and 27-32 nm, and *c*/*a* ratio are 1.5984, 1.5977, 1.5988, 1.6007, 1.5973, 1.5987 and 1.6001, respectively for Z0, ZC1, ZC3, ZC5, ZF1, ZF3 and ZF5 sample. From Table 2, the variation in lattice constant *a* & *c* with Co and Fe doping for ZnO indicates defect vacancies formation. Since the ionic radii of Co^{2+} (0.58 Å) and Fe^{3+} (0.49 Å) ions are smaller than Zn^{2+} (0.60 Å) in tetrahedral environment with high spin results into gradual decrease in lattice parameters and size in Co, Fe doped (from 1 to 5 mol%) ZnO nanorods. Remarkably, the rapid increase in size of nanorods for ZC1 and ZF1 sample may occur due to octahedral environment of Co^{2+} and Fe^{3+} ions in the wurtzite lattice. Because the octahedral Co^{2+} has ionic radius between 0.65 Å (low spin) and 0.74 Å (high spin) and Fe^{3+} has a ionic radius between 0.55 Å (low spin) and 0.64 Å (high spin) exists. Also from Table 2, the pure ZnO show perfect diamagnetism. The Co and Fe doped has super-ferromagnetic type magnetic behavior at room temperature. Values of M_s are 0.344, 0.483, 0.354, 0.233, 0.459 and 0.328 emu g^{-1}, respectively, measured for ZC1, ZC3, ZC5, ZF1, ZF3 and ZF5 nanorods.

Variations in M_s values are explained due to nanostructural shape/size effect and the stoichiometric ratio or concentration of dopant ions and the resulting lattice parameters. Moreover, the F-center exchange mechanism also employ to illustrate the room temperature ferromagnetism of Fe-doped ZnO. For this, $Fe^{3+} - V_O^{2-} - Fe^{3+}$ exchange magnetic interaction occurs from which the electron trapped in oxygen vacancy to form F-center. Interactions among ferromagnetic and antiferromagnetic components responsible into observed variations in magnetization. Bound magnetic polarons formation also responsible due to alignment in spins of transition metal ions and the localized holes of the polarons act on the transition-metal impurities surrounding them. It produces an effective magnetic field and aligning all spins.

Ferromagnetic responses in $Zn_{1-x}Co_xO$ thin films

$Zn_{1-x}Co_xO$ (ZC) [x = 0 (ZC0), 0.01 (ZC1), 0.03 (ZC3), 0.05 (ZC5), 0.07 (ZC7) and 0.09 (ZC9)] thin films were prepared by metallo-organic decomposition (MOD) method by Ram *et al.* 2014 and deposited on Si substrate with spin-coating (annealed at 600^{o}C/3 hrs). Values of lattice distortion, *c*/*a* ratio are 1.599, 1.597, 1.596, 1.594, 1.593 and 1.592, and the average grain size (from XRD FWHM) are 39 nm, 24 nm, 19 nm, 15 nm, 11 nm and 7 nm, and saturation magnetization, M_s = diamagnetic, 1.24, 2.16, 3.02, 4.07 and 3.94 emu cm^{-3}, respectively, for Z0, ZC1, ZC3, ZC5, ZC7 and ZC9 thin films [Table 2]. From these results, the observed magnetic behavior in Co:ZnO thin films attributed due to defects like oxygen vacancies explained on the basis of BMP model by Bednarski *et al.* 2012. According to this BMP model, bound electrons in defects, like oxygen vacancies, can couple Co ions causes ferromagnetic regions to overlap results into long-range ferromagnetic order. Magnetization is assumed to be originate from correlated regions and isolated spins. Magnetization that arises from the correlated spins is ferromagnetic. However, the

magnetization due to uncorrelated spins is paramagnetic. Therefore, there is a greater possibility for occurrence of antiferromagnetic spins.

Magnetic ordering in ZnO nanoparticles due to low Co concentration

Values of lattice constant and ferromagnetism of $Zn_{1-x}Co_xO$ [x = 0.002 (ZCO02), 0.004 (ZCO04), 0.006 (ZCO06) and 0.008 (ZCO08)] nanoparticles prepared by sol-gel chemical process are given in Table 2. From Table 2, the distortion ratio, c/a for Co doped ZnO samples is slightly higher with pure ZnO ($c/a \sim 1.598$). This may due to octahedral environment of Co ions at their low concentration with host ZnO. Octahedral Co^{2+} has an ionic radius between 0.65 Å (low spin) and 0.745 Å (higher spin) which is higher than host Zn^{2+} (0.60 Å). These low Co concentrated ZnO nanorods have average diameter, D ~ 18, 23, 41 and 53 nm, and length, l ~ 39, 57, 95 and 127 nm, respectively, measured for ZCO02, ZCO04, ZCO06 and ZCO08 sample. In pure ZnO, the value of D ~ 10 nm and l ~ 23 nm [Kaur *et al.* 2014]. Effect of Co concentrations to induce lattice oxygen vacancies is evaluated from variations in observed Raman active modes. PL spectra included defects oxygen vacancies which is more favourable for Zn in Co:ZnO samples. XPS spectra indicate +2 oxidation states of Zn and three different defects related oxidation states of O ions. However, the Co 2p has mixed Co^{3+} and Co^{2+} (octahedral and tetrahedral) oxidation state detected. From table 2, the value of saturation magnetization, M_s ~0.0046, 0.0062, 0.0126 and 0.1021 emu g^{-1}, respectively, measured for ZCO02, ZCO04, ZCO06 and ZCO08. This observed magnetic behavior is highly influenced because of nanostructural growth of ZnO at low Co concentrated ions. This is because higher surface to volume ratio contributes large amount of surface oxygen vacancies. Venkatesh *et al.* 2012 suggested point defects in the form of intrinsic defects and surface related impurity transitions that enhanced in anisotropic ZnO nanoparticles.

Ferromagnetism in undoped ZnO thin film

In Table 2, the undoped ZnO has room temperature ferromagnetic behavior (M_s = 0.07 emu cm^{-3}; H_c = 210 Oe) [Verma *et al.* 2019]. This ZnO thin films was synthesized by a metallo-organic decomposition method and annealed at 500°C/7 hrs. Average particles size is 9 nm. Value of a = 0.3246 nm, c = 0.5158 nm and distortion, c/a = 1.5890. It was reported earlier that the diamagnetism is dominant in pure ZnO with average particle size ≥40 nm, irrespective ZnO sample being prepared by a similar MOD method [Ram *et al.* 2014]. This is because, here, the average grain size of pure ZnO reduced to 9 nm and observed room temperature ferromagnetism. Nanostructural grain boundaries might be induced surface states (defects/vacancies) influence magnetic ordering of ZnO. Areas of nanostructural grain boundaries with grain volumes reaches some threshold value and the resulting vacancies participate into room temperature ferromagnetism. These nanograin boundaries thoroughly created oxygen vacancies.

Table 2: Lattice defects (vacancies) due to doping effect and nanostructural growth in TM and Ce substituted ZnO (given synthesis method, morphology [particles size (X), nanorods (diameter (D), length (l))], lattice constant (a & c), lattice distortion (c/a), saturation magnetization (M_s) and magnetic coercive field (H_c).

Samples	**Synthesis method**	**Morphology; size (X, D, l in nm)**	***a*(nm)**	***c*(nm)**	***c*/*a***	**M_s in emu g^{-1} (emu cm^{-3} for thin film)**	**H_c (in Oe)**
ZnO [Kaur *et al.* 2014]	Sol-gel using PVA	Nanorods; D= 10, l = 23	0.3255	0.5203	1.5985	Diamagnetic	132
$Zn_{0.99}Co_{0.01}O$ [Kaur *et al.* 2014]	Sol-gel using PVA	Nanorods; D= 70, l = 200	0.3259	0.5207	1.5977	0.344	13
$Zn_{0.97}Co_{0.03}O$ [Kaur *et al.* 2014]	Sol-gel using PVA	Nanorods; D= 63, l = 131	0.3256	0.5206	1.5989	0.483	41
$Zn_{0.95}Co_{0.05}O$ [Kaur *et al.* 2014]	Sol-gel using PVA	Nanorods; D= 46, l = 117	0.3251	0.5204	1.6007	0.354	40
$Zn_{0.99}Fe_{0.01}O$ [Kaur *et al.* 2014]	Sol-gel using PVA	Nanorods; D= 48, l = 113	0.3261	0.5209	1.5974	0.233	88
$Zn_{0.97}Fe_{0.03}O$ [Kaur *et al.* 2014]	Sol-gel using PVA	Nanorods; D= 14, l = 50	0.3257	0.5207	1.5987	0.459	35

$Zn_{0.95}Fe_{0.05}O$ [Kaur *et al.* 2014]	Sol-gel using PVA	Nanorods; D= 12, *l* = 30	0.3253	0.5205	1.6001	0.328	12
ZnO [Ram *et al.* 2014] High annealing temperature	Metallo-Organic Decomposition	Thin film; *X* = 39	0.3251	0.5201	1.5998	Diamagnetic	188
$Zn_{0.97}Co_{0.03}O$ [Ram *et al.* 2014]	Metallo-Organic Decomposition	Thin film; *X* = 19	0.3245	0.5181	1.5966	2.16	201
$Zn_{0.95}Co_{0.05}O$ [Ram *et al.* 2014]	Metallo-Organic Decomposition	Thin film; *X* = 15	0.3241	0.5168	1.5945	3.02	83
$Zn_{0.93}Co_{0.07}O$ [Ram *et al.* 2014]	Metallo-Organic Decomposition	Thin film; *X* = 11	0.3235	0.5154	1.5932	4.07	97
$Zn_{0.91}Co_{0.09}O$ [Ram *et al.* 2014]	Metallo-Organic Decomposition	Thin film; *X* = 7	0.3232	0.5148	1.5928	3.94	53
$Zn_{0.94}Fe_{0.03}Ce_{0.03}O$ [Verma *et al.* 2016]	Sol-gel using PVA	Nanoparticles; *X* = 97	0.3260	0.5214	1.5994	0.339	753
$Zn_{0.94}Co_{0.03}Ce_{0.03}O$ [Verma *et al.* 2016]	Sol-gel using PVA	Nanoparticles; *X* = 106	0.3261	0.5217	1.5998	0.478	197
$Zn_{0.998}Co_{0.002}O$ [Verma *et al.* 2016]	Sol-gel using PVA	Nanorods; D= 18, *l* = 39	0.32562	0.52056	1.5986	0.0046	28
$Zn_{0.996}Co_{0.004}O$ [Verma *et al.* 2016]	Sol-gel using PVA	Nanorods; D= 23, *l* = 57	0.32561	0.52058	1.5987	0.0062	93
$Zn_{0.994}Co_{0.006}O$ [Verma *et al.* 2016]	Sol-gel using PVA	Nanorods; D= 41, *l* = 95	0.32557	0.52059	1.5990	0.0126	113
$Zn_{0.992}Co_{0.008}O$ [Verma *et al.* 2016]	Sol-gel using PVA	Nanorods; D= 53, *l* = 127	0.32559	0.52068	1.5991	0.1021	162
$Zn_{0.95}Ni_{0.05}O$ [Verma *et al.* 2017]	Sol-gel using PVA	Nanoparticles; *X* = 27	0.3245	0.5201	1.6028	0.073	150
$Zn_{0.91}Ni_{0.05}Ce_{0.04}O$ [Verma *et al.* 2017]	Sol-gel using PVA	Nanoparticles; *X* = 81	0.3244	0.5211	1.6063	0.085	558
$Zn_{0.95}Cu_{0.05}O$ [Verma *et al.* 2017]	Sol-gel using PVA	Nanoparticles; *X* = 57	0.3242	0.5202	1.6045	0.053	393
$Zn_{0.91}Cu_{0.05}Ce_{0.04}O$ [Verma *et al.* 2017]	Sol-gel using PVA	Nanoparticles; *X* = 159	0.3243	0.5213	1.6074	0.132	68
ZnO [Verma *et al.* 2019] Low annealing temperature	Metallo-Organic Decomposition	Thin film; *X*= 9	0.3246	0.5158	1.5890	0.07	210

CONCLUSION

Ferromagnetism of DMS ZnO nanoparticles is described due to formation of defect/vacancies mediated via F-centre exchange antiferromagnetic interaction to form BMPs. TM ions in ZnO are intrinsically antiferromagnetic because of their substitution at Zn sites does not introduce any extra carriers. Interaction among localized spins on TM ions and delocalized carrier electrons originating from the O vacancies is responsible into room temperature ferromagnetism. Doping of RE ions with intrinsic strong magnetic anisotropy might to tailored the coupling between dopant ions and defects stabilized ferromagnetic ordering in DMS ZnO. We have found that the smaller sized nanorods of Co and Fe doped ZnO exhibits comparatively higher saturation magnetization. The 5mol% Co doping into ZnO has shown comparatively higher room temperature ferromagnetism (M_s~3.02 emu cm^{-3}) in ZnO thin films (prepared by MOD method). For ZFCeO, the weak room temperature ferromagnetism was formed due to mixed valance states for Fe^{2+}/Fe^{3+} and oxidizing Ce^{3+} to Ce^{4+} via oxygen vacancies. Values of M_s at 300 K is 0.073, 0.085, 0.053 and 0.132 emu g^{-1}, respectively, measured for ZNiO, ZNiO:Ce, ZCuO and ZCuO:Ce nanoparticles.

ACKNOWLEDGMENTS

Author K.C. Verma was Ex. SRA in CSIR-CSIO Chandigarh and thankfully acknowledges the financial support given by CSIR-HRDG for SRA (Pool Scientist) fellowship scheme under Grant No. B-12287 [SRA (Pool No): 9048-A].

REFERENCES

Babu, G.A., G. Ravi, T. Mahalingam, M. Navaneethan, M. Arivanandhan, Y. Hayakawa. Size and Surface Effects of Ce-Doped NiO and Co_3O_4 Nanostructures on Ferromagnetism Behavior Prepared by the Microwave Route. *J. Phys. Chem. C* **2014**, *118*, 23335-23348.

Bednarski, H. and J. Spalek. Bound-magnetic-polaron molecule in diluted magnetic semiconductors. *J. Phys.: Condens. Matter* **2012**, *24*, 235801-13.

Castro, T.J., P.A.M. Rodrigues, A.C. Oliveira, F. Nakagomi, J. Mantilla, J.A.H. Coaquira, A.F. Junior, H.V.S. Pessoni, P.C. Morais, S.W. da Silva. Optical and magnetic properties of Co-doped ZnO nanoparticles and the onset of ferromagnetic order. *J. Appl. Phys.* **2017**, *121*, 013904-10.

Chakraborti, D.; J. Narayan, J.T. Prater. Room temperature ferromagnetism in $Zn_{1-x}Cu_xO$ thin films. *Appl. Phys. Lett.* **2007**, *90*, 062504-3.

Chen, Z.Y.; Y. Chen, Q.K. Zhang, N. Qi, Z.Q. Chen, S.J. Wang, P.H. Li, P. Mascher. Defect evolution and its impact on the ferromagnetism of Cu-doped ZnO nanocrystals upon thermal treatment: A positron annihilation study. *J. Appl. Phys.* **2017**, *121*, 025703-9.

Coey, J. M. D.; M. Venkatesan, C.B. Fitzgerald. Donor impurity band exchange in dilute ferromagnetic oxides. *Nat. Mater.* **2005**, *4*, 173-179.

Cullity, B. D., "X-Ray Diffraction" Addison-Wesley, Reading, MA, 1967.

Denardin, J.C.; A.L. Brandl, M. Knobel, P. Panissod, A.B. Pakhomov, H. Liu and X.X. Zhang. Thermoremanence and zero-field-cooled/field-cooled magnetization study of $Co_x(SiO_2)_{1-x}$ granular films. *Phys. Rev. B* **2002**, *65*, 064422-8.

Dietl, T., H. Ohno, F. Matsukura, J. Cibert, D. Ferr. Zener Model Description of Ferromagnetism in Zinc-Blende Magnetic Semiconductors. *Science* **2000**, *287*, 1019-1022.

Garcia, M.A. and M.L. Ruiz-Gonzalez. Interface Double-Exchange Ferromagnetism in the Mn-Zn-O System: New Class of Biphase Magnetism. *Phys. Rev. Lett.* **2005**, *94*, 217206-4.

Iqbal, J., B. Wang, X. Liu, D. Yu, B. He and R. Yu. Oxygen-vacancy-induced green emission and room-temperature ferromagnetism in Ni-doped ZnO nanorods. *New J. Phys.* **2009**, *11*, 063009-13.

Kaur, J., R.K. Kotnala, V. Gupta, K.C. Verma. Anionic polymerization in Co and Fe doped ZnO: Nanorods, magnetism and photoactivity. *Curr. Appl. Phys.* **2014**, *14*, 749-756.

Li, H., Y. Huang, Q. Zhang, Y. Qiao, Y. Gu, J. Liu, Y. Zhang. Facile synthesis of highly uniform Mn/Co-co-doped ZnO nanowires: Optical, electrical, and magnetic properties. *Nanoscale* **2011**, *3*, 654-660.

Liu, H., J. Yang, Z. Hua, Y. Liu, L. Yang, Y. Zhang, J. Cao. Cu-doping effect on structure and magnetic properties of Fe-doped ZnO powders. *Mater. Chem. Phys.* **2011**, *125*, 656-659.

Liu, X., Y. Zuo, L. Li, X. Huang and G. Li. Heterosturcture $NiO/Ce_{1-x}Ni_xO_2$: synthesis and synergistic effect of simultaneous surface modification and internal doping for superior catalytic performance. *RSC Adv.* **2014**, *4*, 6397-6406.

Midya, N., S.K. Neogi, Md.A. Ahmed, A. Banerjee, P. Kumar, D. Kanjilal and S. Bandyopadhyay. Correlation between magnetic and micro-structural properties of low energy ion irradiated and un-irradiated $Zn_{0.95}Mn_{0.05}O$ films. *RSC Adv.* **2017**, *7*, 771-781.

Pearton, S.J., D.P. Norton, M.P. Ivill, A.F. Hebard, J.M. Zavada, W.M. Chen and I.A. Buyanova. ZnO Doped With Transition Metal Ions. *IEEE Trans. Eelect. Dev.* **2007**, *54(5)*, 1040-1047.

Radovanovic, P.V. and D.R. Gamelin. High-Temperature Ferromagnetism in Ni^{2+}-Doped ZnO Aggregates Prepared from Colloidal Diluted Magnetic Semiconductor Quantum Dots. *Phys. Rev. Lett.* **2003**, *91*, 157202-4.

Ram, M., K.C. Verma and N.S. Negi. Room temperature ferromagnetism and photoluminescence of nanocrystalline $Zn_{1-x}Co_xO$ thin films prepared by sol-gel MOD. *Phil. Mag. Lett.* **2014**, 94(7): 404-414.

Rouchdi, M., E. Salmani, B. Fares, N. Hassanain and A. Mzerd. Synthesis and characteristics of Mg doped ZnO thin films: Experimental and ab-initio study. *Res. Phys.* **2017**, *7*, 620-627.

Singh, S., M. Singh, R.K. Kotnala, K.C. Verma. Hydrothermal synthesis of $NiFe_2O_4$, $Ni_{0.6}Zn_{0.4}Fe_2O_4$ and $Ni_{0.6}Zn_{0.4}Fe_2O_4/SrFe_2O_4$: nanostructure, magnetic and dielectric properties. *Ind. J. Pure Appl. Phys.* **2014**, *52*, 550-555.

Singhal, A., S.N. Achary, J. Manjanna, S. Chatterjee, P. Ayyub and A.K. Tyagi. Chemical Synthesis and Structural and Magnetic Properties of Dispersible Cobalt- and Nickel-Doped ZnO Nanocrystals. *J. Phys. Chem. C* **2010**, *114*, 3422-3430.

Sluiter, M.H. F., Y. Kawazoe, P. Sharma, A. Inoue, A. R. Raju, C. Rout, U.V. Waghmare. First Principles Based Design and Experimental Evidence for a ZnO-Based Ferromagnet at Room Temperature. *Phys. Rev. Lett.* **2005**, *94*, 187204-4.

Verma, K.C. and R.K. Kotnala. Defects-assisted ferromagnetism due to bound magnetic polarons in Ce into Fe, Co: ZnO nanoparticles and first-principle calculations. *Phys. Chem. Chem. Phys.* **2016**, *18*, 5647-5657.

Verma, K.C. and R. K. Kotnala. Realizing ferromagnetic ordering in SnO_2 and ZnO nanostructures with Fe, Co, Ce ions. *Phys. Chem. Chem. Phys.* **2016**, *18*, 17565-17574.

Verma, K.C. and R.K. Kotnala. Defects due to lattice distortion and nano-size intermediate ferromagnetism in La, Gd substituted $Zn_{0.95}Co_{0.05}O$. *Curr. Appl. Phys.* **2016**, *16*, 175-182.

Verma, K.C.; R. Bhatia, S. Kumar and R. K. Kotnala. Vacancies driven magnetic ordering in ZnO nanoparticles due to low concentrated Co ions. *Mater. Res. Express* **2016**, *3*, 076103-12.

Verma, K.C. and R.K. Kotnala. Understanding lattice defects to influence ferromagnetic order of ZnO nanoparticles by Ni, Cu, Ce ions. *J. Solid State Chem.* **2017**, *246*, 150-159.

Verma, K.C., N. Goyal and R.K. Kotnala. Lattice defect-formulated ferromagnetism and UV photo-response in pure and Nd, Sm substituted ZnO thin films. *Phys. Chem. Chem. Phys.* **2019**, *21*, 12540-12554.

Venkatesh, P.S., V. Purushothaman, S.E. Muthu. S. Arumugam, V. Ramakrishnan, K. Jeganathan, K. Ramamurthi. *CrystEngComm* **2012**, *14*, 4713.

Wang, D., Q. Chen, G. Xing, J. Yi, S.R. Bakaul, J. Ding, J. Wang, T. Wu. Robust Room-Temperature Ferromagnetism with Giant Anisotropy in Nd-Doped ZnO Nanowire Arrays. *Nano Lett.* **2012**, *12*: 3994-4000.

Wan, W., J. Huang, L. Zhu, L. Hu, Z. Wen, L. Sun, Z. Ye. Defects induced ferromagnetism in ZnO nanowire arrays doped with copper. *CrystEngComm* **2013**, *15*, 7887-7894.

Yang, C.Y., Y.H. Lu, W.H. Lin, M.H. Lee, Y.J. Hsu, Y.C. Tseng. Structural imperfections and attendant localized/itinerant ferromagnetism in ZnO nanoparticles. *J. Phys. D: Appl. Phys.* **2014**, *47*, 345003-7.

Yildirimcan, S., K. Ocakoglu, S. Erat, F.M. Emen, S. Reppe, E. Erdem. The effect of growing time and Mn concentration on the defect structure of ZnO nanocrystals: X-ray diffraction, infrared and EPR spectroscopy. *RSC Adv.* **2016**, *6*, 39511 -39521.

formation of an inclusion complex between the β-cyclodextrin unit of a catalytic system and substrate leads to increase in the concentration of substrate near the catalytically active centre. This leads to an increase in the reaction rate, higher substrate selectivity, enantio-selectivity and regio-selectivity. In past years, L-proline and D-glucosamine derivatives have been immobilized on β-cyclodextrin and applied in catalytic field (Abello, *et al.*, 2007).

APPLICATIONS OF INCLUSION COMPLEXES (ICs) IN ASYMMETRIC CATALYTIC FIELD

As mentioned above, the inclusion complexes have been explored as catalyst for different organic reactions, particularly for aldol condensation reaction. The aldol condensation is one of the significant C-C bond forming reactions in organic chemistry resulting in the development of diverse catalytic systems for this reaction (Agarwal, *et al.*, 2010, 2012 and 2016). Aldol reactions create functionalized compounds for multifarious applications, such as in industries including pharmaceuticals (Balog, *et al.*, 1998; Ziarani, *et.al.*, 2009), agrochemicals (Kandel, *et al.*, 2012*)*, materials science (Karak, *et al.*, 2018), and synthesis of natural products (Marino, *et al.*, 2002; Durrwacbter, *et al.*,1986; Lu, *et al.*, 2019; Yu, *et al.*, 2023; Shen, *et al.*, 1993). Highly stereoselective aldol condensation reactions are able to produce stereoselective products in high yields.

a) In 2005, the catalytic activity of inclusion complex was initially explored for the aldol reaction (Shen, *et al.*, 2005). Zonxuan Shen et al. had synthesized β-cyclodextrin-immobilized-(4*S*)-phenoxy-(*S*)-proline chiral catalyst by refluxing a mixture of (4*S*)-phenoxy-(*S*)-proline and β-cyclodextrin in ethanol-water (1:1). The formation of the catalyst was confirmed by ^{1}H- NMR, ^{13}C- NMR and UV-vis spectra. The catalytic potential of the catalyst was explored for aldol reaction between acetone and benzaldehyde derivatives in presence of 10 mol% catalyst loading of the immobilized catalyst (Scheme 1). The desired aldol products were obtained in good yields in the range of 76-91 % and with high enantioselectivities in the range of 70-84%.

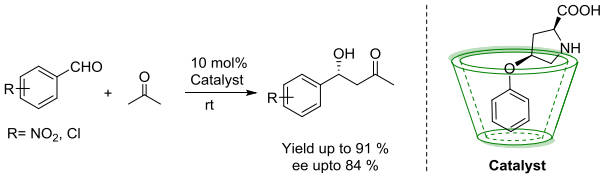

Scheme 1: Aldol reaction between acetone and arylaldehydes

b) In 2007, Junmin Huang et al. had explored a *tert*-butyl phenoxy-L-proline cyclodextrin as immobilized catalyst (Huang, *et al.*, 2007). In this reaction, *in situ* inclusion complex was generated and applied for the direct aldol reaction of cyclohexanone with arylaldehyde in water. The 2 mol% catalyst loading of the organocatalyst afforded the corresponding aldol products in excellent yields with >89% diastereoselectivities and >93% enantioselectivities. The organocatalyst was partially soluble in water. The hydrophobic reactants associated with the catalyst and formed tiny oil droplets to make the reaction feasible. These tiny droplets were floating on water which carried out the reaction successfully in water.

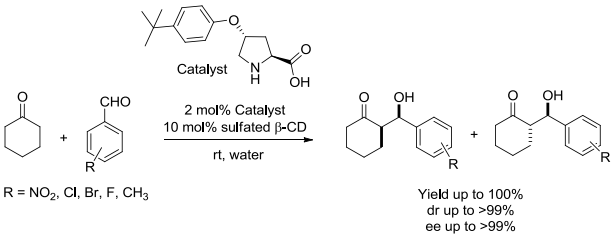

Scheme 2: Aldol reaction between cyclohexanone and arylaldehydes

In 2020, our group developed an inclusion complex between a carbohydrate-based molecule and β-Cyclodextrin (Rani, *et al.*, 2020). The chosen carbohydrate moiety was a D-glucosamine derivative, which could be achieved using a 3-steps process from the commercially available D-glucosamine. The inclusion complex was synthesized using ultrasonication energy. Initially, the D-glucosamine derivative and β-CD were dissolved in ethanol-water and then sonicated for 15 minutes to achieve the corresponding inclusion complex in high yields (Scheme 3).

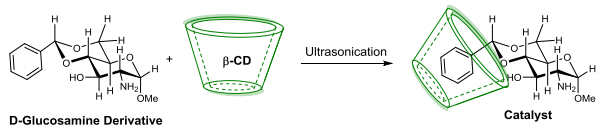

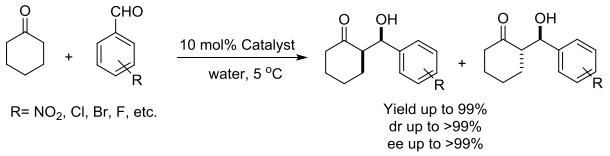

Scheme 3: Aldol reaction catalyzed by carbohydrate-based inclusion complex.

The formation of inclusion complex was confirmed by ^{1}H- NMR, ^{13}C- NMR spectra, while the morphology of IC was determined by SEM images, which revealed the presence of irregular small structure of the catalyst indicating the high surface area. Thermo gravimetric analysis (TGA) revealed the high thermal stability of the IC. Initially, the catalytic activity of IC was tested for the reaction between 3-nitro-benzaldehyde and cyclohexanone in diverse polar and non-polar solvent. Among all, water afforded the corresponding aldol product with 98% yield and high level of dr (>99%) and ee (98%). The catalytic activity of the catalyst was also explored for the reactions between isatin and cyclic ketones providing the corresponding oxindole products in high yields (ranging between 87-98 %) with 66-99 % dr and up to 98 % ee.

CONCLUSION

The unique structural properties of β-CD & its ability to form inclusion complexes make them a suitable host molecule for a variety of small organic molecules. They can encapsulate the guest molecules into their hydrophobic cavity and may enhance their water solubility due to the hydrophilic exterior. When, an organocatalyst or its hydrobobic moiety play a role of guest molecule, then the resulting complex may wok as heterogeneous and aqueous organocatalyst. Moreover, encapsulation increases the stability of the catalyst by protecting it from air and moisture. It also reduces the catalyst loading and enhances the rate of reaction. In the catalytic process, the β-CD may allow the substrates of specific shape & size to enter in its cavity based on the polarity (hydrophobic/non-polar) of reaction medium and its bulky structure may provide the stereo-control to the reaction for producing the stereo-selective products. Overall, using the β-CD based inclusion complexes as catalysts in asymmetric catalytic processes is an excellent concept for generating the eco-friendly, but efficient catalytic systems. They can be easily separated from the reaction mixture and recycled as catalysts for several cycles.

ACKNOWLEDGEMENTS

The authors are grateful to Science and Engineering Research Board (SERB), Delhi (Grant no CRG/2021/006506) and Council of Scientific & Industrial Research (CSIR), Delhi (Grant no 02/0475/23/EMR-II) for providing the financial assistance. Navneet Taya thanks to Panjab University for fellowship. Divya Tagra thanks to the University Grant Commission for the award of junior research fellowship (NTA Ref. No.201610053072).

CONFLICT OF INTEREST

There is no conflict of interest

REFERENCES

Munisamy, M.; Sonaimuthu, M.; Krishnamoorthy, S.; Thambusamy, N-phenyl-1-naphthylamine/β-cyclodextrin inclusion complex as a new fluorescent probe for rapid and visual detection of Pd^{2+}, S. Spectrochim. Acta, Part A. **2014**, 133, 73-79.

Stella, J. V.; He, Q. Cyclodextrins, Toxicol. Pathol. 36, **2008**, 30-42.

Li, K.; Wu, X.; Gu, Q.; Ma, W.; Ni, W. Inclusion complexes of organic salts with β-cyclodextrin as organocatalysts for CO2 cycloaddition with epoxides, RSC Adv. **2017**, 7, 14721-14732

Loftson, T.; Duchene, Cyclodextrins and their pharmaceutical applications, D. Int. J. Pharm. **2007**, 309, 1-11.

Jacob, S; Nair AB. Cyclodextrin complexes: Perspective from drug delivery and formulation. Drug Dev. Res. **2018**, 201-217.

Sett, R.; Sen, S.; Paul, B. K.; Guchhait, N. Effect of temperature and salts on niosome-bound anti-cancer drug along with disruptive influence of cyclodextrins. Spectrochim. Acta A Mol. Biomol. Spectrosc. **2020**, 118261.

Aguado, R.; Murtinho, D.; Valente, A. J. M. Association of antioxidant monophenolic compounds with β-cyclodextrin-functionalized cellulose and starch substrates. Carbohydr Polym. **2021**, 118189.

Liang, S.; Ma, X.; Li, M.; Yi, Y.; Gao, Q.; Zhang, Y.; Zhang, L.; Zhou, D.; Xiao, S. Novel β-Cyclodextrin-Based Heptavalent Glycyrrhetinic Acid Conjugates: Synthesis, Characterization, and Anti-Influenza Activity. Front. Chem. **2022**, 836955.

Ozon, E. A.; Novac, M.; Gheorghe, D.; Musuc, A. M.; Mitu, M. A.; Sarbu, I.; Anuta, V.; Rusu, A.; Petrescu, S.; Atkinson, I.; Lupuliasa, D. Formation and Physico-Chemical Evaluation of Nifedipine-hydroxypropyl-β-cyclodextrin and Nifedipine-methyl-β-cyclodextrin: The Development of Orodispersible Tablets. Pharmaceuticals (Basel). **2022**, 993.

Zhao, X.; Qiu, N.; Ma, Y.; Liu, J.; An, L.; Zhang, T.; Li, Z.; Han, X.; Chen, L. Preparation, characterization and biological evaluation of β-cyclodextrin-biotin conjugate based podophyllotoxin complex. Eur. J. Pharm. Sci. **2021**, 105745.

Ma, Y.; Li, J.; Liu, Y.; Dou, N.; Mu, S.; Wei, X.; Bilawal, A.; Hou, J.; Jiang, Z. Lactitol and β-cyclodextrin alleviate the intensity of goaty flavor. J Sci Food Agric. **2023**, 1588-1592.

Lai, D.; Zhou, A.; Tan, B. K.; Tang, Y.; Sarah-Hamzah, S.; Zhang, Z.; Lin, S.; Hu, J. Preparation and photodynamic bactericidal effects of curcumin-β-cyclodextrin complex. Food Chem. **2021** 361, 130117.

Chodankar, D.; Vora, A.; Kanhed A. β-cyclodextrin and its derivatives: application in wastewater treatment. Environ. Sci. Pollut. Res. Int. **2022**, 1585-1604.

Kadam, V. V.; Balakrishnan, R. M.; Ettiyappan, J. P. Fluorometric detection of bisphenol A using β-cyclodextrin-functionalized ZnO QDs. Environ. Sci. Pollut. Res. Int. **2021,** 11882-11892.

Alanazi F, Salah D. Gold nanoparticles incorporated with Cyclodextrins and its applications. J. Biomater. Nanobiotechnol. **2021**, 2(4), 79-97

Agotegaray, M.; Blanco, M. G.; Campelo, A.; García, E.; Zysler, R.; Massheimer, V.; De Rosa, M. J.; Lassalle, V. β-cyclodextrin coating: improving biocompatibility of magnetic nanocomposites for biomedical applications. J. Mater. Sci. Mater. Med. **2020**, 31(2), 22.

Wang, T.; Bai, Z.; Wei, W.; Hou, F.; Guo, W.; Wei, A. β-Cyclodextrin-Derivative-Functionalized Graphene Oxide/Graphitic Carbon Nitride Composites with a Synergistic Effect for Rapid and Efficient Sterilization. ACS Appl. Mater. Interfaces. **2022**, 474-483.

Dalal, D. S.; Patil, D. R.; Tayade Y. A. β-Cyclodextrin: A Green and Efficient Supramolecular Catalyst for Organic Transformations. Chem. Rec. **2018,** 1560-1582.

Tajbakhsh, M.; Naimi-Jamal M. R.; Balalaie S.; Rezaeian M. A green protocol for the one-pot synthesis of 3,4-disubstituted isoxazole-5(4H)-ones using modified β-cyclodextrin as a catalyst, Scientific Reports **2022**, 12, 19106

Khan, R. I.; Pitchumani, K. Quinolinium modified β-cyclodextrin: An ionic ligand towards sustainable A3-coupling and tandem cyclisation reactions of aldehydes, amines and alkynes, Mol. Catal. **2022**, 519, 112151

Mitra, B.; Pariyarb, G. C.; Ghosh P. β -Cyclodextrin: a supramolecular catalyst for metal-free approach towards the synthesis of 2-amino-4,6-diphenylnicotinonitriles and 2,3-dihydroquinazolin-4(1H)-one, RSC Adv., **2021**, 11, 1271–1281

Tugny, C.; Rio, N.; Koohgard, M.; Vanthuyne, N.; Lesage, D.; Bijouard, K.; Zhang, P.; Suárez, J. M.; Roland, S.; Derat,E.; Bistri-Aslanoff, O.; Sollogoub, M.; Fensterbank, L.; Mouriès-Mansuy V. β-Cyclodextrin−NHC−Gold(I) Complex (β-ICyD)AuCl: A Chiral Nanoreactor for Enantioselective and Substrate-Selective Alkoxycyclization Reactions, ACS Catal. **2020**, 10, 5964−5972

Frijlink, H. W.; Lerk, C. F. The effects of cyclodextrins on drug absorption II. In vivo observations, Int. J. Pharm. **1990**, 195-205

Szente, L.; Szeman. Cyclodextrins in analytical chemistry: host–guest type molecular recognition, J. Anal. Chem. **2013**, 8024-8030.

Tiwari, G.; Tiwari, R.; Rai. A. K. Cyclodextrins in delivery systems Applications, J. Pharm. Bioall. Sci. **2010**, 2, 72-79.

Shen, Z.; Ma, J.; Liu, Y.; Jiao, C.; Li, M.; Zhangi, Y. *β*-Cyclodextrin-Immobilized (4S)-Phenoxy-(S)-proline as a Catalyst for Direct Asymmetric Aldol Reactions, Chirality. **2005**, 17, 556-558.

List, B. Proline-catalyzed asymmetric reactions, Tetrahedron. **2002**, 58, 5573-5590.

Abello, S.; Medina, F.; Tichit, D.; Pe´rez-Ramı´rez, J.; Sueiras, J.E.; Salagre, P.; Cesteros, Y. Aldol condensation of campholenic aldehyde and MEK over activated hydrotalcites, Applied Catalysis B: Environmental**. 2007**, 70, 577–584

Agarwal, J. Progress in aminosugar derived asymmetric organocatalysis. Org. Biomol. Chem. **2016**, 14, 10747−10762.

Agarwal, J.; Peddinti, R. K. Highly efficient and solvent-free direct aldol reaction catalyzed by glucosamine-derived prolinamide. Tetrahedron: Asymmetry **2010**, 21, 1906−1909.

Agarwal, J.; Peddinti, R. K. Synthesis and characterization of monosaccharide derivatives and application of sugar-based prolinamides in asymmetric synthesis. Eur. J. Org. Chem. **2012**, 6390−6406.

Balog, A.; Harris, C.; Savin, K.; Zhang, X.; Chou, T. C.; Danishefsky, S. J. A Novel Aldol Condensation with 2-Methyl-4-pentenal and Its Application to an Improved Total Synthesis of Epothilone B, Angew. Chem. Int. Ed. **1998**, 37, 2675-2678

Ziarani, M.; Ghodsi, Badiei, Abbasi, A.; Farahani, A.; Zahra, Cross-aldol Condensation of Cycloalkanones and Aromatic Aldehydes in the Presence of Nanoporous Silica-based Sulfonic Acid (SiO2-Pr-SO3H) under Solvent Free Conditions, Chin. J. Chem. **2009**, 27, 1537-1542

Kandel, K.; Althaus, S. M.; Peeraphatdit, C.; Kobayashi, T.; Trewyn, B. G.; Pruski, M.; Slowing, I. I. Substrate inhibition in the heterogeneous catalyzed aldol condensation: A mechanistic study of supported organocatalysts, J. Catal. **2012**, 291, 63–68

Karak, M.; Oishi, T.; Torikai, K. Synthesis of anti-tubercular marine alkaloids denigrins A and B, Tetrahedron Lett. **2018**, 59, 2800–2803

Marino, J. P.; Rubio, M. B.; Cao, G.; Dios, A. Total Synthesis of (+)-Aspidospermidine: A New Strategy for the Enantiospecific Synthesis of Aspidosperma Alkaloids, J. Am. Chem. Soc. **2002**, 124, 13398-13399

Durrwacbter, J. R.; Drueckbammer, D. G.; Nozaki, K.; Sweers, H. M.; Wong, C. Enzymatic Aldol Condensation/Isomerization as a Route to Unusual Sugar Derivatives, J. Am. Chem. Soc. **1986**, 108, 7812-7818

Lu, J.; Koldasa, S.; Fan, H.; Desper, J.; Day, V. W.; Hu, D. H. A One-Pot Intramolecular Tandem Michael–Aldol Annulation Reaction for the Synthesis of Chiral Pentacyclic Terpenes, Synth. **2019**, 51, 3964–3972

Yu, X.; Gu, X.; Zhao, Y.; Wang, F.; Sun, W.; Qi, C.; Gu, L.; Zhang, Y. Collective synthesis of aspulvinone and its analogues by vinylogous aldol condensation of substituted tetronic acids with aldehydes, RSC Adv. **2023**, 13, 4859–4864

Shen, B.; Hutchinson, C. R. Tetracenomycin F2 Cyclase: Intramolecular Aldol Condensation in the Biosynthesis of Tetracenomycin C in Streptomyces glaucescens, Biochem. **1993**, 32, 11149-11154

Huang, J.; Zhang, X.; Armstrong, D. W. Highly Efficient Asymmetric Direct Stoichiometric Aldol Reactions on/in Water, Angew. Chem. Int. Ed. **2007**, 46, 9073 –9077

Rani, D.; Sethi, A.; Kaur, K.; Agarwal J. Ultrasonication-Assisted Synthesis of a D-Glucosamine-Based β-CD Inclusion Complex and Its Application as an Aqueous Heterogeneous Organocatalytic System, J. Org. Chem. **2020**, 85, 9548−9557.

EVALUATION OF PHOTOTHERMAL INDUCED BACTERICIDAL EFFICIENCY OF GOLD NANOSTARS

Sunaina Kaul[a,b], Ankush Bajaj[b], Nitesh Priyadarshi[a], Nitin Kumar Singhal[a,b*]

[a] *National Agri-Food Biotechnology Institute, Sector-81 Mohali, 140306, India*

[b]*Department of Biotechnology, Panjab University, Sector 25, Chandigarh, 160014, India*

ABSTRACT

The rising threat of antimicrobial resistance (AMR) represents global concern for the clinicians. The photothermal therapy (PTT) utilizing gold nanostructures has drawn significant interest as a potent strategy in combating pathogens, including drug-resistant ones. Herein the PTT effect of synthesized Gold nanostars (AuNst) were studied for antimicrobial action. *In-vitro* spread plate assays were evaluated using Gram negative, *E.coli* and Gram positive, *S. aureus* as model organisms for study. *S. aureus* exhibited lower survival rates in comparison to *E. coli*. These findings highlight the potential future prospects of AuNst as a PTT agent, offering effective antibacterial activity.

KEYWORDS: Antimicrobial resistance, Gold nanostars and photothermal treatment.

INTRODUCTION

Antimicrobial resistance (AMR) has become a critical global challenges for public health to be dealt with in the 21st century (Prestinaci et al., 2015). Over and inappropriate antibiotic consumption has been the primary contributor to bacterial non-susceptibility towards commonly available antibiotics, leading to high morbidity and mortality in clinical settings. As per the Centers for Disease Control and Prevention (CDC), annually over two million individuals in the United States are affected with illnesses caused by antibiotic-resistant pathogens, leading to a minimum of 23,000 fatalities (Solomon & Oliver, 2014). The primary obstacle lies in the burden of multidrug resistance exhibited by six pathogens, that has been prioritized by the World Health Organization (WHO). Collectively referred to as ESKAPE, namely *Escherichia coli (E. coli), Staphylococcus aureus (S. aureus), Klebsiella pneumoniae (K. pneumoniae), Acinetobacter baumannii (A. baumanni), Pseudomonas aeruginosa (P. aeruginosa)* and *Enterobacter* significantly contribute to the overall challenge of AMR (WHO, 2017a).

With the gaining prevalence of drug resistance in bacteria, it has become essential to eradicate multi-drug resistant bacteria, by bactericidal alternatives. Over the past few decades, there has been a notable interest in photothermally active nanoparticles (PANs), of metallic origin. They exhibit absorption ranging from visible-to-near-infrared (NIR) region and allow temperature elevation in the surrounding medium upon irradiation (Guo et al., 2020; Pallavicini et al., 2020).

Among the various types of gold nanostructures, Gold nanostars (AuNst), multibranched gold nanoparticles characterized by a spherical core and multiple branches. They possess highly concentrated electron density at the tips of their branches, resulting in a substantial amplification of the particle's interaction with photons enhancing their effectiveness of photothermal therapy (PTT) (Kim & Lee, 2018; Lavaee et al., 2021)

As per the previous literature, ~ 40% *S. aureus* killing was achieved, in this manuscript we have explored the photothermal efficiency of AuNst and its application in bacterial reduction. Taking into consideration the unique properties of AuNst, herein we have synthesized AuNst and evaluated their efficacy as PTT agents against Gram-positive microorganism S*taphylococcus aureus* and Gram-negative microorganism *Escherichia coli.*

MATERIALS & METHODS

Gold chloride ($HAuCl_4 \cdot 3H_2O$), Triton-X (Surfactant), Sodium Borohydride ($NaBH_4$), Silver nitrate ($AgNO_3$), Ascorbic Acid were purchased from Sigma-Aldrich; Carboxymethyl-PEG-Thiol (CM-PEG-SH) (Laysan Bio). Bacterial cultures *E. coli* (MTCC443) and *S. aureus* (MTCC 87) were procured from MTCC, IMTECH Chandigarh.

Corresponding author: nitin@nabi.res.in
Received: September 10, 2022, Accepted: November 15, 2022

Using a previously described technique and the surfactant Triton-X (0.1 M), AuNst were produced (Atta et al., 2019). The surfactant's micelles confined the gold metallic ions, allowing for gradual reduction and encouraging the development of spikes. 10 mL of seeds were then added to the $HAuCl_4$ and $AgNO_3$ growing solution. The seeds served as the nucleation foci for the spike growth in the presence of 78 mM Ascorbic acid, a reducing agent. UV-Vis-NIR spectroscopy was used to describe the synthesized AuNst, charge analysis using a zeta analyzer was used to determine whether the pegylation of the AuNst had been successful, and scanning electron microscopy (SEM) and transmission electron microscopy (TEM) were used to assess the surface morphology.

Bacterial cultures were revived after incubating a bacterial colony in LB broth at 37 °C, with shaking at 220 rpm, overnight.The log phase bacterial suspensions, 300 µL (10^4 cells/mL in LB Broth) were kept for 30 sec under LASER (808nm excitation) with optimized concentration of AuNst. Temperature monitoring with photothermal treatment was carried out using temperature sensitive camera application FLIR One.

To estimate bacterial relative viability,100 µL aliquot of each reaction mixture was spread on LB agar plates and kept for overnight incubation at 37°C to allow growth of colonies. The colony forming unit (CFU) were counted and the following formula was used to determine the relative viability/survival ratio% and the quantity of colony forming units (CFU):

$$\textbf{Survival ratio (\%)} = \frac{CFU}{CFUo} \times 100\%$$

Based on the experiments conducted, the data was determined as the mean value± standard deviation, with n=3. One-way analysis of variance (ANOVA) was used to evaluate statistical significance, with p values: ****p<0.0001.

Under FE-SEM, the cell morphology of model bacterial organisms exposed to LASER radiation was examined with and without incubation with AuNst. Following fixation with glutaraldehyde (2.5%), dehydration procedures using a graduated ethanol series (30%, 50%, 70%, 90%, 100%) were carried out (Priyadarshi et al., 2022). Then, drop casting was done with the fixed samples onto the silicon wafer. After 5 nm gold sputtering, the examination was performed at various magnifications with an acceleration voltage of 5–10 kV.

RESULTS & DISCUSSIONS

The UV absorption spectrum showed a peak at 1100 nm as shown in Fig. 1 (a), while the DLS Zetasizer showed the charge on PEGylated AuNst was around -33mV. The TEM and SEM images of the synthesized AuNst were depicted in Figure 1(b), spike lengths (100nm), and overall geometry of AuNst. The results obtained were in accordance with earlier reported study(Kaul et al., 2022).

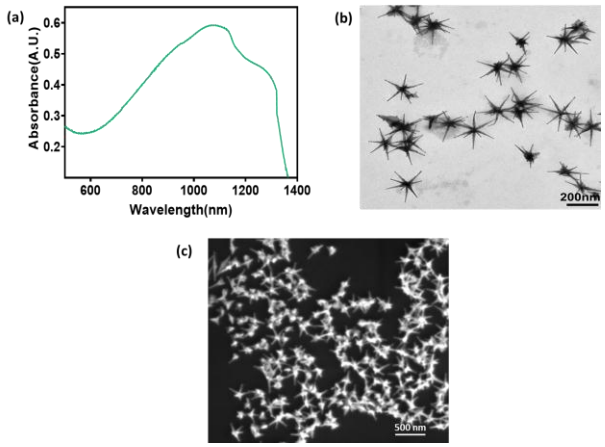

Figure 1: Characterizations of the synthesized AuNst (a) UV spectrum of the nanostructures synthesized (b) TEM and (c) FE-SEM images of AuNst

Subjecting the *E.coli* to AuNst-NIR radiation at 808 nm for 30 seconds yielded significant outcomes. The temperature rose to 56°C for 2 OD AuNst + NIR, as shown in Fig. 2. Similar results were obtained in the *S. aureus* PTT assay. Notably, the temperature exhibited a substantial rise when exposed to varying concentrations of AuNst combined with NIR radiation from 33.1°C to 51.9 °C for 2 OD AuNst + NIR, as illustrated in Fig. 3. In the spread plate assays, better bacterial killing efficiency was obtained for *S. aureus* which was similar to the results obtained earlier (Yin et al., 2014). The relative survival ratios of various photothermal treatment strategies for *E. coli* and *S. aureus* have been represented in Fig 4 which were found to be ~60% (*E. coli*) and 40% (*S. aureus*) with 1O.D. of AuNst and PTT therapy combined. When the concentration of AuNst was doubled and LASER treatment applied relative

INSITU SEPARATION OF BACTERIA FROM CONTAMINATED SAMPLE BY GLYCAN FUNCTIONALIZED MNPs

Nitesh Priyadarshi[1], Jaspreet Kaur[1], Veni Chawla[1], Nitin Kumar Singhal*[1]

[1]National Agri-Food Biotechnology Institue (NABI), Mohali-140306, Punjab, India

ABSTRACT

Foodborne illnesses are the major cause of mortality and morbidity among children worldwide. Several foodborne bacteria are responsible for foodborne infections, which are present in water, food, environment, and surroundings. It is a global concern to make food and water free from bacterial contamination. Several techniques have been used for decontamination of contaminated samples. Advanced technologies like nanotechnologies are proven to be specific, sensitive, and efficient as compared to traditional technologies for the removal of bacteria from contaminated samples. Nanotechnologies offer a range of nanoparticles like gold nanoparticles, magnetic nanoparticles, silver nanoparticles, etc. These nanoparticles have unique characteristics, and they can be used for different applications, magnetic nanoparticles (MNPs) have a magnetic property and can be used for the separation of functionalized MNPs from samples by applying an external magnetic field. MNPs are an upcoming class of nanomaterial used extensively in various translational applications. Here in we have coated gold onto MNPs to give Localized surface plasmon resonance (LSPR) property, then stabilized the formulation with $PEG_{1000.}$ For specific receptor-ligand interaction, we have conjugated two different glycans onto MNPs and targeted the lectins present on the bacterial surface. The specific interaction between lectins and carbohydrate result in the adherence of bacteria to glycan-functionalized MNPs. The adhered bacteria can be separated by the use of an external magnetic field. The mannose functionalized MNPs were able to separate 78.34% of bacteria from the contaminated sample. The current nanoformulations can be used to remove bacteria from contaminated samples.

Keywords: Bacteria, Glycans, Lectins, MNPs, Foodborne pathogens.

INTRODUCTION

Foodborne diseases are a significant cause of death across the world. As per the World health organization (WHO), foodborne bacteria contribute to 600 million illnesses and 420,000 mortality annually (Lee & Yoon et al., 2021). Some of the bacteria commonly associated with foodborne infections are *E.coli*, *L.monocytogenes*, *S. aureus*, *P.aeruginosa*, etc. These bacteria are responsible for several outbreaks in India and worldwide due to the development of drug resistance (Srinivasan et al., 2014). The removal of these bacteria from a contaminated sample is essential to minimize the food borne outbreaks. The removal of bacteria is indeed needed to provide global food security (Dilawari et al., 2021; Dilawari et al., 2022). The separation of bacteria from food is complex and needs new technology for the efficient removal of bacteria from complex food material. Various old-age technologies have been used in the separation of bacteria from a sample, like filtration, centrifugation, etc. These traditional techniques are non-specific and not efficient in the removal of bacteria. New age technology like nanotechnology are upcoming field and has several magnitudes of potential in tackling modern problems (Mondal et al., 2023) like detection (Priyadarshi et al., 2023) (Gupta et al., 2020) and removal of bacteria from complex food material (Singhal et al., 2023). Nanomaterials offers a range of nanoparticle like gold nanoparticle (AuNPs) (Priyadarshi et al., 2022), Gold Nanostars (Kaul et al., 2022), magnetic nanoparticles (MNPs) (Gupta et al., 2023), silver nanoparticles (AgNPs), etc. with multidirectional properties. Here we have used MNPs due to their magnetic property. In the present work, we have explored the carbohydrate-lectin interaction (Becker et al., 2023). Each bacteria have a signature lectin present on its surface, and this lectin binds to targeted carbohydrates (Kaushal et al., 2019). The specific interaction between lectin and carbohydrates has been explored in the present study for the specific capture of bacteria. In a nutshell, glycan-functionalized MNPs have been used to isolate bacteria from contaminated samples.

Corresponding author: nitin@nabi.res.in
Received: September 10, 2022, Accepted: November 15, 2022

MATERIALS AND METHODS

For the current work we used different materials like-Gold(III) chloride ($HAuCl_4$), Sulfuric acid (H_2SO_4), Poly (ethylene glycol) 2-mercaptoethanol ether acetic acid (PEG_{1000}), 4-aminophenyl α-d-mannopyranoside, 4-aminophenyl β-d-galactopyranoside, Sodium chloride (NaCl), Iron (III) chloride hexahydrate ($FeCl_3 \cdot 6H_2O$), Iron (II) chloride tetrahydrate ($FeCl_2 \cdot 4H_2O$), were purchased from Sigma and used without any further purification. EDC (1-ethyl-3-(3-dimethyl aminopropyl) carbodiimide hydrochloride) was purchased from Thermofisher Scientific. MTCC 1610 (*E.coli*) and MTCC 1934 (*Pseudomonas aeruginosa*) were procured from MTCC, CSIR-IMTECH, Chandigarh. The synthesis of glycan-functionalized MNP consists of several steps (Figure 1). The magnetic nanoparticles (Fe3O4) were first synthesized by the use of two different compounds of iron. The reduction of $FeCl_2 \bullet 7H_2O$ and $FeCl_3 \bullet 6H_2O$ chlorides in an aqueous ammonia solution while vigorously swirling produced the magnetic nanoparticles. In 25 ml of a 0.4 M HCl solution, 5.4 g of $FeCl_3 \bullet 6H_2O$ and 2.0 g of $FeCl_2 \bullet 4H_2O$ were dissolved. 250 ml of a 1.5 M NaOH solution received the solution dropwise while being vigorously stirred. Immediately, a black precipitate started to form (Singh et al., 2018). The precipitate was obtained by magnetic decantation, and it was then washed four times with 100 ml each of water, 0.1 M tetramethylammonium hydroxide pentahydrate, and water again. The final precipitate was then dissolved once more in 0.1 M TMAOH solution and kept in the dark for further use. The MNPs were then functionalized with gold by the method reported by S. Banerjee (Banerjee et al., 2011), and then it was functionalized with PEG_{1000} by adding 10µl of 10mg/mL PEG_{1000} to the MNPs and kept at gentle stirring for around 3-4 hrs. The pegylation was confirmed by a salt test by adding 10µl of 0.1M NaCl to the pegylated MNPs and bare MNPs. Further, glycan conjugation was done to the pegylated MNPs with the aid of EDC (10µl of 10mg/mL) to the pegylated MNPs followed by the addition of 4-aminophenyl α-d-mannopyranoside, 4-aminophenyl β-d-galactopyranoside separately and kept for gentle stirring at room temperature for 2-3hrs. Further, the solutions were washed separately by using a magnetic separator.

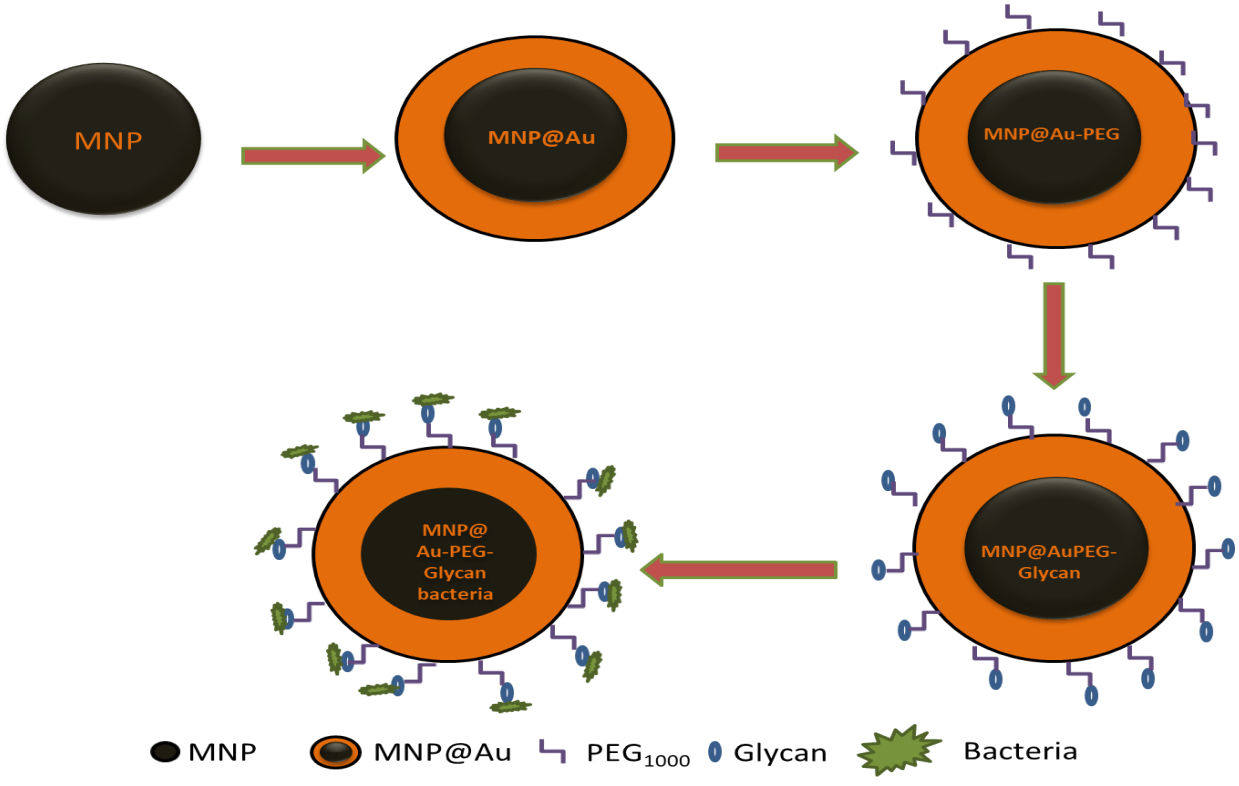

Figure 1: Schematic representation of MNP and process of glycan functionalization over the MNPs and bacteria capture.

ACKNOWLEDGMENT

Department of Science and Technology (DST)-CRG/2019/00482, Department of Biotechnology (Core Grant), National-Agri Food Biotechnology Institute (NABI), Mohali

REFERENCES

Banerjee, S., Raja, S.O., Sardar, M., Gayathri, N., Ghosh, B. and Dasgupta, A., 2011. Iron oxide nanoparticles coated with gold: Enhanced magnetic moment due to interfacial effects. Journal of Applied Physics, 109(12).

Becker, J., Terracciano, R., Yilmaz, G., Napier, R. and Becer, C.R., 2023. Step-Growth Glycopolymers with a Defined Tacticity for Selective Carbohydrate–Lectin Recognition. Biomacromolecules, 24(4), pp.1924-1933.

Dilawari, R., Kaur, N., Priyadarshi, N., Kumar, B., Abdelmotelb, K.F., Lal, S.K., Singh, B., Tripathi, A., Aggarwal, S.K., Jat, B.S. and Mehta, S., 2021. Genome editing: a tool from the vault of science for engineering climate-resilient cereals. Harsh environment and plant resilience: molecular and functional aspects, pp.45-72.

Dilawari, R., Kaur, N., Priyadarshi, N., Prakash, I., Patra, A., Mehta, S., Singh, B., Jain, P. and Islam, M.A., 2022. Soybean: A key player for global food security. In Soybean Improvement: Physiological, Molecular and Genetic Perspectives (pp. 1-46). Cham: Springer International Publishing.

Gupta, R., Sagar, P., Priyadarshi, N., Kaul, S., Sandhir, R., Rishi, V. and Singhal, N.K., 2020. Nanotechnology-based approaches for the detection of SARS-CoV-2. Frontiers in Nanotechnology, 2, p.589832.

Gupta, R., Singh, V., Sarawagi, N., Kaur, G., Kaur, R., Priyadarshi, N., Rishi, V., Goyal, B., Mishra, P.P. and Singhal, N.K., 2023. Salmonella typhimurium detection and ablation using OmpD specific aptamer with non-magnetic and magnetic graphene oxide. Biosensors and Bioelectronics, 234, p.115354.

Hargol Zadeh, S., Kashanian, S. and Nazari, M., 2023. A Label-Free Carbohydrate-Based Electrochemical Sensor to Detect Escherichia coli Pathogenic Bacteria Using D-mannose on a Glassy Carbon Electrode. Biosensors, 13(6), p.619.

Kaul, S., Sagar, P., Gupta, R., Garg, P., Priyadarshi, N. and Singhal, N.K., 2022. Mechanobactericidal, gold nanostar hydrogel-based bandage for bacteria-infected skin wound healing. ACS Applied Materials & Interfaces, 14(39), pp.44084-44097.

Kaushal, S., Priyadarshi, N., Pinnaka, A.K., Soni, S., Deep, A. and Singhal, N.K., 2019. Glycoconjugates coated gold nanorods based novel biosensor for optical detection and photothermal ablation of food borne bacteria. Sensors and Actuators B: Chemical, 289, pp.207-215.

Lee, H. and Yoon, Y., 2021. Etiological agents implicated in foodborne illness world wide. Food science of animal resources, 41(1), p.1.

Mondal, P., Nandan, A., Ajithkumar, S., Siddiqui, N.A., Raja, S., Kola, A.K. and Balakrishnan, D., 2023. Sustainable application of nanoparticles in wastewater treatment: Fate, current trend & paradigm shift. Environmental Research, p.116071.

Priyadarshi, N. and Singhal, N.K., 2023. Quartz Crystal Microbalance (QCM)-Based Nanosensors for the Detection of Pathogenic Bacteria. In Nanosensors for Point-of-Care Diagnostics of Pathogenic Bacteria (pp. 143-167). Singapore: Springer Nature Singapore.

Priyadarshi, N., Ambule, M.D., Kaushal, S., Kumar, A., Sagar, P., Srivastava, A.K. and Singhal, N.K., 2022. Nanoglycocluster based diagnostic platform for colorimetric detection of bacteria; A comparative study analysing the effect of AuNPs size, linker length, and glycan diversity. Biosensors and Bioelectronics, 201, p.113969.

Singh, V., Kaul, S., Singla, P., Kumar, V., Sandhir, R., Chung, J.H., Garg, P. and Singhal, N.K., 2018. Xylanase immobilization on magnetite and magnetite core/shell nanocomposites using two different flexible alkyl length organophosphonates: Linker length and shell effect on enzyme catalytic activity. International journal of biological macromolecules, 115, pp.590-599.

Singhal, N.K., Garg, P., Priyadarshi, N., Ambule, M., Kaur, G., Kaul, S., Gupta, R., Sagar, P., Bajaj, G., Rishi, V. and Goyal, B., 2023. Multiepitope glycan based laser assisted fluorescent nanocomposite with dual functionality for sensing and ablation of Pseudomonas aeruginosa. *Nanoscale*.

Srinivasan, V.B., Singh, B.B., Priyadarshi, N., Chauhan, N.K. and Rajamohan, G., 2014. Role of novel multidrug efflux pump involved in drug resistance in Klebsiella pneumoniae. PLoS One, 9(5), p.e96288.

CHANDIGARH SCIENCE CONGRESS-2022 (CHASCON-2022) A REPORT

***Desh Deepak Singh,[1] Shally Sharma,[1] Janvi Sandhu,[1] Amandeep Singh,[1] Lovepreet Singh,[1] Maaniya,[1] Usha Mathur,[1] Sandeep Sahijpal[2]**

Biotechnology Department, Panjab University, Chandigarh, INDIA

Physics Department, Panjab University, Chandigarh, INDIA

Panjab University, Chandigarh, in association with the Chandigarh Region Innovation and Knowledge Cluster (CRIKC) organized the 15th Chandigarh Science Congress (CHASCON-2022) from September 15th to 17th, 2022 on the theme **"Towards Holistic Development of Science and Technology through Interdisciplinary Approach"**. The theme was chosen realizing that the integration of various fields of science and technology is key feature towards a holistic development. Panjab University, with the CRIKC institutions has been organizing CHASCON every year since 2007. The Congress has come a long way and continues to encourage young and innovative minds by providing them with a suitable platform for interaction with researchers, academicians, and policy planners from all over the country. More than 850 participants registered for the congress and the three days activities included lectures by eminent speakers, panel discussions, competitions and student presentations. The 15th Chandigarh Science Congress was an event to showcase recent developments in science and technology and presented a platform to create a roadmap for future developments and research translations.

After a tumultuous lockdown of 2 years, the congress was organized in the offline mode to facilitate smooth interaction between speakers and the audience. The congress spanned over three days from September 15th-17th, 2022 and included both general and section specific scientific talks that finally ended with a booming cultural evening. The general lectures were organized at the Law Auditorium, PU, while the section specific activities were held at respective departments of different sections.

To begin with, on 15th September 2022, the Coordinator of the event *Prof. Desh Deepak Singh* warmly welcomed the audience, guests and speakers, and initiated the event with a brief introduction. *Prof. Raj Kumar (Hon'ble Vice Chancellor), Prof. Renu Vig (Dean of University Instruction) and Prof. Sudhir Kumar (Director Research and Development)* inaugurated the event and expressed their enlightening insights into the goal and purpose of the conference. They also emphasized the importance of CHASCON-2022 theme and its relevance in today's science and technology. A short refreshing high-tea break was organized following the inaugural function.

Commencing with the first wing of the scientific sessions, *Prof. Rajeev Ahuja (Director, IIT Ropar)* delivered a technical talk on "*Advanced Modelling of Materials for Clean Energy Applications: Hydrogen Storage Materials and Next-Generation Batteries".* His talk provided an overview of the most recent research developments in the field of hydrogen storage materials and rechargeable batteries, with the focus on how computational material science can play an important role in search and design of new hydrogen storage materials and next generation battery materials. The next speaker, *Prof. Dulal Panda (Director, NIPER,Mohali)* talked about *"Microtubule Targeted Cancer Therapy: Opportunities and Challenges of Targeted Drug Deliverly".* He elaborated on the mechanism of action for microtubule targeted anticancer drugs and explained how anti-microtubule agents are much more successful compared to other antimitotic agents. Further, *Prof. Amitav Patra (Director, INST, Mohali)* gave a technical lecture on *"Nano Hybrid for Photon Harvesting Systems",* and highlighted that the fundamental knowledge of photophysical processes that are crucial for developing efficient light-harvesting systems. The first wing of these scientific sessions was followed by lunch.

The second scientific session unfolded with a plenary talk by *Prof. Yashwant Gupta (Distinguished Professor and Centre Director, NCRA-TIFR, Pune),* titled *"Probing the Universe using Radio Waves: Where*

Corresponding author: ddsingh@pu.ac.in

Received: September 16, 2022, Accepted: November 15, 2022

Engineering Meets Astronomy". Prof. Gupta traced back the fascinating story of Radio Astronomy and the engineering behind it, with a special emphasis on its growth and current status in India, ending with the front-line Indian facility - the Giant Metrewave Radio Telescope (GMRT). The next speaker, *Prof. J. Srinivisan (Distinguished Scientist, IISc Bangalore)* focused his talk on *"Climate Change: Threats and Opportunities".* Finally, *Ms. Hargunjit Kaur (Secretary Industries of Chandigarh Administration)* shared her insight into the Start-up Scenario in India, and encouraged the students to come up with more start-ups. She incentivised them with the support through various policies and funding initiatives.

Following a brief evening tea session, the third wing of scientific talks began with a talk by *Dr. Saikat Chakraborty (Plaksha University, Mohali)* on *"Bioenergy in the Time of Climate Change".* The talk provided a holistic view of the origin and consequences of anthropogenic climate change, and explored technologies for mitigating global warming by replacing fossil fuels with biofuels as transportation fuels. The next speaker *Dr. Ekta Singla (IIT Ropar)* concluded the session with an informative lecture on *"Robotic Frameworks for Industry 4.0: A Journey of Five Decades".* Her talk involved concept-design of reconfiguration manufacturing systems for Industry. The students were delighted to hear from all the dignitaries and the event was a great success. Finally, the first day of CHASCON-2022 concluded with an hour-long cultural event in the evening that was organized by the Panjab University students.

Table 1: A chronology of previous CHASCON:

S. NO.	CHASCON	DATES	THEME	COORDINATOR CO-COORDINATOR (Panjab University)
1	15th CHASCON	September 15-17, 2022	Towards Holistic Development of Science and Technology through Interdisciplinary approach	Prof. Desh Deepak Singh (Biotechnology) Prof. Sandeep Sahijpal (Physics)
2	14th CHASCON	Dec 17-19, 2020	Science and Technology Innovations: Ushering in Era of Make in India	Prof. Desh Deepak Singh (Biotechnology) Prof. Sandeep Sahijpal (Physics)
3	13th CHASCON	Mar 13-15, 2019	Science and Technology for New India	Prof. Rajat Sandhir (Biochemistry) Prof. CN Kumar (Physics)
4	12th CHASCON	Feb 12-14, 2018	Science and Society interface: Exploration of cost effective and efficient technologies through Physical and Natural Sciences	Prof. Promila Pathak (Botany) Prof. Sonal Chawla (Computer Science)
5	11th CHASCON	Mar 9-11. 2017	Advancing Sustainable development through Science Technology and Innovation	Prof. Sukhwinder Singh (UIET) Prof. Indu Pal Kaur (UIPS)
6	10th CHASCON	Feb 29-Mar 2, 2016	Integrative approaches in advancement of Science	Prof. Archana Bhatnagar (Biochemistry)
7	9th CHASCON	2015	Marching Ahead Through Science & Technology Development	Prof. Sanjeev Puri (UIET) Prof. Archana Bhatnagar (Biochemistry)
8	8th CHASCON	2014	Accelerating Scientific Research Through Interaction, Inspiration,Invention & Innovation	Prof. Sanjeev Puri (UIET) Prof. Maninder Karan (UIPS)

9	**7th CHASCON**	**March 1-3, 2013**	**Contemporary Issues and Interdisciplinary Science and Technology for Societal Needs**	**Prof. Sanjay Chibber (Microbiology) Prof. Sanjeev Puri (UIET)**
10	**6th CHASCON**	**2012**		**Respected colleagues**
11	**5th CHASCON**	**Feb 26-28, 2011**	**Building gateway to sustainable green communities**	**Prof. Renu Vig (UIET)**
12	**4th CHASCON**	**March 19-20, 2010**	**Energy Security and Environmental Challenges**	**Prof. Wanchoo (Chemical Engg)**
13	**3rd CHASCON**	**26th to 29th February, 2009**	**Science Education and attraction of talent for excellence in Research**	**Prof. AK Bhati (Physics) Prof. RK Pathak**
14	**2nd CHASCON**	**2008**	**Empowering India by Scientific Integration, Innovation and Invention**	**Prof. OP Katare (UIPS)**
15	**1st CHASCON**	**2007**		**Prof. Nirmal Singh Prof Rajeev Puri (Physics)**

16th September, 2022, the second day of CHASCON-2022, was largely committed to section specific activities. There were 9 scientific sections that include; Basic Medical Sciences, Medical and Dental Sciences, Life Sciences, Pharmaceutical Sciences, Chemical Sciences, Physical Sciences, Mathematical Sciences, Engineering and Management Sciences, and Earth and Environmental Sciences. Each of these section organizers had invited guest speakers for discipline specific lectures, and conducted scientific competitions like oral and poster presentations. The scientific programme included an opportunity for the participants to exhibit their acumen by competing in various events like poster, ural competitions and they were stringently evaluated by their respective section's judging panel. A quiz competition was also organized at the sectional level and the section winners competed against each other at the central level in the Law auditorium which was coordinated by Professor Sanjeev Sharma from UIAMS, PU. The guest speakers, jury and competition winners were felicitated appropriately. A popular lecture by an eminent speaker *Prof. Abha Sur (Massachusetts Institute of Technology, United States)* was organized at the end of second day. She discussed gender parity, diversity and inclusivity in science. Her talk was quite engaging and the audience enjoyed her insight on this topic. The second day of CHASCON-2022 ended on a good note.

The third day of CHASCON-2022, 17th September, 2022, began with plenary talks from eminent dignitaries. The first lecture on *"Role of Interdisciplinary Care in the Management of Cancer"* was delivered by *Prof. Pankaj Malhotra (PGIMER, Chandigarh).* His talk was highly applauded and was quite stimulating. The next speaker *Prof. Gopinath (Plaksha University, Mohali)* focused largely on *"The Vulnerabilities of Financial Apps"* and addressed the key challenging issues revolving around the use of financial computer applications. This was followed by a thought-provoking presentation by *Prof. Ashwani Pareek (Executive Director, NABI, Mohali)* on *"Are We Ready to Feed Nine Billions?"* His talk invigorated the audience to think more on upcoming food crunches and sustainable solutions to overcome these issues. These talks were followed by a brief tea session.

The Congress then proceeded for Panel Discussions – the first being on *"Industry-Academia Interaction for Translation of Scientific Research".* The discussion was partaken by *Ms. Jasneet Kaur (IPR, Legal Affairs Expert), Mr. Amit Sharma (Business Consultant), Ms. Minnie Riat (Industrialist), Mr. Sumanpreet Singh (CII, Chandigarh) and Mr. P.J. Singh (CEO, Tynor).* The experts laid special emphasis on capacity and relation building for strengthening connections and bridging the gap between industry and the academia. Everyone enjoyed a brief lunch afterwards. The next panel discussion themed, *"Role of Languages and Interdisciplinary Approach in Development of Science and Technology"* was also conducted. It was chaired by numerous dignitaries namely, *Prof. Sudhir Kumar (Director, Research & Development Cell, Panjab University), Prof. Gurpal Singh (Panjab University), Dr. Debdulal Saha (IISER, Mohali), Prof. Rupinder Tiwari (Panjab University).* Special focus was laid on

promoting science using vernacular languages for better outreach, propagation and understanding of science. Then a sponsors/Start-up session also went underway wherein CHASCON-2022 sponsors like Merck Pvt. Ltd, M/s Scott Edil, Chandigarh informed the audience about their company, its goals, products and their facilities. After an evening tea break, a valedictory function was organized to pay vote of thanks to each and every one for making CHASCON-2022 a roaring success.

LEVERAGE ANALYSIS ON CERTAIN PRODUCT GRAPHS OF PATH AND CYCLE

Sinumol S* and Sunil Kumar R

*Department of Mathematics, T.K. Madhava Memorial College, Nangiarkulangara (University of Kerala)
Department of Mathematics, Baby John Memorial Govt. College, Chavara (University of Kerala)

ABSTRACT

Some interesting graphs can be obtained from some simpler graphs by different graph operations. The centrality of a graph is an essential concept in graph theory that identifies important nodes in a complex network. The different perspectives of a particular node are studied under different indices, in which the leverage centrality is unique as it considers the extent of connectivity of a node in relation to the connectivities of its neighbors. This paper studies the product graph of path $P_n, n \geq 5$ with cycle $C_m, m \geq 3$ under various graph products for its leverage analysis. Also, the leverage centrality analysis on lexicographic and corona product of paths is investigated. We found that the leverage type of the component graphs is preserved in the corona product, but not in the lexicographic product.

Keywords: - Leverage center, Neural network, Bicentric leverage graph, Tetra centric leverage graph.

INTRODUCTION

Graph operations are operations that produce new graphs from initial ones, which play a significant role in the study of graph decompositions into isomorphic subgraphs. Leverage centrality is a novel centrality measure proposed to identify the critical nodes that are highly influential within a network. The leverage centrality of a node in a network is determined by the extent to which its direct neighbors rely on that node for information (Murat Ersen Berberler, 2020). In the mathematical development of this centrality, leverage centrality of knight's graphs and cartesian products of regular graphs and path powers were investigated by Roger Vargas, Jr. et al., 2017. Leverage centrality analysis of some infrastructure networks were determined by Murat Ersen Berberler, 2020. Also, the leverage centralities of complete multipartite graphs and the cartesian product of paths were investigated by Sharma, Vargas, Waldron, Fl´orez, and Narayan, 2017. In this paper, we are motivated to investigate the leverage centrality of various product graphs of path $P_n, n \geq 5$ with cycle $C_m, m \geq 3$ and also the leverage centrality of lexicographic and corona products of paths $P_n, n \geq 5$. The path is a bicentric leverage tree, but the composition of two paths is a tetra centric leverage graph. Furthermore, we found that the leverage type of the component graphs is preserved in the corona product of paths. Identification of leverage centers has a significant role in diagnosing brain tumors as this centrality is specially designed for neural networks. In this paper, we focused on its mathematical perspective only. The structure of the paper is as follows: The paper has five major sections in which the first describes some basic propositions on leverage centrality and the motivation for the present study. The second section describes the leverage analysis of the product graph of path $P_n, n \geq 5$ with cycle $C_m, m \geq 3$ under different graph products based on the cartesian product of the vertex sets such as the cartesian, the tensor, the strong and the lexicographic products of graphs. The third and fourth sections are dedicated to the leverage centrality analysis on the lexicographic and the corona products of paths. The last section includes a conclusion with the future scope of research. We begin with some basic definitions that are essential for our study.

Definition 1.1 (Narsingh Deo, 2014) The number of edges incident on a vertex v, with self-loops counted twice, is called the degree of a vertex v. We denote it by $deg(v)$.

Now we define the leverage centrality of a node v and the leverage center of a graph G are as follows:

Definition 1.2 (Roger Vargas, Jr. et al., 2017) Leverage centrality is a measure of the relationship between the degree of a given node v and the degree of each of its

Corresponding author: sinumolsukumaran@gmail.com
Received: September 10, 2022, Accepted: November 15, 2022

neighbors v_i averaged over all neighbors N_v and is defined as:

$$l(v) = \frac{1}{\deg(v)} \sum_{v_i \in N_v} \frac{\deg(v) - \deg(v_i)}{\deg(v) + \deg(v_i)}$$

Definition 1.3 (Sunil Kumar R, Sinumol S, 2022) The leverage center of a graph G is defined as the set of nodes with the highest leverage centrality.

Definition 1.4 (Sunil Kumar R, Sinumol S, 2022) Bicentric leverage graphs are defined as those graphs with exactly two leverage centers.

Definition 1.5 A graph is said to be a tetra centric leverage graph if it has exactly four leverage centers.

Some Basic Propositions on Leverage Centrality

Proposition 1.1 (Roger Vargas, Jr. et al., 2017) Let G be a graph with n vertices. For any vertex v, $|l(v)| \leq 1 - \frac{2}{n}$. Furthermore, these bounds are tight in the cases of stars and complete graphs.

Proposition 1.2 (Roger Vargas, Jr. et al., 2017) For any graph G, $\sum_{v \in G} l(v) \leq 0$.

Theorem 1.1 (Roger Vargas, Jr. et al., 2017) In a graph G of order n, the maximum number of vertices with positive leverage centrality is $n - 1$.

Proposition 1.3 (Amogh Gupta et al., 2021) **G is a regular graph if and only if $l(v) = 0$** for every vertex $v \in G$.

RESULT AND DISCUSSIONS

In this section, the leverage centrality of the newly formed product graphs of path $P_n, n \geq 5$ with cycle $C_m, m \geq 3$ is studied under the classical graph products such as the cartesian, tensor, strong and the lexicographic products.

The Cartesian Product of Path with Cycle

Definition 2.1 (Richard Hammack, 2011) The Cartesian product of G and H is a graph, denoted as $G \square H$ and is defined as:

$$V(G \square H) = \{(g,h)/g \in V(G) \text{ and } h \in V(H)\}$$
$$E(G \square H) = \{(g,h)(g',h')/g = g', hh' \in E(H) \text{ or } g\,g' \in E(G), h = h'\}$$

Let the vertices of the path $P_n, n \geq 5$ be labeled as $\{0, 1, \ldots, n-1\}$. Before proving the first theorem, we have the following result on the leverage centralities of nodes in a path $P_n, n \geq 5$.

Theorem2.1 (Murat Ersen Berberler, 2020) Let $P_n, n \geq 5$ be a path of order n. Then, for $v \in P_n$,

$$l(v) = \begin{cases} \frac{-1}{3} & if\ v = 0, n-1 \\ \frac{1}{6} & if\ v = 1, n-2 \\ 0 & if\ 2 \leq v \leq n-3 \end{cases}$$

Thus, there are three distinct leverage centralities in a path which is a bicentric leverage tree. Let the vertices of the cycle $C_m, m \geq 3$ be labeled as $\{0, 1, \ldots, m-1\}$. Since the cycle is 2−regular, the leverage centrality is zero for each node. But we get interesting results when we combine cycle with the path through various graph products mentioned above. Now we state our first theorem as follows.

Theorem 2.2 In the cartesian product of path $P_n, n \geq 5$ with cycle $C_m, m \geq 3$, there are three distinct fixed leverage centralities.

Proof: Let $G = P_n \square C_m$, $n \geq 5, m \geq 3$. Then the product graph consists of nm vertices $\{(i,j) : i = \{0, \ldots, n-1\}$ and $j = \{0, \ldots, m-1\}\}$. Since the vertices 0 and $n-1$ are pendant vertices in the path P_n, the vertices $\{(i,j) : i = \{0, n-1\}$ and $j = \{0, \ldots, m-1\}\}$ are of degree three in the product $P_n \square C_m$ where $n \geq 5, m \geq 3$. In which, only one neighbor is of degree four and others are of degree three. Hence for these vertices

$$l(v) = \frac{1}{3}\left(\frac{3-4}{3+4}\right) = \frac{-1}{21}$$

Now consider the vertices $\{(i,j) : i = \{1, n-2\}$ and $j = \{0, \ldots, m-1\}\}$. These vertices are of degree four with one neighbor of degree three and others of degree four. Thus, for these vertices, we have

$$l(v) = \frac{1}{4}\left(\frac{4-3}{4+3}\right) = \frac{1}{28}$$

Finally, the remaining vertices are $\{(i,j): i = \{2,\dots,n-3\}$ and $j = \{0,\dots,m-1\}\}$. These vertices are of degree four, but in this case, all the neighbors are also of degree four. Hence $l(v) = 0$ for such vertices, which completes the proof.

Corollary 2.1 In $P_n \square C_m, n \geq 5, m \geq 3$, the leverage centrality of nodes is independent of the number of vertices in the component graphs.

The Tensor Product of Path with Cycle

Definition 2.2 (Richard Hammack, 2011) The tensor product of G and H is a graph, denoted as $G \times H$ and is defined as:

$$V(G \times H) = \{(g,h)/g \in V(G) \text{ and } h \in V(H)\}$$
$$E(G \times H) = \{(g,h)(g',h')/gg' \in E(G) \text{ and } hh' \in E(H)\}$$

Now we have the following theorem.

Theorem 2.3 The three distinct leverage centralities in the tensor product of path $P_n, n \geq 5$ with cycle $C_m, m \geq 3$ are the same centralities of the nodes of the path $P_n, n \geq 5$.

Proof: Let $G = P_n \times C_m$, $n \geq 5, m \geq 3$. The product graph consists of nm vertices $\{(i,j): i = \{0,\dots,n-1\}$ and $j = \{0,\dots,m-1\}\}$. In which, the degree two vertices are $\{(i,j): i = \{0, n-1\}$ and $j = \{0,\dots,m-1\}\}$. The neighbors of these vertices are of degree four and hence the leverage centrality is

$$l(v) = \left(\frac{2-4}{2+4}\right) = \frac{-1}{3}$$

Now for the vertices $\{(i,j): i = \{1, n-2\}$ and $j = \{0,\dots,m-1\}\}$, the degree is four and two neighbors are of degree two and others are of degree four. Thus, for these vertices, we have

$$l(v) = \frac{2}{4}\left(\frac{4-2}{4+2}\right) = \frac{1}{6}$$

Finally, for the remaining vertices $\{(i,j): i = \{2,\dots,n-3\}$ and $j = \{0,\dots,m-1\}\}$, the degree is four and all the neighbors are also of degree four. Hence $l(v) = 0$ for such vertices, which completes the proof.

The Strong Product of Path with Cycle

Definition 2.3 (Richard Hammack, 2011) The strong product of G and H is a graph, denoted as $G \boxtimes H$ and is defined as:

$$V(G \boxtimes H) = \{(g,h)/g \in V(G) \text{ and } h \in V(H)\}$$
$$E(G \boxtimes H) = E(G \square H) \cup E(G \times H)$$

Theorem 2.4 The three distinct leverage centralities in the strong product of path $P_n, n \geq 5$ with cycle $C_m, m \geq 3$ are $\frac{-9}{65}$, 0 and $\frac{9}{104}$.

Proof: Let $G = P_n \boxtimes C_m$, $n \geq 5, m \geq 3$. The product graph consists of nm vertices $\{(i,j): i = \{0,\dots,n-1\}$ and $j = \{0,\dots,m-1\}\}$. In G, the degree five vertices are $\{(i,j): i = \{0, n-1\}$ and $j = \{0,\dots,m-1\}\}$. For them, three neighbors are of degree eight and the remaining is of degree five itself. Hence for these vertices

$$l(v) = \frac{3}{5}\left(\frac{5-8}{5+8}\right) = \frac{-9}{65}$$

Again, for the vertices $\{(i,j): i = \{1, n-2\}$ and $j = \{0,\dots,m-1\}\}$, the degree is eight and five of their neighbors are of degree eight and others are of degree five. Thus, for these vertices, we have

$$l(v) = \frac{3}{8}\left(\frac{8-5}{8+5}\right) = \frac{9}{104}$$

For the remaining vertices $\{(i,j): i = \{2,\dots,n-3\}$ and $j = \{0,\dots,m-1\}\}$, degree is eight and all the neighbors are also of degree eight. Hence $l(v) = 0$ for such vertices, which completes the proof.

Corollary 2.2 In $P_n \boxtimes C_m$, $n \geq 5, m \geq 3$ the leverage centrality does not vary with the number of vertices in the path as well as the cycle.

The Lexicographic Product of Path with Cycle

Definition 2.4 (Richard Hammack, 2011) The lexicographic product of graphs G and H is the graph $G \circ H$ with

$$V(G \circ H) = \{(g,h)/g \in V(G) \text{ and } h \in V(H)\}$$
$$E(G \circ H) = \{(g,h)(g',h')/gg' \in E(G), or\ g = g'\ and\ hh' \in E(H)\}$$

We state our next theorem as follows.

Theorem 2.5 Let $G = P_n \circ C_m$, $n \geq 5, m \geq 3$. Then for $v = (i,j) \in G$

$$l(v) = \begin{cases} \frac{-m^2}{(m+2)(3m+4)} & if\ v = (i,j)\ with\ i = \{0, n-1\}\ and\ j = \{0,\dots,m-1\} \\ \frac{m^2}{(2m+2)(3m+4)} & if\ v = (i,j)\ with\ i = \{1, n-2\}\ and\ j = \{0,\dots,m-1\} \\ 0 & if\ v = (i,j)\ with\ i = \{2,\dots,n-3\}\ and\ j = \{0,\dots,m-1\} \end{cases}$$

Proof: Let $G = P_n \circ C_m$, $n \geq 5, m \geq 3$. Then the product graph consists of nm vertices $\{(i,j) : i = \{0,\dots,n-1\}$ and $j = \{0,\dots,m-1\}\}$. In which, $deg(i,j) = m+2$ for $i = \{0, n-1\}$ and $j = \{0,\dots,m-1\}$. Thus, there are $2m$ vertices with degree $m+2$. All the remaining vertices are of degree $2m+2$. The $2m$ vertices with degree $m+2$ have exactly two neighbors with degree $m+2$ and the other m neighbors are of degree $2m+2$. Thus $\forall v$ with $deg(v) = m+2$,

$$l(v) = \frac{m}{m+2}\left(\frac{m+2-(2m+2)}{m+2+2m+2}\right) = \frac{-m^2}{(m+2)(3m+4)}$$

Now consider the vertices with degree $2m+2$. Here the vertices (i,j) with $i = \{1, n-2\}$ and $j = \{0,\dots,m-1\}$ have only m neighbors with degree $m+2$ and others are of degree $2m+2$. Hence the leverage centrality of these vertices is

$$l(v) = \frac{m}{2m+2}\left(\frac{2m+2-(m+2)}{2m+2+m+2}\right) = \frac{m^2}{(2m+2)(3m+4)}$$

Finally, for the remaining degree $2m+2$ vertices (i,j) with $i = \{2,\dots,n-3\}$ and $j = \{0,\dots,m-1\}$, all of the neighbors are of degree $2m+2$ itself. Hence the leverage centrality of these vertices is $l(v) = 0$, which completes the proof.

The lexicographic product of graphs is not commutative. Therefore, we need to analyze the case of $G = C_m \circ P_n$ separately.

Theorem 2.6 Let $G = C_m \circ P_n, m \geq 3, n \geq 5$. Then for $v = (i,j) \in G$

$$l(v) = \begin{cases} \frac{2n-3}{2n+1}\left(\frac{-1}{4n+3}\right) & if\ v = (i,j)\ with\ i = \{0,\dots,m-1\}\ and\ j = \{0, n-1\} \\ \frac{5}{2(n+1)}\left(\frac{1}{4n+3}\right) & if\ v = (i,j)\ with\ i = \{0,\dots,m-1\}\ and\ j = \{1, n-2\} \\ \frac{2}{n+1}\left(\frac{1}{4n+3}\right) & if\ v = (i,j)\ with\ i = \{0,\dots,m-1\}\ and\ j = \{2,\dots,n-3\} \end{cases}$$

Proof: Let $G = C_m \circ P_n, m \geq 3, n \geq 5$. Then the product graph consists of mn vertices $\{(i,j) : i = \{0,\dots,m-1\}$ and $j = \{0,\dots,n-1\}\}$. In which $deg(i,j) = 2n+1$ for $i = \{0,\dots,m-1\}$ and $j = \{0, n-1\}$. Here there are only four neighbors with degree $2n+1$ itself. All the remaining $2n-3$ neighbors are of degree $2n+2$. Thus $\forall v$ with $deg(v) = 2n+1$,

$$l(v) = \frac{2n-3}{2n+1}\left(\frac{2n+1-(2n+2)}{2n+1+2n+2}\right) = \frac{2n-3}{2n+1}\left(\frac{-1}{4n+3}\right)$$

Now consider the vertices with degree $2n+2$. Here the vertices (i,j) with $i = \{0,\dots,m-1\}$ and $j = \{1, n-2\}$ have only five neighbors with degree $2n+1$ and others are of degree $2n+2$. Hence the leverage centrality of these vertices is

$$l(v) = \frac{5}{2n+2}\left(\frac{2n+2-(2n+1)}{2n+2+2n+1}\right) = \frac{5}{2(n+1)}\left(\frac{1}{4n+3}\right)$$

Finally, for the remaining degree $2n+2$ vertices (i,j) with $i = \{0,\dots,m-1\}$ and $j = \{2,\dots,n-3\}$, four neighbors are of degree $2n+1$ and the remaining are of degree $2n+2$ itself. Leverage centrality of these vertices is

$$l(v) = \frac{4}{2n+2}\left(\frac{2n+2-(2n+1)}{2n+2+2n+1}\right) = \frac{2}{n+1}\left(\frac{1}{4n+3}\right)$$

which completes the proof.

Corollary 2.3 As the number of vertices in the path increases, the leverage centralities of all the vertices of $G = C_m \circ P_n, m \geq 3, n \geq 5$ converges to 0.

Proof: $G = C_m \circ P_n, m \geq 3, n \geq 5$. From the theorem, for any n, the minimum leverage centrality of any vertex of G is

$$\min(l(v)) = \frac{2n-3}{2n+1}\left(\frac{-1}{4n+3}\right)$$

Similarly, for any n, the maximum leverage centrality of any vertex of G is

$$\max(l(v)) = \frac{5}{2(n+1)}\left(\frac{1}{4n+3}\right)$$

Therefore, for any vertex v in G, the leverage centrality is bounded as

$$\frac{2n-3}{2n+1}\left(\frac{-1}{4n+3}\right) \le l(v) \le \frac{5}{2(n+1)}\left(\frac{1}{4n+3}\right)$$

Thus as $n \to \infty$, we have

$$\lim_{n\to\infty} \frac{2n-3}{2n+1}\left(\frac{-1}{4n+3}\right) = \lim_{n\to\infty} \frac{5}{2(n+1)}\left(\frac{1}{4n+3}\right)$$

Hence

$$\lim_{n\to\infty} l(v) = 0$$

which completes the proof.

Leverage Centrality of vertices in Lexicographic Product of Paths

In this section, we are generalizing the leverage centrality of vertices in $P_n \circ P_n, n \geq 5$.

Theorem 3.1 The path graph $P_n, n \geq 5$ is a bicentric leverage graph with centers 1 and $n-2$ in the vertex labeling $\{0,1,\ldots,n-1\}$. But the composite graph $P_n \circ P_n$ for $n \geq 5$ is tetra centric with leverage centers (i,j) with $i,j = 1, n-2$.

Proof: The composite graph $P_n \circ P_n$ for $n \geq 5$ has n^2 vertices. They are $\{(i,j) : i = \{0,\ldots,n-1\}$ and $j = \{0,\ldots,n-1\}\}$. We can see only four distinct degrees in the composite graph: $n+1, n+2, 2n+1$ and $2n+2$. We need to analyze each case separately.

1. Degree $n+1$ vertices:

There are only four vertices $\{(i,j) : i = \{0, n-1\}$ and $j = \{0, n-1\}\}$ with degree $n+1$. They have one neighbor is of degree $n+2$, two neighbors are of degree $2n+1$ and the remaining $n-2$ neighbors are of degree $2n+2$. Therefore

$$l(v) = \frac{1}{n+1}\left(\frac{(n+1)-(n+2)}{(n+1)+(n+2)} + \left(\frac{(n+1)-(2n+1)}{(n+1)+(2n+1)}\right)2 + \left(\frac{(n+1)-(2n+2)}{(n+1)+(2n+2)}\right)n-2\right)$$
$$= \frac{1}{n+1}\left(\frac{-1}{2n+3} - \frac{2n}{3n+2} - \frac{n-2}{3}\right)$$

2. Degree $n+2$ vertices:

This case is further classified into two, depending upon the neighbor's degrees. Firstly, for the four vertices $\{(i,j) : i = \{0, n-1\}$ and $j = \{1, n-2\}\}$, one neighbor is of degree $n+1$, one neighbor is of degree $n+2$, two neighbors are of degree $2n+1$ and the remaining $n-2$ neighbors are of degree $2n+2$. Thus

$$l(v) = \frac{1}{n+2}\left(\frac{(n+2)-(n+1)}{(n+2)+(n+1)} + \left(\frac{(n+2)-(2n+1)}{(n+2)+(2n+1)}\right)2 + \left(\frac{(n+2)-(2n+2)}{(n+2)+(2n+2)}\right)n-2\right)$$
$$= \frac{1}{n+2}\left(\frac{1}{2n+3} - \frac{2(n-1)}{3(n+1)} - \frac{n(n-2)}{3n+4}\right)$$

Now consider the remaining degree $n+2$ vertices $\{(i,j) : i = \{0, n-1\}$ and $j = \{2,\ldots,n-3\}\}$. For them, two neighbors are of degree $n+2$ itself, two neighbors are of degree $2n+1$ and the remaining $n-2$ neighbors are of degree $2n+2$. Thus

$$l(v) = \frac{1}{n+2}\left(\left(\frac{(n+2)-(2n+1)}{(n+2)+(2n+1)}\right)2 + \left(\frac{(n+2)-(2n+2)}{(n+2)+(2n+2)}\right)(n-2)\right)$$
$$= \frac{1}{n+2}\left(\frac{-2(n-1)}{3(n+1)} - \frac{n(n-2)}{3n+4}\right)$$

3. Degree $2n+1$ vertices:

This case is also further classified into two, depending upon the neighbor's degrees. For the four vertices $\{(i,j) : i = \{1, n-2\}$ and $j = \{0, n-1\}\}$, two neighbors are of degree $n+1, n-2$ neighbors are of degree $n+2$, two neighbors are of degree $2n+1$ and the remaining $n-1$ neighbors are of degree $2n+2$. Hence

$$l(v) = \frac{1}{2n+1}\left(\left(\frac{(2n+1)-(n+1)}{(2n+1)+(n+1)}\right)2 + \left(\frac{(2n+1)-(n+2)}{(2n+1)+(n+2)}\right)(n-2) + \left(\frac{(2n+1)-(2n+2)}{(2n+1)+(2n+2)}\right)(n-1)\right)$$
$$= \frac{1}{2n+1}\left(\frac{2n}{3n+2} - \frac{(n-1)(n-2)}{3(n+1)} - \frac{(n-1)}{4n+3}\right)$$

Now consider the remaining degree $2n+1$ vertices $\{(i,j) : i = \{2,\ldots,n-3\}$ and $j = \{0, n-1\}\}$. In this case, four neighbors are of degree $2n+1$ itself and the remaining $2n-3$ neighbors are of degree $2n+2$. Thus

$$l(v) = \frac{1}{2n+1}\left(\left(\frac{(2n+1)-(2n+2)}{(2n+1)+(2n+2)}\right)(2n-3)\right) = \frac{1}{2n+1}\left(-\frac{(2n-3)}{4n+3}\right)$$

4. Degree $2n+2$ vertices:

Here there are four cases to analyze depending upon the neighbor's degrees. Consider the vertices $\{(i,j): i = \{2,\dots,n-3\}$ and $j = \{2,\dots,n-3\}\}$. For the above vertices, four neighbors are of degree $2n+1$ and the remaining $2n-2$ neighbors are of degree $2n+2$. Hence

$$l(v) = \frac{4}{2n+2}\left(\frac{(2n+2)-(2n+1)}{(2n+2)+(2n+1)}\right) = \frac{2}{(n+1)(4n+3)}$$

Now consider the vertices $\{(i,j): i = \{2,\dots,n-3\}$ and $j = \{1,n-2\}\}$. Here five neighbors are of degree $2n+1$ and the remaining $2n-3$ neighbors are of degree $2n+2$. Thus

$$l(v) = \frac{5}{2n+2}\left(\frac{(2n+2)-(2n+1)}{(2n+2)+(2n+1)}\right) = \frac{5}{2(n+1)(4n+3)}$$

Again for the four vertices $\{(i,j): i = \{1,n-2\}$ and $j = \{1,n-2\}\}$, two neighbors are of degree $n+1, n-2$ neighbors are of degree $n+2$, three neighbors are of degree $2n+1$ and the remaining $n-1$ neighbors are of degree $2n+2$. Thus

$$l(v) = \frac{1}{2n+2}\left(\left(\frac{(2n+2)-(n+1)}{(2n+2)+(n+1)}\right)2 + \left(\frac{(2n+2)-(n+2)}{(2n+2)+(n+2)}\right)(n-2) + \left(\frac{(2n+2)-(2n+1)}{(2n+2)+(2n+1)}\right)3\right)$$
$$= \frac{1}{2(n+1)}\left(\frac{2}{3} + \frac{n(n-2)}{3n+4} + \frac{3}{4n+3}\right)$$

Finally, consider the vertices $\{(i,j): i = \{1,n-2\}$ and $j = \{2,\dots,n-3\}\}$. For them, two neighbors are of degree $n+1, n-2$ neighbors are of degree $n+2$, two neighbors are of degree $2n+1$ and the remaining n neighbors are of degree $2n+2$. Thus

$$l(v) = \frac{1}{2n+2}\left(\left(\frac{(2n+2)-(n+1)}{(2n+2)+(n+1)}\right)2 + \left(\frac{(2n+2)-(n+2)}{(2n+2)+(n+2)}\right)(n-2) + \left(\frac{(2n+2)-(2n+1)}{(2n+2)+(2n+1)}\right)2\right)$$
$$= \frac{1}{2(n+1)}\left(\frac{2}{3} + \frac{n(n-2)}{3n+4} + \frac{2}{4n+3}\right)$$

From the above-detailed analysis, we found that

$$l(v) = \frac{1}{2(n+1)}\left(\frac{2}{3} + \frac{n(n-2)}{3n+4} + \frac{3}{4n+3}\right)$$

is the largest value among all other leverage centralities for any $n \geq 5$. The corresponding four vertices $(i,j): i = \{1,n-2\}$ and $j = \{1,n-2\}$ are the leverage centers for the composite graph $P_n \circ P_n$ for $n \geq 5$, which completes the proof.

Leverage Centrality of vertices in Corona Product of Paths

The corona operation duplicates the second graph by the cardinality of the first graph and connects each copy to each corresponding point in the first graph (T I Haryadi and LSusilowati, 2021). The corona product $G \odot H$ of two graphs G and H is defined as follows (Zahra Yarahmadia et al., 2012):

Definition 4.1 The corona product $G \odot H$ of two graphs G and H is defined as the graph obtained by taking one copy of G and $|V(G)|$ copies of H and joining the i^{th}vertex of G to every vertex in the i^{th}copy of H.

Remark 4.1 (Zahra Yarahmadia et al., 2012) If $|V(G)| = n$ and $|E(G)| = q$, we say that G is an (n,q) graph. If G is an (n,q) graph and H is an (m,q') graph, then $|V(G \odot H)| = n + nm$ and $|E(G \odot H)| = q + nq' + nm$. The i^{th}copy of H is denoted by H_i, $1 \leq i \leq n$.

Remark 4.2 In this section, the vertices of the graph G of order n be labeled as $\{u_1 u_2, \dots, u_n\}$ and that of the graph H of order m be labeled as $\{v_1 v_2, \dots, v_m\}$. In the graph $G \odot H$, the vertex v_k in H_i is denoted by $v_{i,k}$, $1 \leq i \leq n$ and $1 \leq k \leq m$.

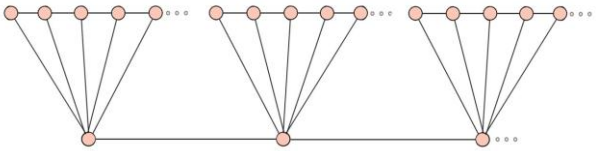

Figure 1: Corona product $P_n \odot P_m$

Theorem 4.1 Let $G = P_n$ and $H = P_m$ where $n, m \geq 5$ and $n \leq m$ or $n \geq m$. In the corona product $G \odot H$, all the vertices $v_{1,k}$ in the copy H_1 have the same leverage with the corresponding vertices $v_{n,k}$ in the copy H_n where $1 \leq k \leq m$. Furthermore, the corresponding vertices in the remaining copies H_i, $2 \leq i \leq n-1$ have the same leverage. Also, $G \odot H$ is a bicentric leverage graph with u_2 and u_{n-1} as leverage centers.

Proof: Let the vertices of the graph $G = P_n$ be labeled as $\{u_1 u_2, \dots, u_n\}$ and that of the graph $H = P_m$ be labeled as $\{v_1 v_2, \dots, v_m\}$ where $n \leq m$ or $n \geq m$. Then the corona graph $G \odot H$ consists of $n + nm$ vertices. In this, $deg(u_i) = m + 1$ for $i = 1, n$ and for $2 \leq i \leq n - 1$, $deg(u_i) = m + 2$. Now we find the leverage centralities of each of them. The leverage centrality $l(u_i)$ for $i = 1, n$ is

$$l(u_i) = \frac{1}{m+1}\left(\frac{(m+1)-(m+2)}{(m+1)+(m+2)} + \left(\frac{m+1-2}{m+1+2}\right)2 + \left(\frac{m+1-3}{m+1+3}\right)(m-2)\right)$$
$$= \frac{1}{m+1}\left(\frac{-1}{2m+3} + \frac{2(m-1)}{m+3} + \frac{(m-2)^2}{m+4}\right)$$

The leverage centrality $l(u_i)$ for $i = 2, n - 1$ is

$$l(u_i) = \frac{1}{m+2}\left(\frac{(m+2)-(m+1)}{(m+2)+(m+1)} + \left(\frac{m+2-2}{m+2+2}\right)2 + \left(\frac{m+2-3}{m+2+3}\right)(m-2)\right)$$
$$= \frac{1}{m+2}\left(\frac{1}{2m+3} + \frac{2m}{m+4} + \frac{(m-2)(m-1)}{m+5}\right)$$

The leverage centrality $l(u_i)$ for $3 \leq i \leq n - 2$ is

$$l(u_i) = \frac{1}{m+2}\left(\left(\frac{m+2-2}{m+2+2}\right)2 + \left(\frac{m+2-3}{m+2+3}\right)(m-2)\right)$$
$$= \frac{1}{m+2}\left(\frac{2m}{m+4} + \frac{(m-2)(m-1)}{m+5}\right)$$

Finally, we consider the leverage centralities of the vertices in the copies H_i, $1 \leq i \leq n$. Here $deg(v_{i,k}) = 2$ for $1 \leq i \leq n$ and $k = 1, m$. Also, $deg(v_{i,k}) = 3$ for $1 \leq i \leq n$ and $2 \leq k \leq m - 1$.

The leverage centrality $l(v_{i,k})$ for $i = 1, n$ and $k = 1, m$ is

$$l(v_{i,k}) = \frac{1}{2}\left(\frac{2-3}{5} + \frac{2-(m+1)}{2+(m+1)}\right) = \frac{1}{2}\left(\frac{-1}{5} - \frac{m-1}{m+3}\right)$$

The leverage centrality $l(v_{i,k})$ for $i = 1, n$ and $k = 2, m - 1$ is

$$l(v_{i,k}) = \frac{1}{3}\left(\frac{3-2}{5} + \frac{3-(m+1)}{3+(m+1)}\right) = \frac{1}{3}\left(\frac{1}{5} - \frac{m-2}{m+4}\right)$$

The leverage centrality $l(v_{i,k})$ for $i = 1, n$ and $3 \leq k \leq m - 2$ is

$$l(v_{i,k}) = \frac{1}{3}\left(\frac{3-(m+1)}{3+(m+1)}\right) = \frac{1}{3}\left(-\frac{m-2}{m+4}\right)$$

The leverage centrality $l(v_{i,k})$ for $2 \leq i \leq n - 1$ and $k = 1, m$ is

$$l(v_{i,k}) = \frac{1}{2}\left(\frac{2-3}{5} + \frac{2-(m+2)}{2+(m+2)}\right) = \frac{1}{2}\left(\frac{-1}{5} - \frac{m}{m+4}\right)$$

The leverage centrality $l(v_{i,k})$ for $2 \leq i \leq n - 1$ and $k = 2, m - 1$ is

$$l(v_{i,k}) = \frac{1}{3}\left(\frac{3-2}{5} + \frac{3-(m+2)}{3+(m+2)}\right) = \frac{1}{3}\left(\frac{1}{5} - \frac{m-1}{m+5}\right)$$

The leverage centrality $l(v_{i,k})$ for $2 \leq i \leq n - 1$ and $3 \leq k \leq m - 2$ is

$$l(v_{i,k}) = \frac{1}{3}\left(\frac{3-(m+2)}{3+(m+2)}\right) = \frac{1}{3}\left(-\frac{m-1}{m+5}\right)$$

Thus, for a given m and n, $l(u_i)$ for $i = 2, n - 1$ is the maximum among the leverage centralities of all other vertices. Thus $G \odot H$ is a bicentric leverage graph, which completes the proof.

CONCLUSION

The leverage centrality analysis of vertices in $P_n \square C_m$, $P_n \times C_m$, $P_n \boxtimes C_m$, $P_n \circ C_m$ and $C_m \circ P_n$ for $n \geq 5, m \geq 3$ are done. We found that for the first three products leverage is independent of the number of vertices in the component graphs and for the remaining, it is dependent on m and n respectively. The leverage centrality analysis of vertices in the lexicographic and the corona product of paths are also investigated and found that in the lexicographic product, the composition of two paths is a tetra centric leverage graph, even though it is bicentric in the corona product. In each case, the number of distinct leverage centralities are also identified. This study can be extended to other graph operations.

ACKNOWLEDGEMENT

Our thanks go out to an anonymous referee who provided helpful feedback.

References

Amogh Gupta, Harish Balaji, Sundareswaran R, Mahesh V, Geetanjali B. 2021. Group Leverage Centrality and its Application in Brain

Networks. IOP Conf. Ser.: Mater. Sci. Eng. (1187).1-9.

Haryadi T. I. and Susilowati L. 2021. Betweenness centrality in corona product of K_n and C_m graph, J. Phys. Conf. Ser.1494012017.

Joyce K. E., Laurienti P. J, Burdette J. H., and Hayasaka S. 2010. A New Measure of Centrality for Brain Networks, PLOS ONE 5:8, art. id. e12200.

Murat Ersen Berberler. 2020. Leverage Centrality Analysis of Infrastructure Networks, WILEY. 767-781.

Narsingh Deo. 2014. Graph Theory with Applications to Engineering and Computer Science, PHI Learning Pvt. Ltd. Delhi-110092.

Richard Hammack, Wilfried Imrich and Sandi Klavzar. 2011. Handbook of Product Graphs, 2nd ed., CRC Press, Taylor &Francis Group, LLC.

Roger Vargas Jr, Abigail Waldron, Anika Sharma, Rigoberto Fl´orez and Darren A. Narayan. 2017. A Graph Theoretic Analysis of Leverage Centrality. AKCE Int. J. Graphs Comb. 295-306.

Roger Vargas Jr., Abigail Waldron, Anika Sharma, Rigoberto Fl´orez and Darren A. Narayan. 2017. Leverage centrality of knight's graphs and Cartesian products of regular graphs and path powers. INVOLVE 10(4), 583-592.

Sharma A., Vargas R., Waldron A., Florez R., and Narayan D. A. 2017. Leverage centrality of graphs, preprint.

Sunil Kumar R, Sinumol S. 2022. Leverage Center of Some Graphs, arxive: submit/4471796 [math.co].

Zahra Yarahmadia, Ali Reza Ashraf. 2012. The Szeged, vertex PI, first and second Zagreb indices of corona product of graphs. Faculty of Sci. and Math., University of Nis, Serbia, Filomat 26:3, 467–472.

COUPLING BETWEEN LOWER ATMOSPHERE AND IONOSPHERE DURING SUPER CYCLONE "AMPHAN" USING COSMIC SATELLITE-A CASE STUDY

Gopal Mondal
Department of Mathematics, Vivekananda Mission Mahavidyalaya, Haldia, Purba Medinipur, 721645, India

ABSTRACT

The coupling between the lower atmosphere and ionosphere during the super cyclone "AMPHAN" has been studied using COSMIC-RO satellite observation. Sea Surface Temperature (SST) and Outgoing Long-wave Radiation (OLR) information for the 45-day observational period have also been analyzed in this study. Both the SST and OLR exhibit sensible variation during different stages of the cyclone. At Ionospheric height, Electron (Ne) concentration shows significant variability during the pre as well as post-cyclonic period. During the mature stage of a cyclone drastic fall in electron content, specifically in the bottom side ionosphere, indicates a sharp fall in Ne concentration throughout the F region to the lower ionosphere, which could be considered as the major ionospheric signature during an active cyclone in lower atmosphere. In E-layer electron content shows a more prominent signature not only during the pre and post-cyclonic period but also during the mature stage of the cyclone.

KEYWORDS: Amphan, Ionosphere, COSMIC-RO, AGW-TID

INTRODUCTION

It is well known that the Earth's Atmosphere is extremely dynamic. In this regard, the geographically equatorial region is highly dominant over the remaining part of the Globe, and our country (India) is almost totally included in this region where a maximum of the lower atmospheric hazards occur. Due to Global warming, the Sea Surface Temperature (SST) in most parts of the World's oceans is sensitively increasing, which helps to initiate the formation of the low-pressure system over the water body. Each year, a large number of Cyclonic Storm (CS) activities are generated over the Bay of Bengal (BOB) region, as the temperature of this region is mostly favorable to generate it. In this connection, it should be mentioned that in 1948 Erik Palmen first observed that the Tropical Cyclone (TC) requires an ocean temperature of at least 80°F (26.5°C) for its formation and growth. Above this temperature, deep convection can occur, but below this, the atmosphere is too stable and no thunderstorm activity could be found (Graham and Barnett, 1987). Recently, in the equatorial region, an increasing trend in cyclone intensity and its lifecycle (Elsner *et al.*, 2008, Park *et al.,* 2014) encourages the research community to estimate its evolution in signature not only in the horizontal direction but also to the vertical extending up to the Ionosphere (Abramovich *et al.,* 2008; Lin 2012a, 2012b; Polyakova and Perevalova, 2011, 2013; Tian *et al.,* 2010) where concentration of charged particle is a key element (Lee and Reinisch, 2006) and mainly controlled by state of the sun (Liu *et al.,* 2006; Sripathi, 2012)**.** Vertically all the Atmospheric layers including the Ionosphere have crucial relationships with each other and the convective phenomenon or thermal-misbalance activity in the lower atmosphere indirectly persists in density and pressure change in the ambient atmosphere causing the generation of Atmospheric Gravity Wave (AGW) (Eun and Gross, 1976; Fritts *et al.,* 2008; Kazimirovsky, 2002) and then can move through the upper troposphere via stratosphere to mesospheric and ionospheric heights (Killeen and Johnson, 1995, Mondal *et al.,* 2017). In previous reports (Vincent, 2007; Vlasov *et al.,* 2011; Yigit, and Medvedev, 2015) different characteristic of AGWs was deeply studied. Recently it was reported (Hoffmann *et al.,* 2018; Nolan and Zhang, 2017) that the cyclone intensity and amplitude of AGWs at stratospheric heights are well correlated. Nina and his team 2017 studied 70 cyclones using VLF signals to find out their effect on the ionosphere and found ionospheric responses in most of the cases in which prominent signatures were detected during the depression state of the convective phenomena which converted to hurricanes later. Recognizing these irregularities, if any, occurred in the ionosphere during different convective events, has been crucial for better interpreting the coupling mechanism in Earth's atmospheric observations, under-

Corresponding author: gopalmondal18@gmail.com
Received: September 10, 2022, Accepted: November 15, 2022

standing the Earth's climate system, and developing forecast capabilities.

The Super Cyclonic Storm (SuCS) "AMPHAN" was the first SuCS over the BOB, after Odisha in 1999. It originated from the remnant of a low-pressure area that occurred over the south Andaman Sea and adjoining southeast BOB on 13th May. After its concentration into depression (D) and further intensification to Deep Depression (DD) in the afternoon, it moved north-north-westwards and again intensified into a Cyclonic Storm over southeast BOB in the evening of 16 May 2020. Moving slightly northward further intensified into a Severe Cyclonic Storm(SCS) over southeast BOB on the morning of 17th May. Again, after rapid intensification, during the afternoon period of the 17th, it became an Extremely Severe Cyclonic Storm (ESCS) in the early hours of the 18th and finally reached the SuCS state around noon of the 18th of May. Thereafter it weakened slightly and crossed the west Bengal-Bangladesh coasts as a Very Severe Cyclonic Storm (VSCS) across the Sundarbans during 1530-1730 IST, 20th May, with a maximum sustained wind speed of 155-165kmph. It moved very close to Kolkata during the late evening to night on 20th May with heavy wind and rain. A detailed description of its track and intensity was obtained from https://mausam.imd.gov.in/Forecast/marquee_data/indian111.pdf.

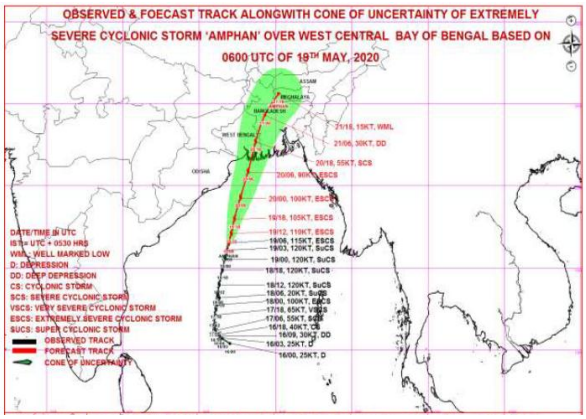

Figure 1: Track and intensity of SuSC amphan over BOB from 16th to 21st May 2020 (Adopted from https://mausam.imd.gov.in/Forecast/marquee_data/indian111.pdf)

MATERIAL AND METHOD OF ANALYSIS

All information about the super cyclone amphan including its track, intensity, lifecycle, etc. was obtained from the Indian Meteorological Department (IMD) website (http://www.imd.gov.in/). The OLR and SST are valuable parameters that provide sensitive information about convictive activities, like a thunderstorm, cyclones, etc. For this study daily mean OLR and SST over the selected region, were taken from the NOAA website (http://www.esrl.noaa.gov/psd/data/gridded). For ionospheric information, COSMIC-RO satellite data have been downloaded from the mission website (http://www.cosmic.ucar.edu). Also, the solar flux variability (Liu *et al.*, 2006) and Earth's geomagnetic (Dabas *et al.*, 1980) condition during the respective observational periods were checked by the variations of the solar F10.7 flux and geomagnetic $\sum$Kp indices information, obtained from the websites (http://www.ukssdc.ac.uk) of UKSSDC, UK and (http://wdc.kugi.kyoto-u.ac.jp) of Kyoto, Japan. Like other studies (Sripathi, 2012; Mondal *et al.*, 2017) some precise restrictions have been imposed to filter out suitable data sets for better quality and applicability of this study. As the COSMIC satellite is a Low Earth Orbiting (LEO) Satellite completing one rotation around Earth in 100 minutes (Aragon-Angel *et al.*, 2009) to detect any variability in the atmosphere over a fixed location continuously for a few days, data of those orbits have been considered which passes through a 15^{O} box size region covering the track of cyclone. Also, those data profiles have been considered that were associated with $F10.7 \le 150$ you and/or $\sum Kp \le 30$. Finally, 838 Vertical Electron Density (VED) profiles for the selected 45-day observational periods have been filtered out for analysis.

The Integrated Electron Contents (IECs, equivalent to TEC) have been calculated using the following equation:

$$(BIEC, TIEC) = \int_{(Balt, HmF2)}^{(HmF2, Talt)} Ne(z)dz \qquad (1)$$

In the above equation (Eq. 1), Balt and Talt are the Mean Sea Level Altitude (MSL_Alt) at the bottom and top point of the bottom and topside Ionosphere respectively. Finally, the daily weighted mean of each ionospheric parameter has been calculated using equation (2) to minimize the diurnal effect in the irregular variability, if any, at ionospheric height. For this purpose, each day (i.e. 24 hours) is divided into

four equal-length (six hours) sub-intervals: $0 \leq LT < 6$, $6 \leq LT < 12$, $12 \leq LT < 18$, and $18 \leq LT < 24$, and thereafter all the parameters associated to these four sub-intervals have been assigned the weights; 4, 3, 2 and 1 respectively.

$$P(\text{ave}) = \frac{(4N_4P+3N_3P+2N_2P+N_1P)}{(4N_4+3N_3+2N_2+N_1)} \quad (2)$$

RESULT AND DISCUSSIONS

OLR AND SST VARIATION

Figure 2 shows the variability in OLR during the 45-day observational period including the lifecycle of the catastrophic super cyclone, amphan over the BOB. Here daily averaged OLR values were plotted. Generally, OLR provides sensitive information about convective activities, like thunderstorms, cyclones, etc. not only over the land but also over the ocean. However, in this case, during the incipient stage of the low-pressure systems across 15th May 2020 the OLR values primarily started decreasing (see Figure 2) which might be due to the initial trend of increasing cloud amount in the lower atmosphere. After five days of depleting, the OLR value achieved its lowest level (nearly 149) on the 20th of May when the low-pressure system reached its peak intensity just before the precipitation. After that, the OLR values sharply increased and attained their normal level near 260-270 W m^{-2} in the post-cyclone genesis period when the cloud amount in the troposphere was gradually decreasing day by day.

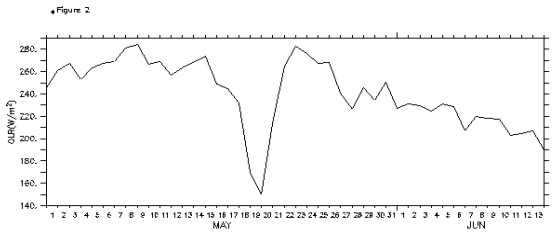

Figure 2: Daily mean variation in OLR over BOB during 45 (1st May-14th June 2020) days observational period.

For SST (see figure 3), the steady higher concentration across 13-14th May 2020, indirectly initiated the formation of the low-pressure system over the BOB region. After that, from 15-17 May, the temperature at the sea surface maintains a certain higher level which helps the low-pressure system to be further intensified gradually achieving its peak level on 18-19 May. Finally, on 20th May, this dynamic system entered the land with great wind and heavy rainfall in the coastal area of BOB causing huge damages, and during this period SST fell drastically. After that, the temperature at the sea surface maintains a steady lower level for the next few days which is markedly different from the OLR. One significant difference in variability between SST and OLR depicted here is that during the period when SST maintains the higher level concentration, OLR continuously depletes with the gradual intensification of the low-pressure system, and after landfall, this phenomenon is the opposite which attributes that OLR and SST are anti-correlated during the whole lifecycle of the low-pressure system.

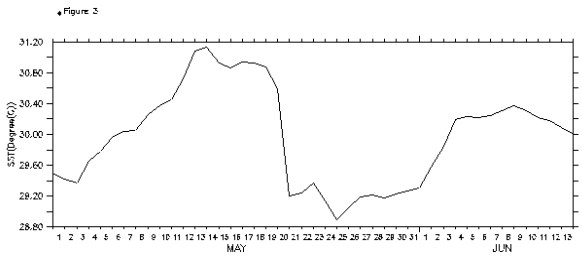

Figure 3: Daily mean variation in SST over BOB during 45 (1st May-14th June 2020) days observational period.

VARIATION IN IONOSPHERIC PARAMETERS

In Figure 4(a-d) weighted average values of ionospheric parameters (NmF2, HmF2. BTEC, and TTEC) were depicted for the 45-day observational period including the life cycle of super cyclone amphan. Observing four panels in this figure, it is clear that NmF2 and TTEC were highly correlated to each other compared to BTEC throughout the observational period. Again, till the 17th of May, TTEC and BTEC showed almost similar behavior, and thereafter these two parameters along with NmF2 continuously declined up to the 21st to 22nd of May when the HmF2 sustained at a higher level. On the other hand, in the lower atmosphere, during the first phase of the cyclone formation i.e. between the 15th to 17th of May the cloud amount in the troposphere increased (shown in Figure 2) gradually due to excessively high SST (shown in figure 3) near the place of origin of the low-pressure system in BOB and transforming to depression, a considerable rise in electron concentration throughout the bottom side ionosphere along with top side F2 layer help to achieve

higher NmF2, BTEC and TTEC. This particular ionospheric signature might be considered as the pre-cyclonic variability in the ionosphere during active depression in the lower atmosphere which is consistent with the findings of the study Nina *et al.,* 2017. During the period 18th to 21st May which covers the mature stage to landfall of the cyclone, as the Ne concentration in the bottom side ionosphere continuously falls, the level of NmF2 also falls, resulting in HmF2 to be shifted at the higher altitude which in turn reduces the thickness of top-side ionosphere slightly and hence affect the magnitude of TTEC (shown in figure 4(c-d)). These phenomena could be considered as the effect of perturbation in the lower atmosphere during the active cyclone. After landfall, steady ionization by sunlight in the F layer of the ionosphere during the next 3-4 days slowly gears up the level of the electron concentration, resulting rise in TEC level in both the bottom and top side ionosphere while the height of peak electron concentration (i.e. HmF2) remains essentially at the same level for 2-3 days.

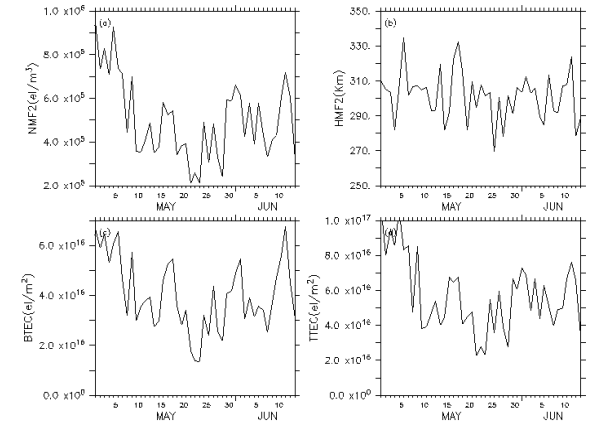

Figure 4: Variation in peak ionospheric parameters (NmF2 and HmF2) and TECs (BTEC and TTEC)

VARIATION IN DIFFERENT LAYERS

In Figure 5, TECs associated with different sub-intervals of 50 km height were plotted to identify the region or layer where maximum perturbation was encountered during different stages of the low-pressure system. From 15th to 17th May, the electron content in every layer of the ionosphere was significantly very high, during which the temperature on the sea surface (i.e. SST, shown in figure 3) also maintained higher concentration and the amount of OLR (shown in figure 2) concentration indicated the increasing presence of clouds amount in the lower atmosphere i.e. depression stage, mostly agreed with Nina *et al.,* 2017. This event is followed by a prolonged TEC drop in all layers till 20th May, specifically in the denser region, which can then be interpreted as a signature during the active cyclone and in post-cyclonic periods this trend of lower concentration of electron content sustained for the next 3-4 days (21st -25th May). As no unusual solar activity and geomagnetic activity have been reported during the observational period, this irregular variability in TECs across the cyclone genesis period have a sensitive connection with the lower atmospheric disturbance arises due to the thermal misbalance triggering so many physical as well as chemical changes in atmospheric layers due to lightning, convection current, thunderstorms, strong electric fields between the clouds (Bhattacharya and Das, 2013), air-sea interactions (Das *et al.,* 2021; Lastovicka, 2006; Guha *et al.,* 2016).

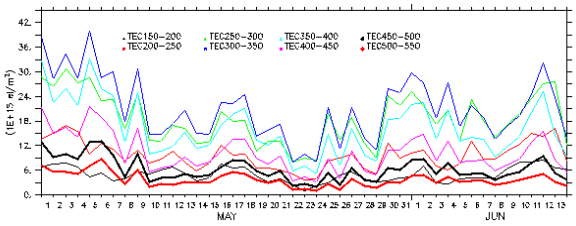

Figure 5: TEC variation in different sub-intervals of 50 km height, during 45 (1st May-14th June 2020) days observational period

Figure 6 shows the electron content variation during the 45-day observational period (1st May to 14th June 2020) particularly at the E layer. Across 15-17th May in this layer, the trend of getting higher electron concentration is more prominent when the cyclone was in the depression stage in the troposphere and this particular pre-cyclonic signature in the E-layer might be due to lower atmospheric forcing during the depression stage (Nina *et al.,* 2017) of the low-pressure system. Then the electron content (i.e. ETEC) starts to fall and reaches its lowest level on the 23rd, which covers the mature to post-cyclonic period whereas, the other layer above it maintains a steady level of TEC for 2-3 days (shown in figure 5) which is a major difference in TEC concentration in the post cyclonic period. Finally, a quick restoration to normalcy has also been observed which is much more prominent as compared to other layers. This interesting phenomenon is attributed to the

effect of lower atmospheric forcing in the lower ionosphere, matching the report by Das *et al.*, (2021).

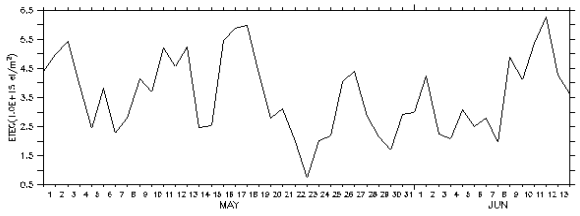

Figure 6: Variations in E layer Total Electron Content during 45 (1st May-14th June 2020) days observational period.

CONCLUSIONS

Here to study the ionospheric variation during the Amphan super cyclone over the BOB region, COSMIC-RO satellite information has been used with other two important atmospheric parameters, SST and OLR. This type of study using LEO satellite data with SST and OLR information over this region has not been done recently. From the above result and discussion, it is clear that during active low pressure as well as during pre and post-cyclonic periods, different layers, especially the E layer and denser ionospheric layer showed noticeable irregular variability. This coupling between different layers of the atmosphere during an active cyclone in the lower atmosphere redistributes the energy and momentum among them. The results are summarised in the following order:

1. Atmospheric parameters, SST, and OLR both showed significant variability during different stages of the cyclone (shown in Figure 2 and Figure 3).
2. Peak parameters, NmF2 as well as HmF2 show clear pre and post-cyclonic signatures.
3. During the period when the low-pressure system initially was in the depression stage, a higher concentration of Ne throughout the ionosphere is an important pre-cyclonic signature.
4. During the mature stage to landfall, major depletion in TEC values could be attributed to the effect of an active cyclone in the lower atmosphere.
5. The ionospheric E layer exhibits significant Pre and post cyclonic signature (shown in Figure 6) partially agrees with the study of Nina *et al.,* 2017 and Das *et al.*, 2021.

ACKNOWLEDGMENTS

COSMIC satellite data were downloaded from the website http://www.cosmic.ucar.edu. Cyclone-related information has been taken from the IMD website http://www.imd.gov.in/. The author would like to thank WDC Geomagnetic Data Centre, Kyoto University, Japan for providing geomagnetic indices and UKSSDC, UK for providing F10.7 cm solar flux data. The author would also like to acknowledge the reviewers for their earnest comments.

REFERENCES

Abramovich E. L., S. V. Voeykov, A. B. Ishin, N. P. Perevalova, and Y. A. Ruzhin, 2008. Variations in the total electron content during the powerful typhoon of August 5-11, 2006, near the southeastern coast of China, Geomagn. Aeron. 48 (5), 674-679, doi:10.1134/ S0016793208050113.

Aragon-Angel A., M. Hemandez-Pajares, J. M. Juan, and J. Sanz, 2009. Obtaining more accurate electron density profiles from bending angle with GPS occultation data: FORMOSAT-3/COSMIC constellation, Adv. Space Res. 43, 1694–1701 doi:10.1016/j.asr.2008. 10.034.

Bhattacharya B. and T. Das, 2013. Tropospheric-Ionospheric Coupling by Electrical Processes of the Atmosphere. International Journal of Application or Innovation in Engineering & Management (IJAIEM), 2(5) 324-336, Retrieved from http://www.ijaiem.org/ Volume2Issue5/IJAIEM-2013-05-30-086.pdf.

Dabas, R. S., J. B. Lal, T. R.Tyagi, and Y. V. Somayajulu, 1980. Variations in TEC and other parameters associated with magnetic storms, Indian J. Radio & Space Phys. 9, 1-6, http://nopr.niscair.res.in/ handle/1234567 89/36936.

Das, B., A Sen, S Pal, and P K Haldar, 2021. Response of the Sub-Ionospheric VLF Signals to the Super Cyclonic Storm Amphan: First Observation from Indian Subcontinent, J. Atmos. and Solar-Terrestrial Phy. 220(1), 105668 https://doi.org/10.1016/j.jastp.2021. 105668.

Elsner, J. B., J. P. Kossin and T. H. Jagger, 2008. The increasing intensity of the strongest tropical cyclones. NATURE 455(4), doi: 10.1038/nature07234.

Eun, H and S. H. Gross, 1976. Ionospheric Disturbances and Gravity Waves. J. Geophysical. Res. 81(19), https://inis.iaea.org/search/search.aspx?orig_q=RN:8286655.

Fritts, D. C., S. L. Vadas, D. M. Riggin, M. A. Abdu, I. S. Batista, H. Takahashi, A. Medeiros, F. Kamalabadi, H. L. Liu, B. G. Fejer, and M. J Taylor, 2008. Gravity wave and tidal influences equatorial spread F based on observations during the Spread F Experiment (SpreadFEx); Ann.Geophys. 26, 3235–3252, doi:10.5194/angeo-26-3235-2008.

Graham N. E. and T. P. Barnett, 1987. Sea Surface Temperature, Surface Wind Divergence, and Convection over Tropical Oceans, Science, 238(4827), 657-659, doi: 10.1126/science.238.4827.65.

Guha A., B. Paul, M. Chakraborty, B. K. De, 2016. Tropical cyclone effects on the equatorial ionosphere: First result from the Indian sector, J. Geophysical Res. 121(6), 5764-5777, https://doi.org/10.1002/2016JA02 2363

Hoffmann, L., X. Wu, and M. J. Alexander, 2018. Satellite Observations of Stratospheric Gravity Waves Associated With the Intensification of Tropical Cyclones. Geophysical Research Letters 45 1692-1700, https://doi.org/10.1002/2017GL076123.

Kazimirovsky, E.S., 2002. Coupling from below as a source of ionospheric variability: a review. Ann. Geophys. 45(1), 1-29, http://dx.doi.org/10.4401/ag-3482.

Killeen, T. L., and R. M. Johnson, 1995. Upper atmospheric waves, turbulence, and winds: Importance for mesospheric and thermospheric studies. Review of Geophysics 33(S1), 737–744, doi: 10.1029/95RG00408.

Lastovicka, J. 2006. Forcing of the ionosphere by waves from below. J. Atmos. Sol.-Terr. Phys. 68, 479–497, http://doi.org/10.1016/j.jastp.2005.01.018.

Lee, C. C. and B. W. Reinisch, 2006. Quiet-condition hmF2, NmF2, and B0 variations at Jicamarca and comparison with IRI-2001 during solar maximum. J. Atmos. and Solar-Terr. Phys., 68, 2138–2146, http://doi.org/10.1016/j. jastp.2006.07.007.

Lin, J. W. 2012a. Ionospheric total electron content anomalies due to Typhoon Nakri on 29 May 2008: A nonlinear principal component analysis. Computers and Geosciences, 46, 189-195, doi:10.1016/j.cageo.2011.12.007.

Lin, J. W. 2012b, Study of ionospheric anomalies due to impact of typhoon using Principal Component Analysis and image processing. J. Earth Sys. Sci. 121 (4), 1001-1010, Doi: 10.1007/s 12040-012-0214-6.

Liu, J. Y., C. H. Lin, Y. I. Chen, Y. C. Lin, T. W. Fang, C. H. Chen, Y. C. Chen, and J. J. Hwang, 2006. Solar flare signature of the ionospheric GPS total electron content, J. Geophys. Res. (USA) 111A5 A05308, doi: 10.1029/2005JA011306.

Mondal, G., M. Gupta, and G. K. Sen, 2017. An Investigation into Height Variation of Ionospheric Signature Due To the Cyclonic Storm Formation Using COSMIC-RO Measurements, Int. J of Engineering Research and Application, ISSN: 2248-9622, 7(7), 76-85, doi: 10.9790/9622-0707077685.

Nina, A., M. Radovanović , B. Milovanović, A. Kovačević, J. Bajčetić, and L. Č. Popović, 2017. Low ionospheric reactions on tropical depressions before hurricanes, Adv. Space Res. 60(8), 1866-1877, https://doi.org/10.1016/j.asr.2017.05.024.

Nolan, D. S. and J. A. Zhang, 2017. Spiral gravity waves radiating from tropical cyclones, Geophysical Res. Letts., 44(8) 3924-3931 https://doi.org/10.1002/2017GL073572.

Park, D. S. R., C. H. Ho and J. H. Kim, 2014. Growing threat of intense tropical cyclones to East Asia over the period 1977–2010. Environ. Res. Letts. (9) 014008, (7pp), doi:10.1088/1748-9326/9/1/014008.

Polyakova, A. S. and N. P. Perevalova, 2011. Investigation into the impact of tropical cyclones on the ionosphere using GPS sounding and NCEP/NCAR Reanalysis data. Adv. Space Res. 48, 1196–1210, http://doi.org/10.1016/j.asr.2011.06.014.

Polyakova, A. S. and N. P. Perevalova, 2013. Comparative analysis of TEC disturbances over tropical cyclone zones in the North–West Pacific Ocean. Adv. Space Res. 52, 1416–1426, http://doi.org/10.1016/j.asr. 2013. 07.029.

Sripathi, S. 2012. COSMIC observations of ionospheric density profiles over Indian region: Ionospheric conditions during extremely low solar activity period. Indian J. Radio & Space Phys. 41, 98-109,http://nopr.niscair.res.in/handle/123456789/14037.

Tian, M., W. JingSong, Y. GuangLin, Y. Tao, P. JinSong and S. YuCheng, 2010. Effects of Typhoon Matsa on ionospheric TEC. Chin. Sci. Bull. 55(8), 712–717, doi: 10.1007/s11434-009-0472-0.

Vincent, R. A. 2007. Gravity wave coupling from below: A review. Climate and Weather of the Sun-Earth System (CAWSES), Kyoto Symposium, 279–293, https://www.terrapub.co.jp/ onlineproceedings/ste/CAWSES2007/pdf/CAWSES_279.pdf.

Vlasov, A., K. Kauristie, M. van de Kamp, J. P. Luntama, and A. Pogoreltsev, 2011. A study of Traveling Ionospheric Disturbances and Atmospheric Gravity Waves using EISCAT Svalbard Radar IPY-data. Ann. Geophys. 29, 2101–2116, doi 10.5194/anger-29-2101-2011.

Yigit, E., and A. S. Medvedev, 2015. Internal wave coupling processes in Earth's atmosphere, Adv. Space Res. 55 (4), 983-1003, https://doi.org/10.1016/j.asr.2014.11.020.

FORM IV
(See rule 8)

1.	Registration No.	:	ISSN-0555-7631
2.	Place of Publication	:	Old Correspondence Building Panjab University, Chandigarh – 160014 (India)
3.	Periodicity of Publication	:	Annual
4.	**Publisher's & Editors' Name**	:	
	Editor-in-Chief	:	Professor G.S.S Saini
	Nationality	:	Indian
	Editor	:	Professor Desh Deepak Singh
	Nationality	:	Indian
	Address	:	Research Journal (Science) Room No. 28-29, Old Correspondence Building, Panjab University, Chandigarh- 160014 (India)
5.	Printer's Name	:	Mr. Jatinder Moudgill
	Nationality	:	Indian
	Address	:	Manager Panjab University Printing Press Chandigarh – 160 014.
6.	Name and address of the Individuals who own the newspaper and partners or shareholders holding more than one percent of the total capital.	:	Panjab University, Chandigarh

Professor G.S.S Saini, hereby declare that the particulars given above are true to the best of my knowledge and belief.

Professor G.S.S Saini
Editor-in-Chief

PANJAB UNIVERSITY RESEARCH JOURNAL (SCIENCE)

LIFE MEMBERSHIP FORM

Name _____

Qualification _____

Area of Specialization _____

Present Designation _____

Address: (Tick the address on which you would like to receive the journal. Local members would receive the journal by hand)

i. Office _____
_____

ii. Residence _____
_____

Telephone (O) _____
(R) _____
(Mobile) _____
Fax _____
Email. _____

Payment Mode:

(Only local cheques are acceptable. Draft to be drawn in favour of **The Registrar, Panjab University, Chandigarh**

If by cheque/Draft:
Cheque/D.DNo. _____ Date _____ Amount_____
Name of the Bank: _____

Date _____
Place: _____

SIGNATURES

Subscription fee:

	Inland	**Foreign**
Life Membership:	Rs. 3000/-	US $ 250
Annual Subscription:	Rs. 400/-	US $ 50

Send to: The Editor-in-Chief
Research Journal (Science)
Room No. 28-29, Old Correspondence Building
Panjab University, Chandigarh-160014(India)

INSTRUCTIONS FOR AUTHORS

Panjab University Research Journal of Science (PURJS) is an international peer-reviewed journal covering wide-range of research activities in all disciples of science.

PURJS provides opportunity to scientists, engineers and medical experts to publish original full research articles, rapid communications, state-of-the-art reviews in all disciplines of the science, engineering and medicine.

JOURNAL POLICY: It is PURJS policy to publish only original and unpublished research work, therefore, PURJS does not wish to receive any papers on research work that has already been reported in parts or contains already published text, data, figures, tables or other illustrations or any copyright materials whatsoever that has been submitted or accepted for publication either in a journal or conference proceedings elsewhere in any form, in print or in electronic media. When submitting a manuscript, authors should make a full statement to the Editors that the research work contained in their manuscript is completely original and unpublished. If redundant or duplicate publication is attempted or occurs authors should expect immediate editorial action to be taken including prompt rejection of the submitted manuscript. Submission of any manuscript that contains redundant or duplicate publication of the same or very similar research work violates the policies of this journal

ETHICAL COMPLIANCE: Research papers reporting animal or clinical studies should, where appropriate, contain a statement that they have been carried out with animal or human ethics committee approval. All scientific studies should be carried out in accordance with the relevant national and local guidelines. Each author(s) warrants that his or her research institution has fully approved the protocol for all scientific studies involving animals or humans and that all experiments of any kinds were conducted in compliance with ethical and humane principles of research after ethics committee approval.

SUBMISSION OF MANUSCRIPT: Authors are requested to read PURJS policy before submitting their manuscript to Editors. Authors are encouraged to submit high quality original research work that has not been published or nor under consideration by other journals or conference proceedings elsewhere. Authors should submit manuscript electronically as a Microsoft Word file to the Editor-in-Chief. Authors are highly encouraged to submit manuscript electronically as a MS Word file (preferred) or a PDF file to save time for the reviewing process.

Authors should submit a list of SIX (6) potential referees accompanied with their complete mailing address, telephone, fax and email address, who may be contacted for reviewing the manuscript though refereeing, is done by anonymous reviewers selected by the Editor-in-Chief or Editor. (The selection of the reviewer is the discretion of Editors –in-chief and reviewers may not necessarily be from the list provided).

MANUSCRIPTS - The manuscripts should be typewritten (double spaced) with ample margins.

Page 1 should contain only title of manuscript, author(s) name(s) and affiliation(s), a short running title (abbreviated from the title) not exceeding 40 characters, name & complete mailing address of the person to whom correspondence should be addressed.

Page 2 should contain an abstract not exceeding 150 words. The abstract should contain no illustration or reference to the figures, tables, or authors. The abstract should be followed by 3-4 key words.

Rest of the content also continue from this page and should be described under Headings, Introduction, Results and Discussions. Acknowledgements should be inserted at the end of the text before References.

SHORT COMMUNICATION: A short communication should be a record of completed short investigation giving details of new methods or findings. It should not exceed 4 to 5 typed pages with an Abstract followed by Key words. Body of the text should not have any separate title, like Abstract, Materials and Methods, Results and Discussion except the Acknowledgements and References.

REFERENCES:

While citing references in the text it should conform to the following style:-

Adherence of *E. coli* to intestinal mucosal surface...pathogenesis (Beachey, 1981). According to Arnoldi (1976), these feathers....

The references at the end of article should be in alphabetical order and presented as follows:-

Ahuja, D.B. 1990. Population dynamics of mustard aphid, Lipaphis erysimi (Kalt.) on Indian mustard Brassica juncea. Indian J. Plant Protection, 18 : 233-235.

Bener, A. and F.C. Erk. 1979. The analysis of whorls on specific fingerstips with respect to sex, bilateral asymmetry and genetic relationship. Ann. Hum. Biol., 6 : 349 - 356.

Buskrik, E.R., K.L. Anderson, and J. Brozek. 1956. Unilateral activity and bone and muscle development in the forearm. Res. Quart., 27 : 127-131.

Jain, S.K. 1986. Orchid Wealth of India. In: Biology, Conservation, and Culture of Orchid
s (Ed.S.P.Vij) pp. 319-22. Affiliated East - West Press (New Delhi).

ILLUSTRATIONS: The illustrations, preferably be in the form of text-figures, should also be submitted electronically. All figures whether photographs or drawing, must be numbered in single series (Fig. 1, 2, 3.etc.). The figures should be arranged and numbered in the order in which they are referred to in the text. The figures or photographs (plates) submitted for publication must not be less than 300 DPI. The ratio of length & width of the full figure plate must necessarily be in proportion to the page size of the journal i.e. 23 cm x 18 cm. Figures must carry magnification bars.

Legends to figures should be typed on a separate sheet of paper to be inserted after References. Abbreviations used for the figures should be given in an alphabetical order after the legends.

TABLES: Tables 1, 2, 3 should be single-spaced on separate page and numbered. Each table must bear a short descriptive heading.

PROOFS: Page proof will be sent to corresponding author.

Manuscripts and Correspondence should be addressed:

Editor-in-Chief
Research Journal of Science
Room No. 28-29
Old Correspondence Building
Panjab University,
Chandigarh. 160 014 (India)
Telephone: 0172-2534376
E.mail : resjoursci@pu.ac.in

Published by :
EDITOR-IN-CHIEF
Research Journal (Science)
Panjab University, Chandigarh-160 014
INDIA

www.puchd.ac.in

ISSN-0555-7631